**Simplicity, flexibility, quality.**
REDOX-FLOW.COM

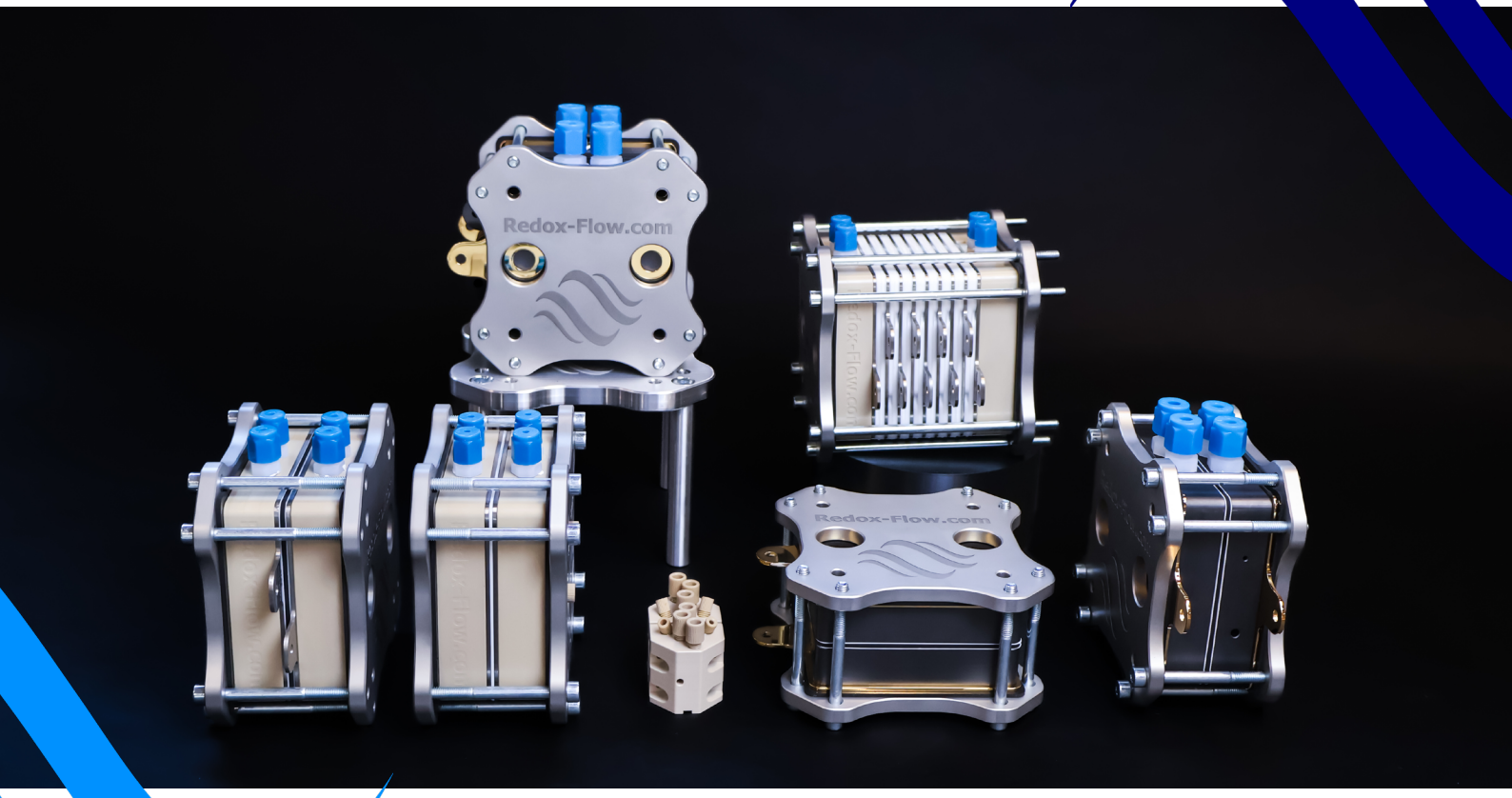
@redoxflow @RedoxFlow redox-flow.com

Redox Flow®

# WHITEPAPERS

**CARRIED OUT BY THE REDOX-FLOW TEAM**

Published in 2025
Last Updated 2026 November




**CONTACT**

Mikkel Kongsfelt
*CEO and Head of Sales*
sales@redox-flow.com
+45-3126-2040

# Contents

Measurement of Overpotentials and Liquid Potentials in Flow Batteries 4

Flow Rates and Pressure Drop in Tubes and Redox Flow Units 16

Heat Transfer Performance of Redox Flow Temperature Control Units with Single-Pass and Continuous Flow Heat Exchange 20

Experimental Investigation of Hydraulic Shunts, Liquid Potentials, and Shunt Currents in Vanadium Flow Battery Stacks 28

X-Stacks With Flow Field and Flat Surface Current Collectors 48

Accurate Overpotential and Reference Electrode Measurements in Water Electrolysis Using the 1 $cm^2$ M-Cell 56

1 $cm^2$ M-Cell: Flow Battery Tests 86



WHITEPAPER I

# Measurement Of Overpotentials And Liquid Potentials In Flow Batteries

## Introduction

Flow battery R&D is much driven by optimization of electrodes and flow cell geometry. In a standard lab type flow battery setup, it is only the electrical current and cell potential that is measured. Although these two parameters alone determine the overall performance, it is from an R&D perspective desired to understand which parts and components that contributes to the overall energy losses. This white paper focuses on the experimental possibilities for mapping these losses out.

Note that this white paper only applies for reversible electrochemical systems, like flow batteries. For irreversible electrochemical systems like water electrolysis other methods are needed.

## Definition of energy levels

Figure 1 below is a general representation of the energy levels in a flow battery (or any other reversible electrochemical flow system). In the figure the blue scale represents absolute energy levels with respect to e.g. SHE. On the absolute scale the abbreviations are:

- $\varepsilon_{CC-}$ and $\varepsilon_{CC+}$ : The potential on the negative and positive side current collectors
- $\varepsilon_{-}$ and $\varepsilon_{+}$ : The (redox) potential of the liquid on the negative and positive side – note that it is variable and depends on the state-of-charge and is described by the Nernst equation
- $\varepsilon_{ref}$ : The potential of (a) reference electrode(s) in the setup

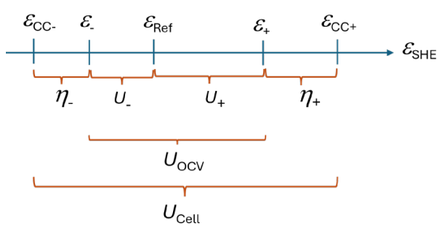



*Figure 1. Energy levels in flow batteries.*





While the upper (blue) potentials are absolute energy levels, the lower (orange) parts show the measurable voltages. Here

- $\eta_{-}$ and $\eta_{+}$: The overpotentials for the charging (discharging) the negative and positive side liquids
- $U_{-}$ and $U_{+}$: Measured potentials with respect to a reference electrode to determine the liquid (redox) potentials of the negative ($\varepsilon_{-}$) and positive side ($\varepsilon_{+}$)
- $U_{OCV}$: Potential measured in an OCV cell
- $U_{cell}$: The potential measured on the electrochemical cell by battery tester or potentiostat

The overpotentials and the electrolyte redox potentials are the most important parameters for mapping out internal resistive losses. There are multiple ways for a total mapping out of $\eta_{-}$,$\eta_{+}$ , $\varepsilon_{-}$ and $\varepsilon_{+}$ and only two are outlined below.

## Setup with reference electrodes and OCV cell

Figure 2 shows a generic representation of how the energy levels are completely mapped out by use of reference electrodes. The red lines depict the hydraulic circuit, while blue lines are potential measurements and the black part are units in the hydraulic circuit. This includes bottles, pumps, reference electrodes, flow through electrode holders, OCV cell and flow battery cell.

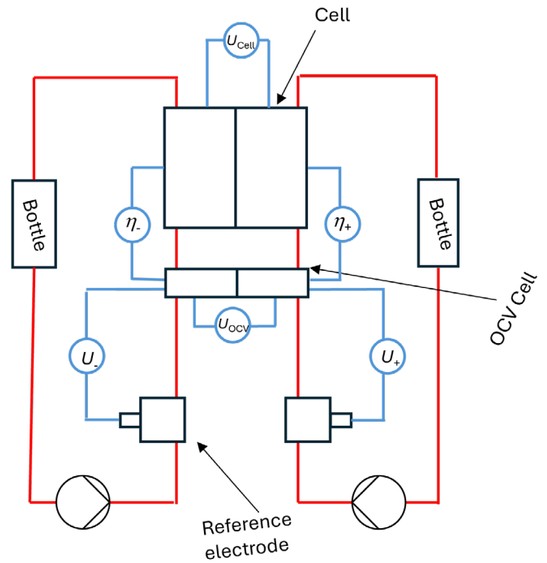



*Figure 2. Schematic representation of a setup with reference electrodes.*

The voltage difference between the negative side of the OCV cell and the current collectors on the flow cell measures the negative side overpotential ($\eta_-$) and vice versa for the positive side overpotential ($\eta_+$). I.e. the difference between the applied potential to the current collector and the potential of the solution. The voltages $U_-$ and $U_+$ measured between the reference electrodes and the OCV cell can be related to the redox potentials of the solutions ($\varepsilon_-$ and $\varepsilon_+$). Depending on the sign definitions and the electrical connections, $U_- = \pm\varepsilon_- \pm \varepsilon_{\mathrm{ref}}$ and $U_+ = \pm\varepsilon_+ \pm \varepsilon_{\mathrm{ref}}$, where $\varepsilon_{\mathrm{ref}}$ is the standard potential of the reference electrode.

An experimental setup based on a 12A/5V tester, a S-cell with 25 cm² active area, with AV Carb (G475) thermally treated carbon felt electrodes and Fumatech FS930 membrane was assembled in a circuit similar to the one in figure 2. Reference electrodes (double junction calomel) were inserted into Redox-Flow.com flow through electrode holders. The OCV cell was mounted with a FS930 membrane.

The reference electrodes were calibrated against a pristine V3/4+ solution and values around 0.19 V were consistently measured over time. In all tests standard 1.6 M vanadium solutions were used for tests and ambient temperatures were in the range 22-24°C.

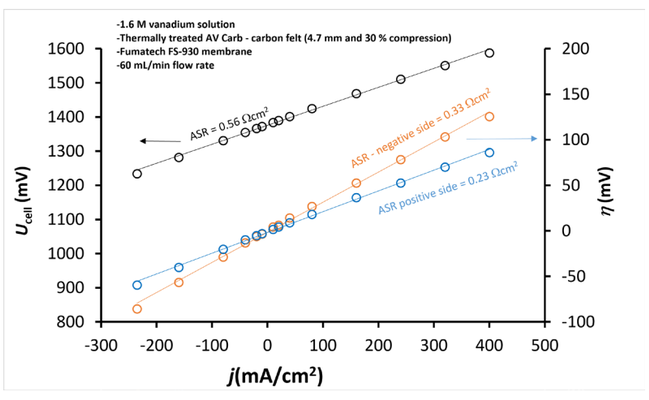



*Figure 3. Polarization curve and overpotentials for both negative and positive side. Note that the reference electrodes are not used in this experiment.*

Figure 3, shows the polarization curve measured at 50% State-of-charge (SOC). Here a very low internal area specific resistance (ASR) of 0.56 Ωcm² was found. From the overpotential measurements the contributions were found to be higher for the negative side (0.33 Ωcm²) compared to the that of positive side (0.23 Ωcm²), and is in agreement with scientific literature. It can also be seen that the two half-cell ASRs add up to the total value. In the figure both overpotentials are defined as positive on charging and negative on discharging, other sign conventions can be used and defined from Figure. 1.





To further demonstrate the capabilities of the setup, Figure 4 shows the first initial (pre) charging to full 100% SOC for a vanadium flow battery with 8 A (320 mA/cm²). The top graph shows the cell potential, OCV and redox potentials of the negative and positive side with respect to $V^{3/4+}$($\varepsilon_- = \pm U_- \pm \varepsilon_{\mathrm{ref}}$, where $\pm$ refers to sign definitions and electric wiring). The capacity of the battery is about 2787 mAh and it is seen that both ε and ε+ remain low but increasing with capacity until approximately 1400 mAh where both increases suddenly due to the initial pre-charging is finished and the electrolyte reaches 0% SOC. After this and $\varepsilon_-$ and $\varepsilon_+$ increases until maximum SOC is reached.

Also $U_{\mathrm{OCV}}$ is measured from the OCV cell and shown in the figure, alternatively it could also be constructed from the measured redox potential ($U_{\mathrm{OCV}} = \varepsilon_+ - \varepsilon_-$). A comparison show that they are within 5-10 mV of each other, this discrepancy is primarily attributed to shunt currents (see below). In the range where the precharging is about to finish the difference is larger. This discrepancy is attributed to the short charging time (25 min), relatively low flow rate and different time constants for the units. i.e. due to the double junction (high resistance) of the calomel electrodes it is expected that they are reacting a little slower than the OCV (low resistance). The consequence is that the system is not in equilibrium. A slower charging and higher flow rate would give more consistent results.

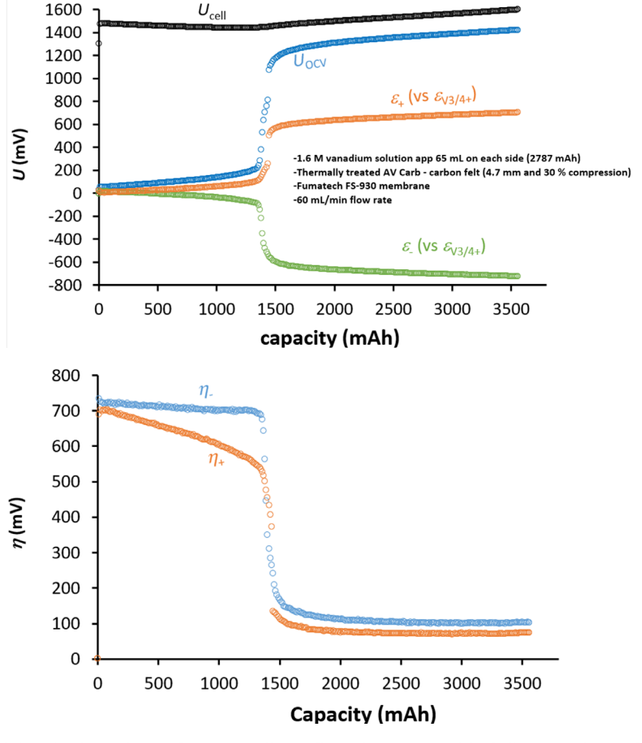



*Figure 4. First initial (pre) charging of a vanadium flow battery with full mapping of all energy levels in one single experiment.*

Lower graphs in figure 4, shows the negative and positive side overpotentials. Here it is seen that there is a significant overpotential associated with the pre-charging of the electrolyte. However, once the electrolyte reaches 0 % SOC and onwards, the overpotentials drops to about 80-120 mV.

## Setup with OCV cell with internal reference

Redox-Flow.com has developed a unique OCV cell that enables addition of a central chamber to the OCV cell. This central chamber can be used as an 'internal' reference electrode in the OCV cell and replace the reference electrodes used in the other setup.

Schematic figure below shows the setup. Again, red and blue lines refer to the electric and hydraulic circuit respectively, while the black parts are units in the circuit.

As in the previous setup, the overpotentials ($\eta_-$ and $\eta_+$) are measured directly between the outer chambers of the OCV cell and electrochemical flow cell. While the redox potentials ($\varepsilon_-$ and $\varepsilon_+$) are measured with respect to the redox solution in the central chamber through the voltages $U_-$ and $U_+$.

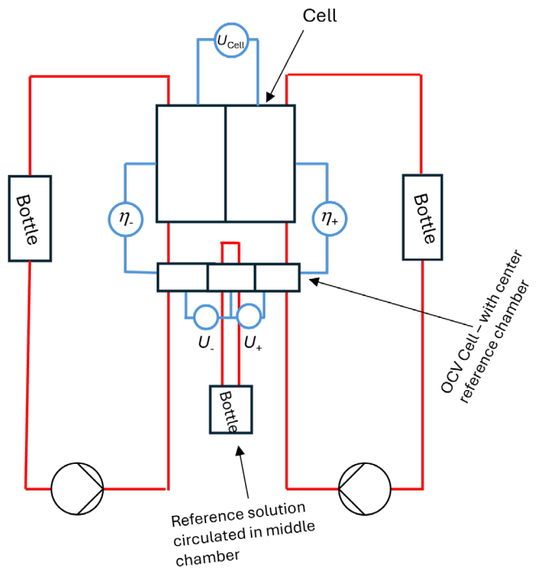



*Figure 5. Schematic representation of a setup with an OCV cell with internal reference.*





The central chamber reference solution is circulated from an external third bottle. If the reference solution is not circulated the reference solution may 'drift' as the membranes are not fully perm-selective, whereby the reference potential changes with time. There can be specific chemistries, membranes or short experimental times where circulation is not necessary, however, Redox-Flow.com recommends as default to use circulation if this option is used.

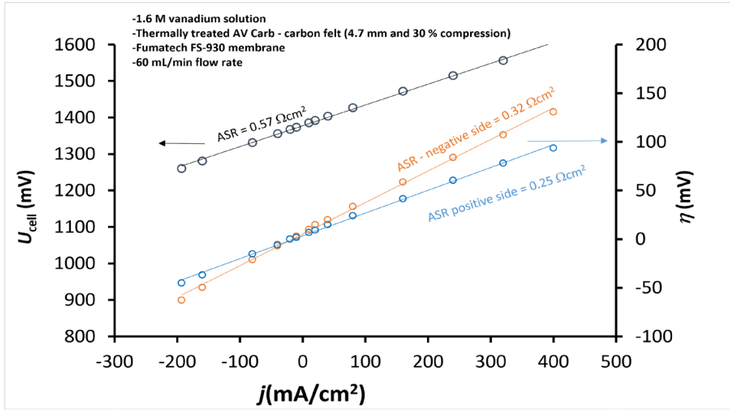



*Figure 6. Polarization curve and overpotentials for both negative and positive side. Note that the reference electrodes are not used in this experiment*

Figure 6 shows the polarization curve at 50 % SOC and an ASR of 0.57 Ωcm² is found and within experimental uncertainty of the 0.56 Ωcm² found in the normal OCV setup. Also the ASRs for the negative (0.32 Ωcm²) and positive (0.25 Ωcm²) are very close to the ones found in the previous test. This not only underlines the robustness of the method, but also that both setups are suitable for measurement of overpotentials.

To demonstrate the capabilities of the setup, Figure 7 (similar to Figure4) shows the first initial (pre) charging to full 100% SOC for a vanadium flow battery with 3 A (120 mA/cm²). The central reference chamber of the OCV cell is circulated with pristine $V^{\frac{3}{4}+}$ vanadium solution at a rate of 60 mL/min (same solution as used in the flow battery cell). The top graph shows the cell potential, OCV and redox potentials of the negative and positive side. Since the reference solution is $V^{\frac{3}{4}+}$ no conversion/calibration of the voltage measurement is needed. Overall, the trend is the same as for the setup with reference electrodes and demonstrates the functionality of the OCV cell with reference chamber.

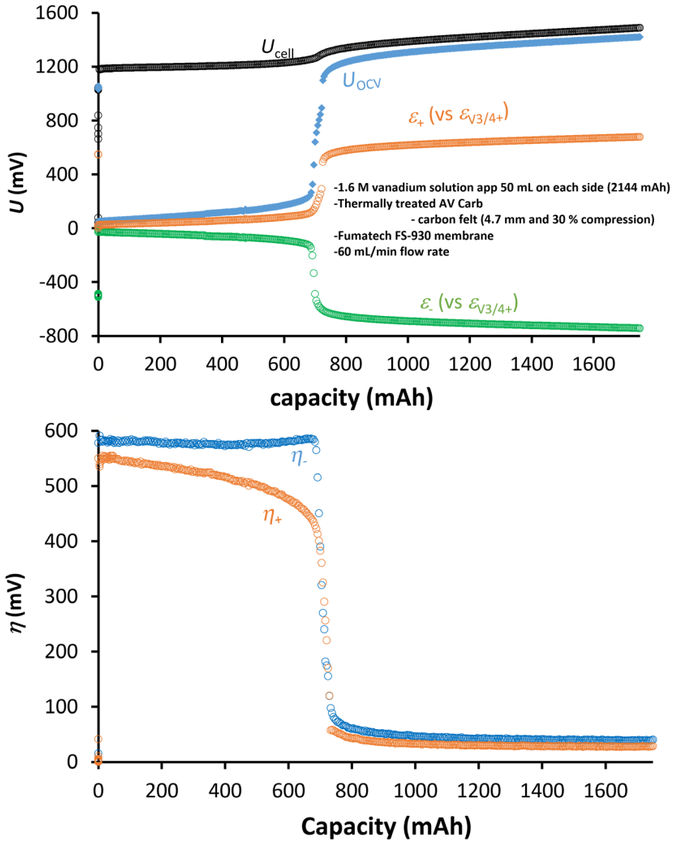



*Figure 7. First initial (pre) charging of vanadium flow battery with full mapping of all energy levels in one single experiment.*

## Cycling data and hydraulic shunt

To further demonstrate some of the potential R&D applications, a battery cycling test was conducted on the setup with the OCV cell with internal reference. Here the cycling parameters were 3A constant current charging/discharging to 1.6 V and 0.8 V, followed by constant voltage charging/discharging down to 0.3 A.

Figure 8 shows the charge/discharge capacity vs the cycle number. As can be seen the capacity retention drops quite fast as the battery is cycled. This mechanism behind the capacity is quite complex but mainly determined by cross-over of vanadium from one to the other side, whereby the other side becomes the capacity limiting factor. To balance out this cross-over and volume changes in the two bottles, the bottles are in many cases connected with a tube/hydraulic shunt. This is switched on after cycle 21. Here it is seen that the capacity is somewhat restored in the subsequent cycles (some of the electrolyte also becomes inactive in the syringe used in the shunt, explaining partly the missing capacity).





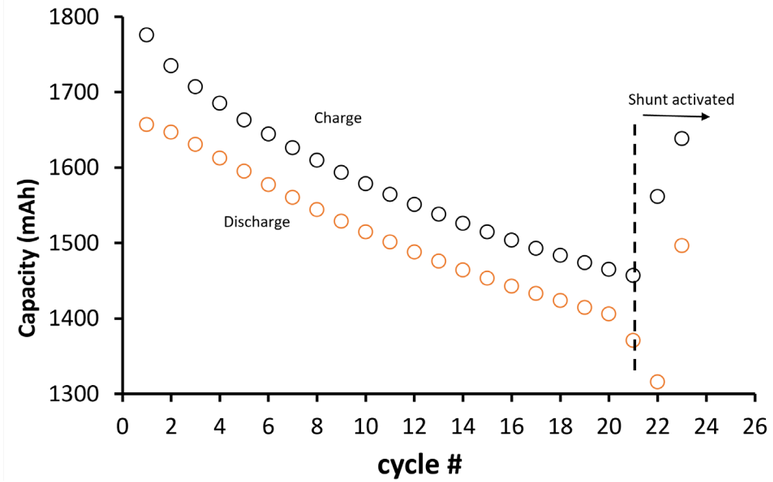



*Figure 8. Charge/discharge capacity vs cycle number. First cycle that includes pre charging is not included. After cycle 21 shunt between the two bottles is activated.*

The understanding of the capacity fade can be improved by measuring the liquid redox potentials of the solutions with OCV cell with internal reference as shown in figure 9. From the liquid potentials on the negative side it is seen that they have a sharper decrease on discharge as it approaches 0% SOC (and sharper increase on charging) compared to that on the positive side. This is a clear indication that the negative side, is the capacity limiting side and that vanadium ions are transferred to the positive side during repeated cycling. Once the hydraulic shunt is opened, these cross-over effects are mitigated and capacity is (somewhat) restored.

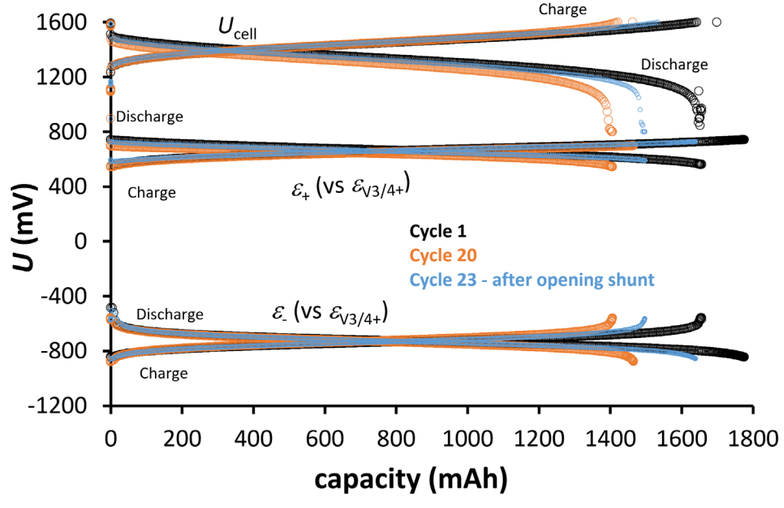



*Figure 9. $U_{cell}$, $\varepsilon_-$ and $\varepsilon_+$ for cycle 1, 20 and 23 on charge and discharge.*

## Shunt Currents

It has been reported that shunt currents through the OCV cell can affect the overpotential measurements. To investigate the magnitude of this effect, an experiment where both the 'OCV cell with internal reference' and reference electrodes were inserted into the same experimental setup. It was charged to a specific value and left resting until all potential measurements were stable. Then 8 A (pulse) charging was applied, and all potentials were monitored as function of time. Results are shown in figure 10. The top graph shows the overpotential measurements and as expected a sharp increase is seen when the current is applied, and the voltage change is considered as being the overpotential.

It is expected that $\varepsilon_- + \varepsilon_+$ should remain constant (no change of SOC within seconds of the charging). If this is not the case, it can be seen from $U_{cell} = \varepsilon_- + \varepsilon_+ + \eta_- + \eta_+$ (figure 1) that this would lead to an error in the overpotential ($\eta_- + \eta_+$) measurement. As can be seen from the middle graph in figure 10, the potential change of $\varepsilon_-$ and $\varepsilon_+$ is about 1-1.5 mV and the error on the overpotential 80-120 mV (top graph) is only of the order 1% and not as high as reported elsewhere in literature. It is anticipated that the low impact is due to the low internal resistance of the Redox-Flow.com OCV cell. The tube length (1/16'' ID) from cell to OCV cell is total about 20 cm and results in approximately 0.06 mA shunt current through the OCV cell. It is anticipated that the OCV cell with internal reference chamber has a very low internal resistance of about 10 Ω, which would result in a potential loss of about 0.5 mV and in relative agreement with the value of about 1 mV.

As a last point, the lower graph shows the response of the calomel electrodes. Here a larger potential change of about 5 mV is seen. This potential change does not as such affect the overpotential measurement but will lead to error in the liquid potentials. This error should not be compared directly to the overpotentials measurement, but to the relative change over a full SOC, which is of the order 200 mV. In this case it is still relatively small, but there can be specific experiments where this error is unacceptable and here it is recommended to use a blocking sheet (PTFE) inside the OCV cell that is supplied with the OCV cell. The blocking sheet isolates the two sides of the OCV cell and prevents shunt current, hereby it no longer works as an OCV cell, but can only be used for overpotential measurements.





## Internal resistance of electrochemical devices and measurement of voltage signals

The voltage from the OCV cell and reference electrodes in the experiments above have been measured with the AUX unit that can be supplied together with the battery testers sold by Redox-Flow.com. When measuring on electrochemical devices/sensors it is important to understand the magnitude of the internal resistance of the device. I.e. the internal resistance of the OCV cell is in the range 5-50Ω depending on configuration, membrane and chemistry. The double junction calomel electrode has an internal resistance of about 3-8 kΩ. Internal resistances below 10-30 kΩ are 'considered' as low and can be measured by standard voltmeters (that typically have internal resistances > 100 kΩ).

Nonetheless, it is paramount that the voltage measurement device is bipolar. I.e. the voltage measurement device cannot share a common 0/zero for measuring multiple potentials.

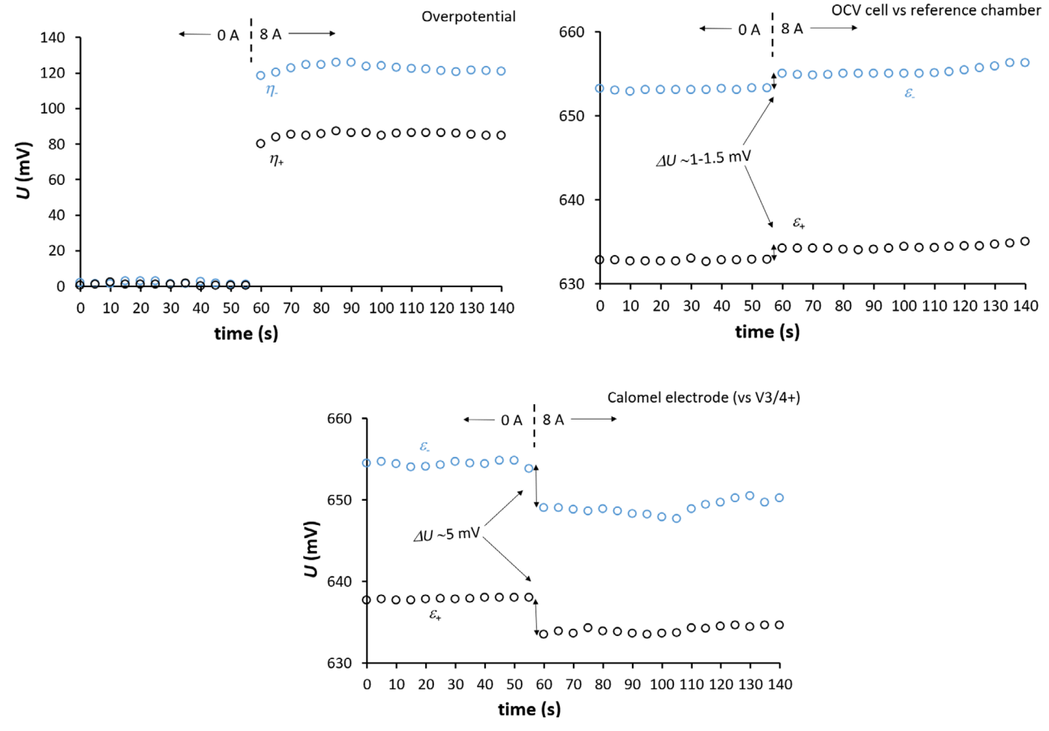



*Figure 10. Direct current pulse experiment to monitor effect on voltages.*

Besides this, in some cases it can be considered to include galvanic isolation between the electrochemical device and voltage measurement unit. If there is a voltage bias between the experimental setup and the measurement unit, this can lead to galvanic/electrical currents between the electrochemical sensor and measurement unit, this will quickly deteriorate the electrochemical sensors and give false readings. Alternatively, this can also be mitigated by grounding all devices in the setup that is connected to grid power to the same ground, connecting all devices to the same ground connection can minimize/remove voltage biases. Also, for many other good reasons grid powered devices in the same experimental setup should always be connected to the same ground.

## Considerations and recommendations

Choosing the right experimental setup for mapping out energy levels and potentials can be done in many ways. However, in many applications it is not necessary to make a full mapping and is there redundancy in the measurements. Table below summarizes some of the considerations for the experimental setup.

| What kind of measurement is needed? | OCV only? Overpotentials? Electrolyte redox potential – for one side only or both sides? |
|---|---|
| **Shunt currents through OCV cell** | It is easy to measure through a direct current pulse measurement. How accurate does the measurement need to be? Consider tube lengths and placement of units. If there is a hydraulic shunt between electrolyte bottles (only for vanadium flow battery systems), what impact can that have on shunt currents. |
| **Time delays in the electrochemical and hydraulic system** | As the units (reference electrode, OCV, flow battery cell) comes in series there can be some delay in the response depending on dead volumes, flow rates and electrical current. I.e. higher flow rates and lower electrical currents will mitigate this. |
| **Measure before / after electrochemical cell** | Whether to measure before or after the flow battery cell, depends on the specific aim of the test. For standard tests like the ones in this note, we recommend measuring before. |
| **Electrical measurements** | Both the OCV cell and the double junction reference electrodes of redox-flow.com are ‘low impedance’ and the voltage can be measured directly on standard voltmeters and data loggers. However, the voltage must be measured in a bipolar manner (i.e. no common 0 between several independent voltage measurements). |
| **Reference electrodes** | In most redox-flow batteries the electrolyte concentrations are so high that a large osmotic pressure difference is built up between electrolyte in flow battery and reference electrode. This will result in pollution/deterioration of the reference electrodes. So always use double junction reference electrodes. |

Finally, the table below shows some of the advantages/disadvantages between using a setup with an OCV cell with internal reference or reference electrodes. Redox-Flow.com does not promote one over the other, we have developed the OCV cell with internal reference because we are ‘electrochemical nerds’, so consider the internal reference as a research tool.

| | Advantages | Disadvantages |
|---|---|---|
| **Reference electrodes with standard OCV cell** | • Well described in literature<br>• Shunt currents can be blocked in OCV cell | • Calibration of reference electrodes<br>• Drifting of reference electrodes over prolonged testing time |
| **OCV cell with internal reference** | • Only need one unit for a full mapping<br>• Hydraulic circuit becomes very simple – few connections and fittings<br>• The internal reference option/middle chamber is included as an option with the Redox-Flow.com OCV cell<br>• Potentially no calibration of ‘reference solution’ – depending on chemistry | • The reference electrolyte must be circulated in the central chamber (can relatively easy be done with peristaltic pumps, if an additional pump head can be added to the pump)<br>• There are limited number of reference electrolyte solutions available. For vanadium flow batteries V3/4+ solutions can be used. For neutral/alkaline Ferro/Ferri-cyanide solutions can be used, but may not be compatible with the flow battery chemistry)<br>• Shunt currents – If the OCV cell with internal reference is used for mapping out all potentials, there will be shunt currents through the OCV cell. This can destroy accuracy of the measurements. |

## References and suggested reading

In connection with this note, it is suggested to read the following papers to get an overall understanding of the methodology and theory.

1. Gonzalez, G., & Peljo, P. (2025). Experimental Set-Up for Measurement of Half-Cell-and Over-Potentials of Flow Batteries During Operation. Batteries & Supercaps, 8(2), e202400394.

2. Langner, J., Melke, J., Ehrenberg, H., & Roth, C. (2014). Determination of overpotentials in all vanadium redox flow batteries. ECS Transactions, 58(37), 1.

WHITEPAPER II

# Flow Rates And Pressure Drop In Tubes And Redox Flow Units

## Introduction

Understanding and managing pressure losses in tubing and electrochemical units is essential for ensuring optimal performance and reproducibility in electrochemical flow systems. We are often asked about best practices and design considerations regarding pressure drop. While the final configuration must be tailored to your specific application, this white paper provides guidance and insight to support more informed decision-making.

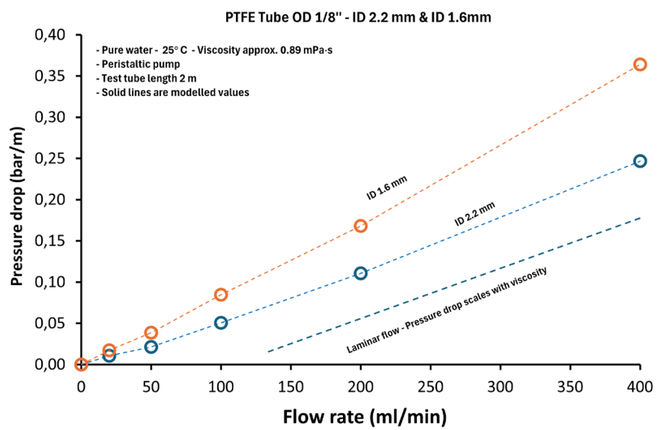
## Tubes

At Redox-Flow.com, we offer three standard tubing sizes, listed with their outer (OD) and inner diameters (ID):

- 1/8'' OD – 1/16'' (1.6 mm) ID
- 1/8'' OD – 2.2 mm ID
- 1/4'' OD – 4.35 mm ID

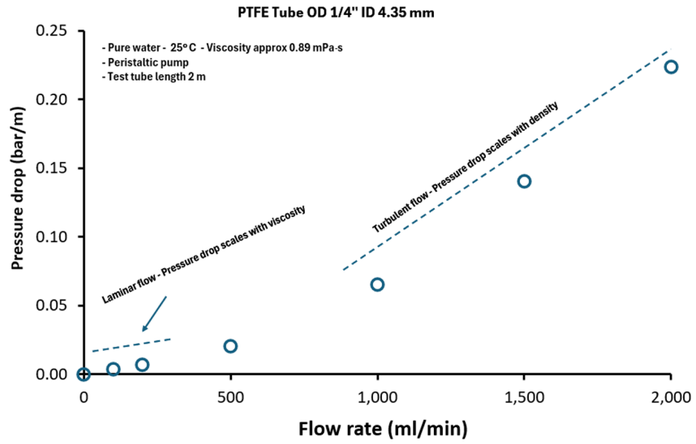
The pressure drop per meter of tubing is shown in the graphs below as a function of flow rate. These measurements were taken using pure water at room temperature. However, it is important to note that pressure loss is influenced by:

- Fluid viscosity (large dependence on temperature),
- Fluid density (small dependence on temperature, but large dependence on dissolved salt/chemicals)
- Flow regime (laminar vs. turbulent)








## Flow Regimes and Pressure Drop

The pressure loss depends on the viscosity (temperature) and density of the fluid and whether it is in laminar or turbulent flow range. For laminar flow range, the pressure drop is proportional to the viscosity, turbulent flow range the pressure drop is proportional to the density of the fluid.

To estimate pressure drop for a given setup, determine whether the flow is laminar or turbulent using the Reynolds number (Re):

$$Re = \frac{\rho Q D}{\mu A}$$

Where $\rho$ is the density of the liquid, $Q$ is the flow rate and $D$ is the diameter of the tube, $\mu$ is the dynamic viscosity of the liquid and $A$ is the cross-sectional area of the tube.

Guideline values:

- Re < 2300 $\longrightarrow$ laminar flow
- Re > 2900 $\longrightarrow$ turbulent flow

Then scale with either density or viscosity of the liquid according to the graphs.

Depending on the tubing length and application, Redox-Flow.com recommends keeping pressure losses below 0.1–0.2 bar/m.

## Electrochemical cells

Redox-Flow.com electrochemical cell types (A, S, and X) are designed to minimize pressure drop at the hydraulic inlet and outlet. However, the total pressure drop depends entirely/ significantly on the electrodes used. Here Redox-Flow.com general recommendations are:

- For thin electrodes (<1 mm thickness): Use current collectors with interdigitated flow fields to improve distribution and reduce pressure drop.
- For thicker electrodes (>1 mm thickness): Current collectors with flat flow fields can be used, although performance heavily depends on the intrinsic hydraulic resistance of the electrode material.

Redox-Flow.com also provides tools and units that allow direct measurement of the hydraulic resistance of different electrodes to support empirical testing and optimization.

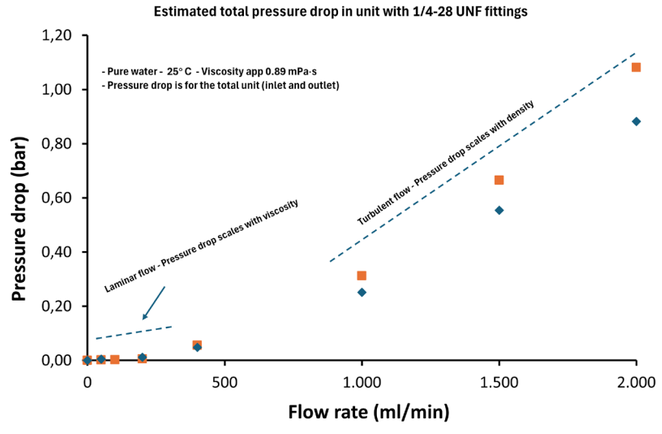
## Inline/electrochemical units

This section applies to inline units using ¼-28 UNF fittings (commonly known as IDEX fittings for 1/8'' OD tubing).

We offer a variety of inline units for integration of:

- Reference electrodes
- Pressure sensors
- UV/VIS detectors
- And more

In these units, pressure drop is largely governed by the fitting and related orifice restrictions. The accompanying graph illustrates pressure losses for two representative units. As observed, pressure loss increases substantially beyond 400 mL/min. For applications requiring flow rates > 500 mL/min, we recommend reaching out to Redox-Flow.com to discuss customized solutions.



WHITEPAPER III

# Heat Transfer Performance Of Redox Flow Temperature Control Units With Single-Pass And Continuous Flow Heat Exchange

## Introduction

Understanding and quantifying heat transfer in compact flow systems is essential for optimizing performance and reproducibility in thermal management and process design. This study focuses on evaluating the efficiency of two types of Redox Flow temperature control units under varying flow conditions: 1) a single-pass plate heat exchange operated using the single flow control unit, and 2) a continuous flow heat exchange operated using the double flow control unit. While the ideal configuration and performance depend on the specific application, the following work provides practical data, analysis, and guidance to support more informed design and operation of small-scale liquid heating systems.

## The temperature control units

The Redox Flow heating & cooling units can be used for controlling the temperature of liquids and electrochemical cells - including flow batteries and electrolyzers. To the best of our knowledge, similar products cannot be found by any other companies in the field.

Controlling temperature of cells and liquids for flow batteries, electrolyzers and other electrochemical flow cells is challenging. One of the most widely used solutions is to place the cell and liquid bottles inside a heating chamber. While Redox-Flow has recommended this solution before (and still does, when it is viable), it comes with several limitations and shortcomings:

- Most commercial heating chambers do not come with feed-through holes for electrical wires to the cell and must be drilled manually
- For high temperature operation, the pump must be placed outside the heating chamber and can result in long hydraulic connections
- In heating/cooling chambers the space is limited and setting up experiments becomes tedious and time consuming
- Chambers with both heating and cooling are in general very costly
- Due to limited thermal conductance through bottles and cells, the time for reaching the set point temperature can be long (> 1-2 hours)





The solution developed by Redox-Flow.com comes in three different configurations that are based on the same components and can be interchanged depending on the purchased option (upgrading is always possible). All options include a PEEK flow body and metal block, shown in the pictures below. The PEEK body contains one (variant 1) or two separate (variant 2) flow chambers for heating/cooling one or two independent liquids, respectively. The liquids in the experimental setup are circulated through the PEEK flow body and placed against a metal heating/cooling plate, whereby heat is transferred to or from the liquids in the PEEK flow body. The metal plate is separated from the liquids in the experimental setup by a thin PTFE sheet, whereby corrosive/oxidative solutions can also be heated without corroding the metal plate. At the time of the studies, the material of the heating block was aluminum.

The aluminum block can be 1) heated by placing it on a heating plate, or 2) heated or cooled using heat cartridges for liquids and thermometers.

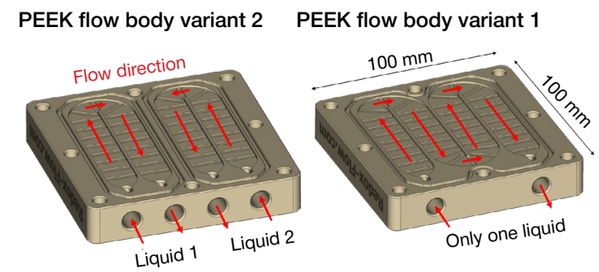



*Figure 1*

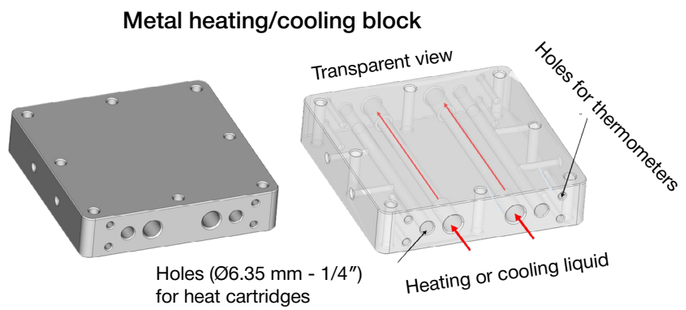



*Figure 2*

There are three options for the heating/cooling unit. For all products, the temperature can be controlled by circulating heating/cooling liquids through the metal block or by using a heat cartridge in the metal block. In two of the products, the temperature can also be controlled by placing the unit on a heating plate.

# Study 1: Single-Pass Heat Exchange Using The Single-Flow Temperature Control Unit

## Experimental setup

The experiment was performed using a peristaltic pump, a Redox Flow single-flow temperature control unit with an aluminum plate, a temperature-controlled heater, and two digital thermometers. Water was used as the working fluid and passed once through the control unit (non-recirculating flow).

The heater temperature was set to 80 °C, 100 °C, and 120 °C, while the flow rate was varied at 4, 8, 12, and 20 mL/min. The inlet fluid temperature ($T_F$) was maintained at approximately 20 °C throughout the experiments.

The following temperatures were recorded:

- $T_F$ : temperature control unit liquid inlet temperature
- $T_E$ : temperature control unit liquid outlet temperature
- $T_A$ : temperature of the aluminum plate

These measurements were also used to calculate the overall heat-transfer coefficients (U) and to evaluate the efficiency of the single-flow temperature control unit under different operating conditions.

## Results

Three graphs were prepared to illustrate the relationship between the outlet temperature ($T_E$) and the flow rate for each heater setting. Each graph corresponds to one of the tested heater temperatures of 80 °C, 100 °C, and 120 °C, and shows how the outlet temperature decreases as the flow rate increases. This trend reflects the reduced residence time of the water in contact with the heated surface at higher flow rates.

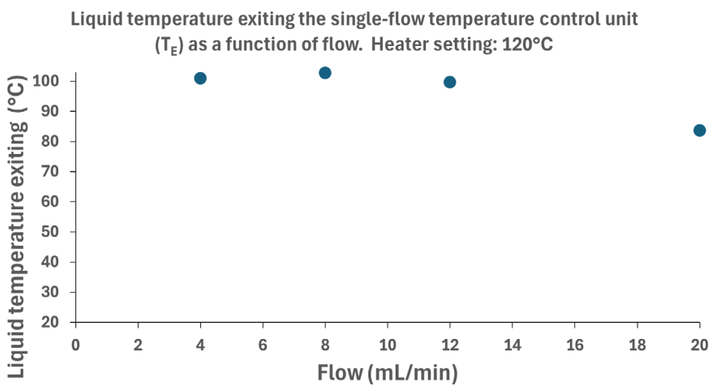



*Figure 3*





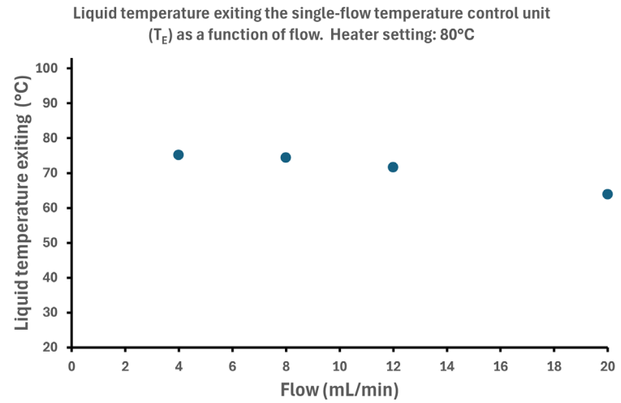



*Figure 4*

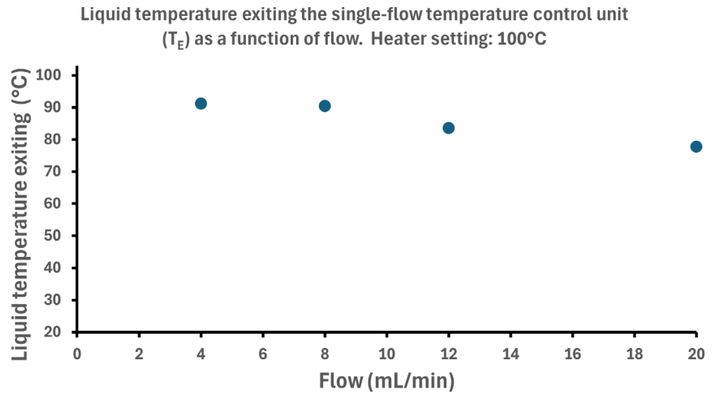



*Figure 5*

The graph below shows the heat transfer coefficient between the aluminum block and the liquid at three different heater settings. The coefficients can be used for estimating the heat transfer power between the unit and the liquid.

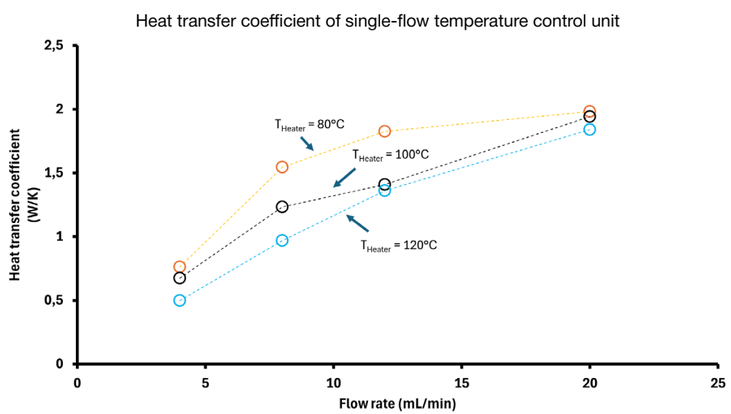



*Figure 6*

## Calculating exiting liquid temperature from the results

The exiting liquid temperature ( $T_E$ ) can be estimated using the empirical formulas below. These equations relate ($T_E$) to the flow rate at different heater setpoints (80 °C, 100 °C, and 120 °C). These models are valid for flow rates between 4 and 20 mL/min. Extrapolation beyond this range may result in unreliable predictions.

**Formula 1**

At the heater setting of 80°C:

$$T_E = -0.0348\big(\text{Flow rate}\big)^2 + 0.1201\big(\text{Flow rate}\big) + 75.383$$

**Formula 2**

At the heater setting of 100°C:

$$T_E = -0.0038\big(\text{Flow rate}\big)^2 - 0.8115\big(\text{Flow rate}\big) + 95.225$$

**Formula 3**

At the heater setting of 120°C:

$$T_E = -0.1166\big(\text{Flow rate}\big)^2 + 1.7069\big(\text{Flow rate}\big) + 96.166$$

## Example Calculation

To determine the flow rate required to achieve an exiting liquid temperature of 80 °C at a heater setting of 100 °C, use Formula 2:

$$80 = -0.0038\big(\text{Flow rate}\big)^2 - 0.8115\big(\text{Flow rate}\big) + 95.225$$

Thus, at a heater setting of 100 °C, a flow rate of approximately 17,35 mL/min results in an exiting liquid temperature of 80 °C.

## Study 2: Continuous Flow Heat Exchange Using The Double Flow Temperature Control Unit

### Experimental setup

The experiment was performed using a peristaltic pump, a double-flow temperature control unit with an aluminum plate, a temperature-controlled heater, and two digital thermometers. Water was used as the working fluid and passed continuously through the temperature control unit (recirculating flow).





## Results

### Heat Transfer Coefficient

Graph below shows the heat transfer coefficient between the aluminum block and the liquid. It is measured by heating about 500 mL of water in a bottle (without an electro-chemical cell) by placing the heating unit on a heating plate where the aluminum block temperature is fixed and the temperature in the bottle is monitored.

The heat transfer coefficient is in the range 1 W/K to 5 W/K and dependent on the flow rate. We term the coefficient ‘apparent’ as it does not strictly follow the definition of the ‘overall heat transfer coefficients’. Nonetheless, the coefficients can be used for estimating the heat transfer power between the unit and the liquid. I.e., if there is a 40 K temperature difference between the aluminum block and the liquid and the flow rate is 100 mL/min, it can be expected that 100 W of heat is transferred.

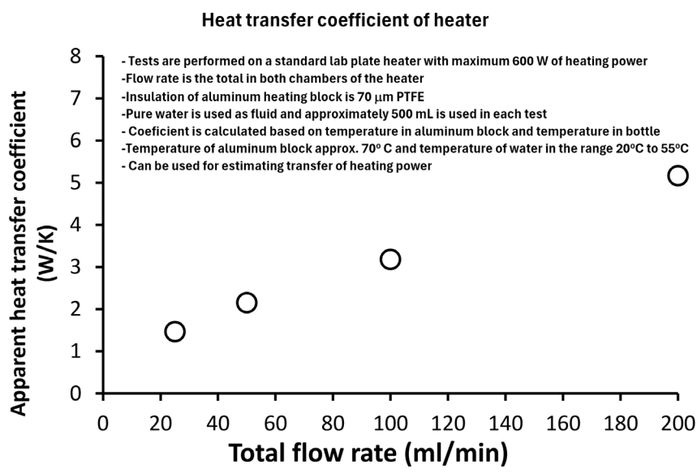



*Figure 7*

### Bottle Heating

Graph below shows a configuration where the unit is placed on a heating plate and connected to a pump and a bottle with 500 mL of water (i.e., an electrochemical cell is not included in the circuit). The heating plate has a maximum of 600 W heating power and PID control, where the input for the control is an external thermometer, which in this case is placed in a bottle. In addition to this thermometer, one is also placed inside the aluminum block. In this test, the water temperature set-point in the bottle was set at 75°C. It is seen that the water reaches 75°C within 15 minutes and stability is reached within about 35 minutes. Better control strategies can shorten time before stability.

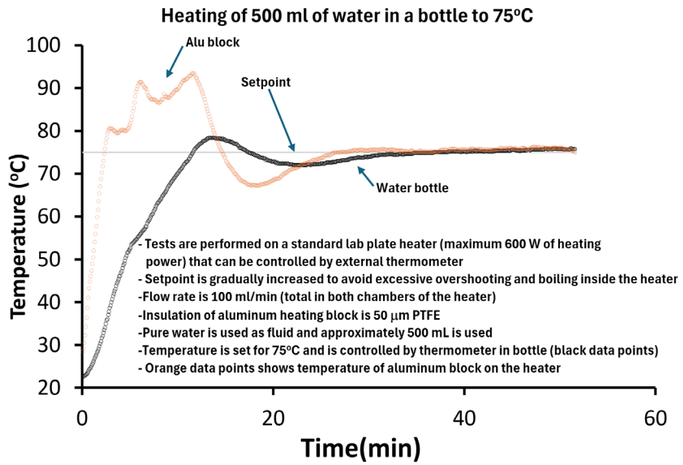



*Figure 8*

## Cell & Bottle Heating

Graph below shows a configuration where the unit is placed on a heating plate and connected to a pump. The heating unit is placed after the pump and followed by an electrochemical cell and a bottle. The total water volume is 500 mL. The heating plate has a maximum of 600 W heating power and PID control, where the input for the control is an external thermometer. In this case, the control thermometer is placed inside the cell (close to the current collector). Temperature stability is reached within about 35-45 minutes. More aggressive temperature control strategies where temperature over shooting is allowed will decrease time to reach the temperature set-point.

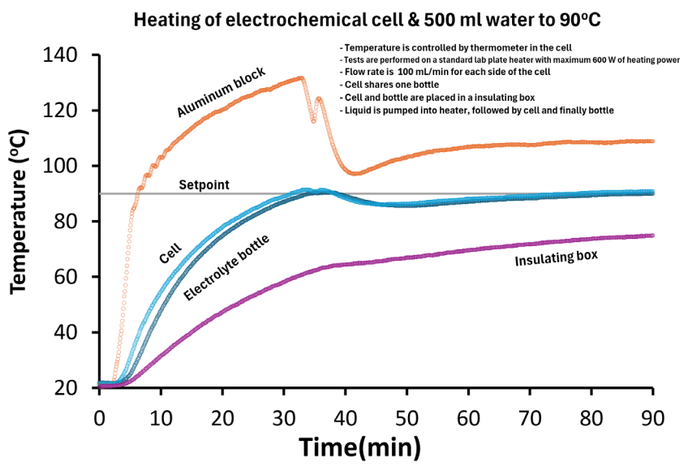



*Figure 9*

WHITEPAPER IV

# Experimental Investigation of Hydraulic Shunts, Liquid Potentials, and Shunt Currents in Vanadium Flow Battery Stacks

## Introduction

This white paper presents an integrated experimental demonstration of stack-scale diagnostics and shunt-current phenomena in a vanadium redox flow battery using modular components from www.redox-flow.com and includes the following sections:

- Stack Cycling & effect of hydraulic shunt on capacity fades
- OCV cell data – Liquid half-cell potentials
- Stack polarization curve & individual cell voltages
- Shunt currents in flow battery stacks
- Effect of shunt currents through OCV cell

The study combines long-term cycling experiments, liquid potential measurements, hydraulic shunt investigations, and shunt-current modeling in a unified experimental platform built entirely from standardized laboratory hardware. A 6-cell Redox-Flow.com S-stack (25 $cm^2$ active area per cell) is operated under realistic flow-battery conditions using commercial vanadium electrolyte, enabling detailed investigation of capacity fade, faradaic efficiency, temperature behavior, and individual cell voltage uniformity.

A central feature is the use of Redox-Flow.com Multiport Electrolyte Reservoirs, which provide nine independent hydraulic ports per reservoir. This unique design enables experimental configurations that are not possible with conventional GL45 bottles, including (i) precise investigation of volumetric crossover effects (ii) direct integration of external OCV cells and similar (iii) controlled hydraulic shunts between reservoirs for gravimetric volume balancing. Using these reservoirs, the white paper experimentally demonstrates how hydraulic shunts can partially restore lost stack capacity by re-balancing electrolyte volumes, while simultaneously quantifying the associated self-discharge mechanisms.

The setup further integrates the Redox-Flow.com OCV cell with internal reference, enabling continuous measurement of liquid half-cell potentials during stack operation. This allows direct observation of electrolyte imbalance, capacity-limiting sides, vanadium crossover, and state-of-charge evolution. In addition, individual cell voltages within the S-stack are monitored in parallel with stack polarization measurements, demonstrating highly uniform electrochemical performance across all cells and validating the hydraulic and electrical stack design.

Finally, the experimental results are linked to a resistor-network shunt current model developed specifically for Redox-Flow.com stack geometries. By combining experimentally measured gasket dimensions with modeling, the white paper quantifies the trade-off between shunt current losses and hydraulic pressure drop, providing practical design guidance for stack optimization.

Overall, the white paper demonstrates how the combined use of the S-stack, multiport reservoirs and, OCV cell with internal reference from Redox-Flow.com enables advanced flow-battery experimentation that bridges the gap between single-cell studies and full system operation.

## Experimental Setup

Figure 1 shows a schematic picture of the experimental setup that includes the following components:

- Stack: Redox-flow.com S-stack with 6 cells
  - 25 cm2 active area per cell
  - Thermally activated AVCarb G475 carbon felt electrode that are compressed from 4.7 mm down to 3.5 mm with flow field gasket of 1.5 mm and two cover gaskets of 1 mm
  - Fumatech FS930 cation exchange membranes
- 10 A/10V battery tester with 8 AUX voltage and temperature logging for reference electrodes and individual cell voltage measurements
- Redox-Flow.com Multiport Reservoirs (2 x 250 mL) for electrolyte containers
- Standard 1.6 M vanadium electrolyte – 210 mL used for both anode and cathode side – total 9005 mAh capacity = 1501 mAh 6 cell stack capacity
- Redox-flow.com OCV cell with internal reference
- Redox-flow.com peristaltic pump with three pump heads
  - Two heads are fitted with #25 peristaltic tube and a flow of 240 mL/min (40 mL/min per cell) – used for the main hydraulic circuit of the stack
  - One head is fitted with a #14 peristaltic tube and a flow of 25 mL/min – used for the hydraulic circuit of the reference for the OCV cell

The main hydraulic circuit between pumps, reservoirs and stack is made with ¼'' OD (4.8mm ID) PTFE tubes. A number of redox-flow.com components are essential in the circuit, nonetheless, the multiport reservoirs are highlighted as they are paramount for the present demonstration. A schematic overview of these is shown in Figure 2, besides having possibility for heating the electrolyte efficiently, the reservoirs comes with 9 ports (6 in the reservoir and 3 in lid) for each reservoir. This allows many additional features that cannot be obtained with normal (GL45) bottles where the maximum number of tube connections is 4. This includes both a (i) hydraulic shunt between the reservoirs, that can level out liquid height differences between the two reservoirs and (ii) use of the OCV cell with hydraulic outlet directly into the reservoir.

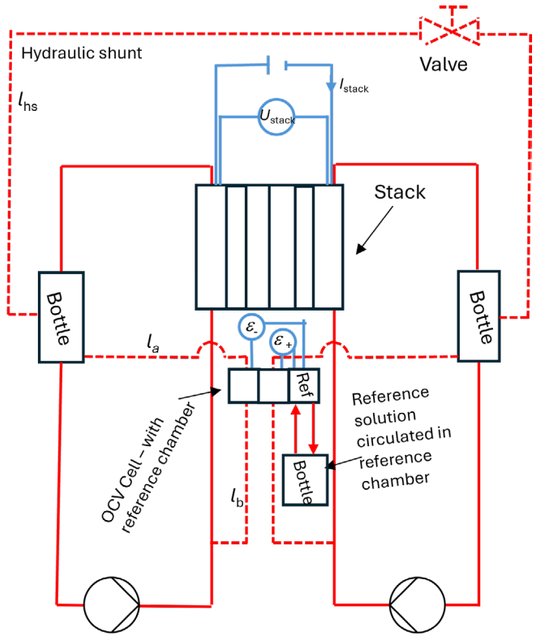



*Figure 1. Schematic representation of the S-stack, OCV cell with internal reference, multiport reservoirs and hydraulic shunt connection between the reservoirs.*

The OCV cell is connected with a T before the stack through 1/8'' OD (1.6 mm ID) PTFE tube while after the OCV cell it is connected directly to the reservoir marked by dotted red line. The length of the 1/8'' OD tube before the OCV is denoted $l_b$ and after it is denoted $l_a$. Rather than connecting the OCV directly in the main hydraulic circuit (as in white paper *Measurement of Overpotentials and Liquid Potentials in Flow Batteries* https://redox-flow.com/whitepapers/), this approach has been selected because (i) The OCV cell has a relatively high hydraulic resistance and flow rates of > 200 mL/min can lead to relatively high pressure losses in the OCV cell (ii) Because of a much higher stack voltage compared to





single cells, shunt currents through the OCV cell will significantly affect the voltage readings from the OCV cell. For that reason the length of the OCV hydraulic circuit is $l_b$ ~100 cm and $l_a$ ~10 cm. It is noted that out of the total flow of 240 mL/min from the pump the flow through the OCV cell was measured to approximately 15 mL/min, whereby the true flow rate inside the stack is only 225 mL/min. The ratio between the two flow rates is not constant and will depend on $l_a + l_b$ and hydraulic resistance of the stack. But it can be measured by disconnecting the $l_a$ tube from the reservoir and measure the transferred volume into a separate bottle over e.g. 1 minute.

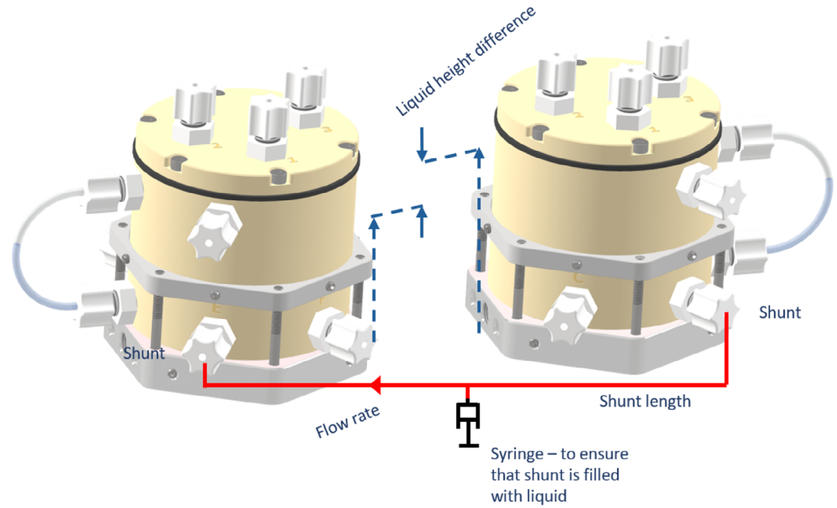



*Figure 2. Overview of Multiport Reservoirs with integrate heating possibilities. In present test, the main hydraulic connections are ¼ '' OD PTFE tubes. Electrolyte is only in contact with corrosion resistant polymers (PP, PTFE, VITON/EPDM). Liquid height inside reservoirs can be measured through the liquid heights in the tubes on the sides of the beakers. Additionally, the reservoirs are hydraulically connected through a shunt (40 cm 1/8" PTFE tube) with a valve that can open/close the shunt.*

The reference chamber is connected with a reservoir of pristine vanadium solution (V3/4+) that is pumped continuously with a flow rate of 25 mL/min from the peristaltic pump (using peristaltic pump #14 which gives a flow rate about 9-10 times lower than tube #25 for the same pump RPM).

Individual cell voltages are monitored directly on the bipolar plates and temperature in the graphite flow body in the stack is also monitored (not indicated on figure).
Finally, the two reservoirs are also connected by a hydraulic shunt which is PTFE Tube with inner diameter of 1.6 mm and length ($l_{hs}$) of 40 cm. A valve (tube clamp on peristaltic tube piece) can open or close the shunt.

## Stack Cycling & Effect of Hydraulic Shunt on Capacity Fades

The primary objective of the cycling experiments was to investigate capacity loss over extended operation. For this reason, all charge–discharge cycles were performed using constant-current operation followed by a constant-voltage step, which provides a more accurate determination of usable capacity.

Charging was conducted at a current of 3.75 A (150 mA $cm^{-2}$) with an upper cut-off voltage of 9.6 V (corresponding to an average of 1.6 V per cell). The constant-voltage step was terminated at a cut-off current of 0.5 A (20 mA $cm^{-2}$). Discharge was performed at the same current of 3.75 A, with a lower cut-off voltage of 4.0 V (0.67 V per cell) and a constant-voltage termination current of 0.25 A (10 mA $cm^{-2}$).

The resulting charge and discharge capacities, together with the faradaic efficiency, are shown in Figure 3 as a function of cycle number. Capacity is reported as stack capacity, which is six times lower than the total electrolyte capacity due to the six cells connected in series. Each cycle required approximately 45 minutes, resulting in a total experimental duration of about seven days.

At the beginning of the experiment, the hydraulic shunt between the two electrolyte reservoirs was closed. During the initial cycles, the discharge capacity was approximately 1300 mAh, in good agreement with the theoretical value of 1501 mAh. However, a rapid capacity fade was observed, and by cycle 23 the discharge capacity had decreased to approximately 1000 mAh.

During these cycles, a measurable volume imbalance developed between the two multiport reservoirs. By cycle 23, the liquid level on the positive side was approximately 5 mm higher than on the negative side, corresponding to a volume difference of about 25 mL. This indicates that roughly 12.5 mL of electrolyte had been transferred through the membranes within the stack.

To mitigate this volumetric crossover and the associated capacity loss, the hydraulic shunt between the two reservoirs was opened at cycle 24. The liquid levels equalized within approximately one hour. Following this intervention, the stack capacity recovered rapidly over the next two to three cycles, after which a slower capacity decay was observed.

The purpose of this white paper is not to provide a detailed mechanistic explanation of these observations, but rather to demonstrate the experimental capabilities enabled by the combination of the Redox-Flow.com S-stack and multiport electrolyte reservoirs. Nevertheless, the observed capacity decay can generally be attributed to two dominant effects: (i) gradual oxidation of the vanadium electrolyte by residual oxygen and (ii) crossover of vanadium species and supporting electrolyte through the membrane.





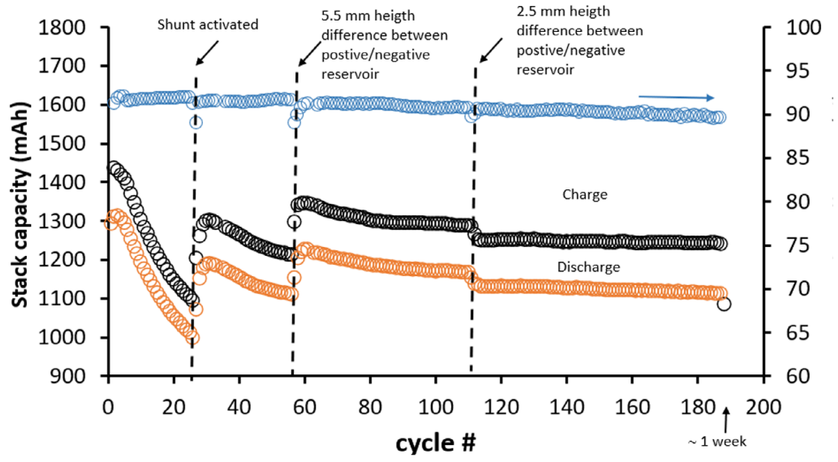



*Figure 3. Experimental stack charge/discharge capacity and faradaic efficiency as function of cycle number. Each cycle takes about 45 min and the full experiment takes about 1 week.*

In the present experiment, the electrolyte was not purged with inert gas prior to operation. Consequently, some initial oxidation occurs during the first cycles. However, because the multiport reservoirs are leak-tight, this oxidation is limited to the oxygen initially present in the system. After the first few cycles, capacity fade is therefore dominated by vanadium crossover.

Various mitigation strategies have been proposed in the literature to address this issue. One approach is the use of a hydraulic shunt between the reservoirs, which passively equalizes liquid levels and partially balances vanadium inventories between the two half-cells. As demonstrated here, such a hydraulic shunt can restore a significant fraction of the lost capacity.

The design of the shunt represents a trade-off between rapid electrolyte transfer (short shunt length and large diameter) and parasitic self-discharge currents (long shunt length and small diameter). In the present work, the shunt consists of a 40 cm PTFE tube with an inner diameter of 1.6 mm. Potential self-discharge mechanisms associated with this configuration are summarized in Table 1.

| Self discharge mechanism | Model | Estimated self-discharge current (electrolyte) |
|---|---|---|
| Electric potential difference driven shunt currents (migration) | 40 cm shunt channel leads to an ionic resistance of 7 kΩ | ~0.2 mA |
| Diffusion of charged vanadium through the shunt that recombines to 3.5+ and leads to apparent self discharge | Diffusion through 40 cm shunt | << 0.2 mA |
| Volumetric transfer (convection) of charged vanadium through the shunt that recombines to 3.5+ and leads to apparent self discharge | Osmotic and electro-osmotic effects – 0.5 mL/hour electrolyte transfer | ~25 mA |

*Table 1*

Opening the hydraulic shunt leads to a reduction in faradaic efficiency from approximately 92.0% to 91.5%. Given an average cycle duration of 45 minutes, this corresponds to an increase in stack-level self-discharge current of roughly 9 mA, equivalent to approximately 56 mA on an electrolyte basis. Migration- and diffusion-driven shunt currents are estimated to be below 0.2 mA and are therefore negligible. The dominant contribution arises from volumetric electrolyte transfer driven by osmotic and electro-osmotic effects, estimated at approximately 0.5 mL $h^{-1}$. Considering experimental uncertainties and the simplicity of the models, the observed decrease in faradaic efficiency is consistent with this mechanism.

To further demonstrate the flexibility of the multiport reservoir system, additional tests were conducted in which the relative heights of the two reservoirs were deliberately adjusted. From cycle 57, the positive reservoir was elevated by 5.5 mm relative to the negative reservoir, resulting in approximately 28 mL additional electrolyte on the negative side. This led to an immediate increase in capacity, which stabilized at around 1200 mAh until cycle 110. Subsequently, the height difference was reduced to 2.5 mm (corresponding to approximately 12 mL volume difference), producing a small but immediate decrease in capacity, after which stable cycling was again observed.

## OCV cell data – Liquid half-cell potentials

In addition to the normal stack/cell I and U monitored during the charging, the setup was also equipped with an OCV cell that can measure both the liquid potentials and overpotentials for each side as described in white paper *Measurement of Overpotentials and Liquid Potentials in Flow Batteries* (https://redox-flow.com/whitepapers/). However, in the case of a combination of a stack (rather than a single cell) and an OCV cell, it is not possible (straight forward) to measure the overpotentials individually for each side as OCV cell measures the potential of the common electrolyte and not the potential of the electrolyte inside each cell of the stack. In principle the total stack overpotential can be approximated/calculated by subtracting $N_{stack} = U_{stack} – 6xU_{ocv}$, depending on the definition of the overpotential, it should include/not include the effects of shunt currents between the cells in the stack. In any case, this is out scope of the current white paper and for this reason only liquid potentials are shown in the following and using the same definitions of the energy levels as in paper *Measurement of Overpotentials and Liquid Potentials in Flow Batteries* (https://redox-flow.com/whitepapers/). Also it is noted that the reference chamber is not placed in the center as in the previous white paper, but in the side chamber, whereby the order in the OCV cell is Negolyte || Posolyte ||‖ Reference. Extended test (not shown) of the OCV cell has shown that the order of the chamber does not play a crucial role on the stability and accuracy of the OCV cell data. On the other hand there can for reasons of cross-over in membranes in the OCV cell or compatibility of reference solutions with either the anolyte or catholyte be good reasons for changing the order of the solutions in the OCV cell.





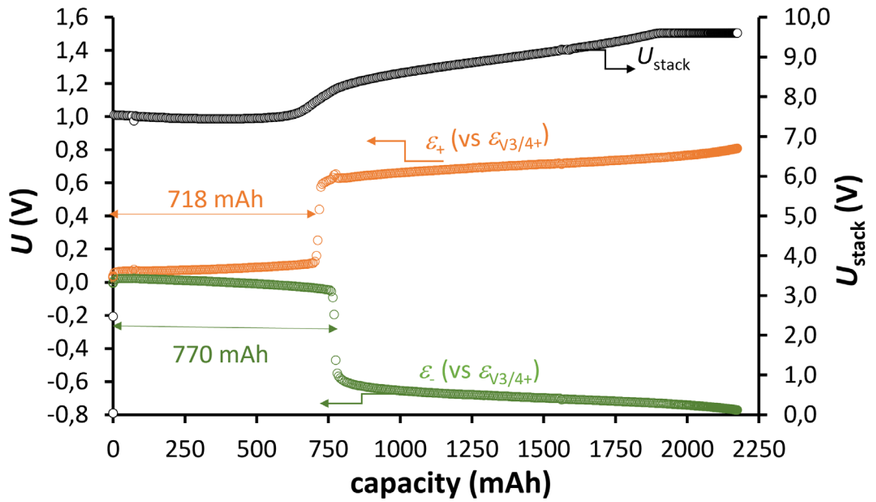



*Figure 4. Liquid potentials of the negolyte (ε-), posolyte (ε+) and stack voltage during the first cycle. All liquid potentials are against the potential of the pristine 50%/50% V3+/V4+ solution.*

The data is the same as the cycling data shown in Figure 3. The corresponding data, Figure 4, shows the liquid redox potentials of the solutions ($\varepsilon_-$ and $\varepsilon_+$) and stack voltage as function of capacity in the first cycle where the vanadium is charged from it pristine state (50%/50% V3+/V4+) to 100 % SOC. The charging is 3.75 A constant current followed by constant voltage (9.6 V) and finally terminated by a cut-of current of 0.5 A.

It is seen that $\varepsilon_-$ and $\varepsilon_+$ decreases/increases slowly, respectively, from values from about 0 V (vs. εV3/4+ because the pristine vanadium solution is used as reference solution in the OCV cell). A large decrease and increase is observed at 770 mAh and 718 mAh for $\varepsilon_-$ and $\varepsilon_+$, respectively. This plateau is related to charging V4+ -> V3+ and V3+ -> V4+ on the negative and positive side, respectively. In the ideal case where the pristine V3+/4+ solution is fully balanced 50%/50%, there is exactly 210 mL of electrolyte in each reservoir and the membrane in the stack is fully selective (i.e. no vanadium cross-over) this number should be identical and half of the theoretical capacity of 1501 mAh/2 = 750 mAh. It is out of the scope of the present white paper to understand this difference in detail. However, from specs of the vanadium electrolyte, it should be balanced within ±2% and volumes are measured with < ±1% accuracy and cannot explain the difference. Oxygen/air in the (negative side) reservoir should have little effect as air only reacts with V2+, but could nonetheless explain the slightly larger value for the negative side. However, most likely is that it is due vanadium cross-over. All vanadium species are positively charged and for this reason migration will be from the positive side to the negative side during the first initial charging cycle.

As seen from Figure 4 larger quantities are reduced on the negative side.

Another example of the unique information and benefits from mapping out liquid potentials is shown in Figure 5, that shows $\varepsilon_-$, $\varepsilon_+$ and $U_{stack}$ during charge and discharge for cycles 3, 25, 60 and 180. The purpose of this example is to demonstrate that the by mapping out the liquid levels it is possible to explain the behavior of the capacity fades/increases shown in Figure 3.

During the repeated cycling of the battery, it is obvious that vanadium quantities on each side are changed either by vanadium cross-over inside the stack or by external change of the volumes on each side. Hereby one side becomes the capacity limiting side and determines the overall capacity of the battery. However, as the vanadium concentrations are different on each side, it is not possible just from the volumes on each side to determine the vanadium capacity, however, these can be observed from the liquid potentials[1].

From cycle 3 it is seen that upon charging both negative side and positive side show a Nernstian upturn at the highest capacities, while during discharge both sides shows a clear Nernstian downturn when almost fully discharged (slightly more pronounced for the negative side) and shows that anolyte/catholyte is close to being balanced (i.e. same amount of vanadium on both sides and fully 3+/4+ at 0% SOC and fully 2+/5+ at 100 % SOC) and in agreement with this cycle being the one with the largest capacity.

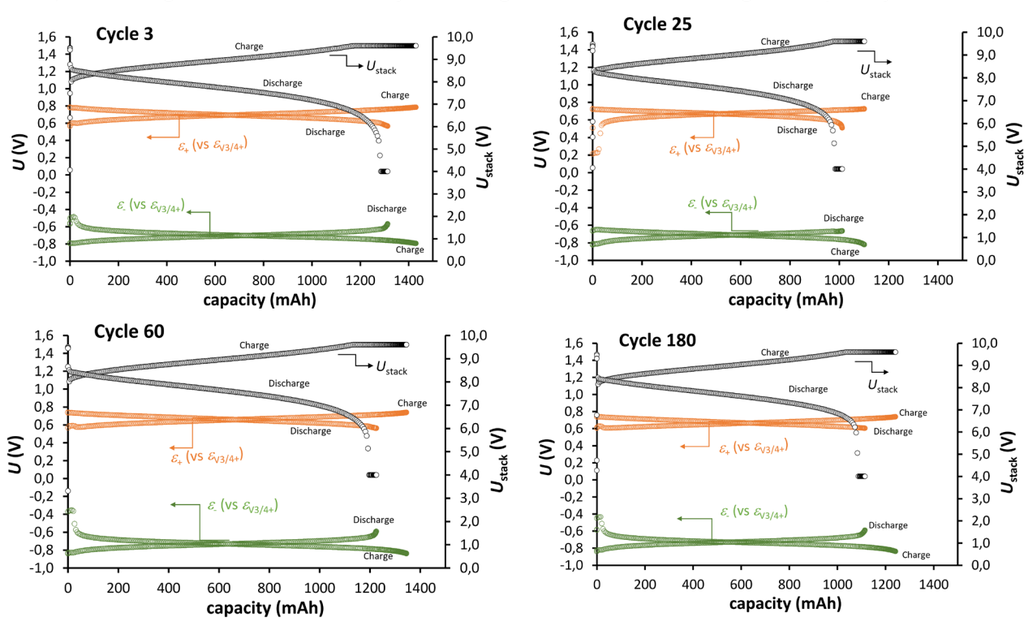



*Figure 5. Liquid potentials of the negolyte (ε-), posolyte (ε+) and stack voltage during cycles 3, 25, 60 and 180, see also Figure 3 for the corresponding capacity vs cycle number plot. All liquid potentials are against the potential of the pristine 50%/50% V3+/V4+ solution.*

1 Although the electrolyte reservoirs on were not purged with e.g. N2 before the tests, the O2 in the reservoir would only change the overall vanadium charge from +3.5 to about +3.525 and can only explain a very small fraction of the overall capacity loss in Figure 3.

In cycle 25 (top right panel in Figure 5) the capacity reaches the lowest overall capacity of about 1000 mAh, it is clear that the negative side is the capacity limiting (Nernstian downturn of $\varepsilon_-$ around 1100 mAh), while it is the positive side that is capacity limiting on discharge (Nernstian downturn of $\varepsilon_+$ around 1000 mAh). This indicates that vanadium overall has been transported to the positive side and in the same direction as the volume transfer that goes towards the positive side. Once the shunt is opened (after cycle 25) capacity is restored because vanadium is transported from the positive to the negative (capacity limiting) reservoir through the shunt.

As suggested by the results of the shunt, the capacity is limited because vanadium is continuously being transported to the positive side. This suggests that if the positive side reservoir is vertically elevated relatively to the negative reservoir, the difference in total vanadium amounts on each side can be balanced out by the height difference. After cycle 56 the positive side reservoir is raised 5.5 mm to the negative reservoir and after cycle 111 to 2.5 mm. From the bottom discharge plots in Figure 5, the potentials shows that for both cycle 60 and 180 the negative side is the capacity limiting side on both charge and discharge. Comparing this to the capacity of cycle 60 (about 1250 mAh) it is seen that it is higher than that of cycle 180 (about 1100 mAh), this suggest that the optimal height difference for balancing the vanadium between the two reservoirs is higher than 5.5 mm. Again the scope of the present white-paper is not to optimize and find the most optimal conditions, but to demonstrate the capabilities of combining the S-stack with the OCV-cell and multiport reservoir.

## Temperature during cycling

During the cycling of the battery, there was placed a battery inside the graphite flow body of the stack through ø2/ø4 holes intended for this purpose and a thermometer was placed outside for measuring the ambient temperature. Results are shown in Figure 6 which shows the temperature during charge and discharge in cycle 3. The digital resolution of the thermometers is about 0.15°C and the reason why the temperature data jumps in steps of 0.15°C. Nonetheless, it is seen that the ambient temperature is about 24.2°C through out the cycle, while the cell increases about 2°C from 26°C to 28°C during charge and decreases equivalently from 28°C to 26°C during discharge. It is fully expected that the temperature of the cell/electrolyte is higher during cycling due to joule/ohmic heating. However, the cycling of the temperature is related to the entropy effects, where charging results in a negative change of reaction entropy and therefore cools down and discharging the reaction entropy is positive and leads to heating[2].

2 Reynard, Danick, et al. "Efficiency improvement of an all-vanadium redox flow battery by harvesting low-grade heat." Journal of Power Sources 390 (2018): 30-37.

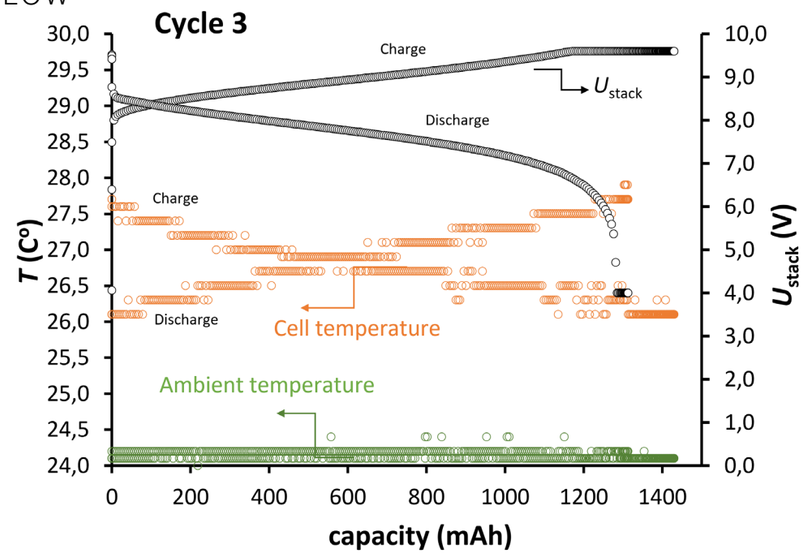



*Figure 6. Temperature inside the stack and ambient temperature during charge and discharge of cycle 3.*

## Stack polarization curve & individual cell voltages

An important key parameter for optimal stack operation and minimized corrosion in stacks is that each cell in the stack perform similarly i.e. have the same flow, voltage, current characteristics. The design of the S-stack is made in a way where individual cell voltages can be measured in the stack. This enables testing of homogeneity of electrodes in terms of both catalytic activity and hydraulic permeability. Additionally, a lower flow rate in one electrode or lower catalytic activity would lead to higher overpotential of that single cell compared to the rest in the stack.

Figure 7 shows the overall stack polarization curve at 50 % SOC with a total flow rate of 40 mL/min per cell (240 mL/min in total). Due to the very low capacity of the electrolyte (1501 mAh) compared to the size of the stack in the current test this leads to relatively high self-discharge. Additionally, even small charge/discharge times can lead to significant changes of the SOC which combined will lead to apparent non-linear polarization curves. For this reason the polarization curve is measured by constant current in 10 s followed by instant jump to next current (without rest in between). The polarization curve is constructed from the electrical current and voltage at the last data point in the 10 s sequence. Even with these short sequences there is a significant SOC change during the test and for that reason the data in Figure 7 has been corrected with the change of the OCV measured in the OCV cell. The maximum correction is 150 mV at the most negative stack current.

The polarization curve shows a linear tendency and from a linear fit a stack area specific resistance of 4.68 $\Omega$cm$^2$ ($R_i$ = 0.187$\Omega$) is found. The maximum power during charging is about 65 W and limited by the maximum charging voltage of 9.6 V. The maximum power





during discharge is equally about 65 W and is limited by the discharge current of the battery tester (10A). From the stack internal resistance (Ri) and stack OCV the maximum discharge power is estimated to be about 95 W ($P_{max}$ = $OCV^2/(4R_i)$ ) @ 22.5A. It is underlined that it is for the specific temperature and SOC only.

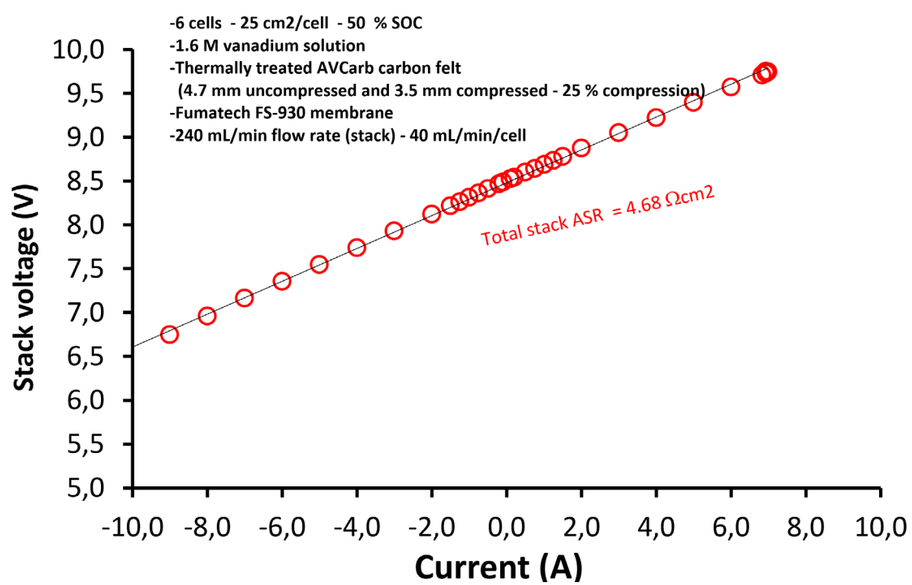



*Figure 7. Stack polarization curve at 50 % SOC.*

Figure 8 shows the individual cell voltages during the measurement of the polarization curve at 50 %. As for the stack polarization curve, they have been SOC corrected from the OCV measurement. All cells have been corrected with the same values and the maximum correction is 150 mV/6 = 25 mV. As seen all cells show a linear behavior where the ASR is in the range 0.76 $\Omega$cm$^2$ to 0.79 $\Omega$cm$^2$ and very close to each other. The values are slightly higher than single cell tests measured in the S-cell (0.56 $\Omega$cm$^2$ in white paper *Measurement of Overpotentials and Liquid Potentials in Flow Batteries* https://redox-flow.com/whitepapers/). However, in this test flow rates were higher and compression larger, both leading to lower ASRs and in agreement with present test.

The variation of the voltages between individual cells[1] shows a maximum at the highest discharge current (-400 mA/cm$^2$, 10A) where the variation is 17 mV and cell voltages are in the range from 1096 mV (cell 4) to 1079 mV (cell 5). However, more importantly during maximum charging current (280 mA/cm$^2$) where difference individual cell voltages/performance can lead to acceleration of corrosion and unwanted side reactions, the maximum variation is only 11 mV (1629 mV cell 5 and 1618 mV cell 4). For moderate current

1 Effects of stack shunt currents are not considered here. However, it will later be shown that they contribute with < 2 mV difference among cells. With the central cells having the lowest potential.

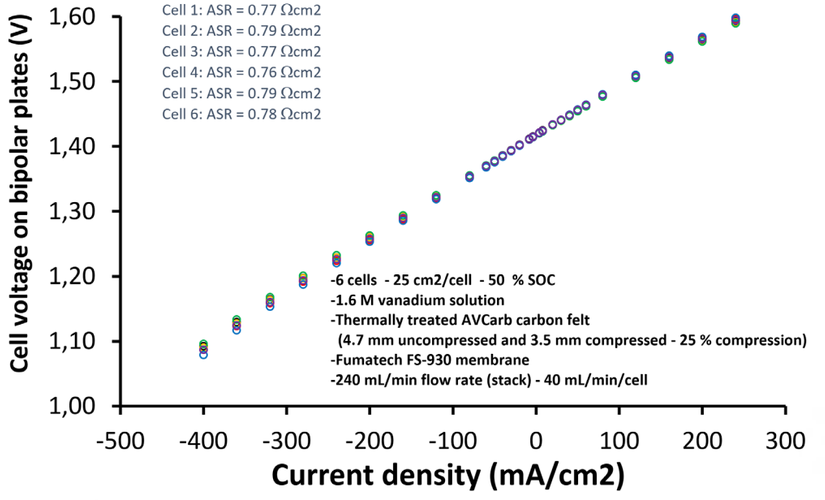



*Figure 8. Stack polarization curve with individual cell potentials in the stack. Stack polarization curve at 50 % SOC.*

densities in the range -160 mA/cm² to 160 mA/cm², the largest variation among any of the cells is only 5 mV (1291 mV cell 1 and 1286 mV cell 5). The variations are very small and demonstrates that performance between individual cells in the stack is reproducible among different cells.

The gaskets used in the assembly of the S-stack are based on gaskets with large manifold diameter (ø4) and wide shunt channel width (3.5 mm), this increases shunt currents (see next section). If an application requires very low shunt currents, gaskets with smaller manifold diameter (ø3) and smaller shunt channel width (2 mm) can be used. However, tests (not displayed) has shown that larger differences between individual cells can occur. This is attributed to larger and varying hydraulic resistance of the manifolds/channel because of geometric tolerances of the channels when stack is assembled. This leads to variations of the flow in individual cells, which again leads to different performance/voltages in individual cells.

## Shunt currents in flow battery stacks

In redox flow batteries electrochemical cells are connected in series to form a stack to increase the overall operating voltage. In most stacks this is obtained by distributing the electrolytes in parallel hydraulic circuits through common manifolds in the stack. However, the presence of electrically conductive electrolytes in shared manifolds creates unintended ionic current paths between cells. These parasitic currents, known as shunt currents, arise because adjacent cells operate at different electric potentials, which drives ionic currents between individual cells through the manifold. Shunt currents are undesirable because they directly reduce the faradaic (and energy) efficiency of the stack. In addition, shunt currents can lead to high local potentials in cells and manifolds, which may accelerate corrosion inside the stack.





A common mitigation strategy is to introduce shunt channels between each cell and the manifolds. These narrow channels increase the ionic resistance between cells, thereby reducing shunt current magnitudes. However, this approach introduces a trade-off between increasing ionic resistance that lowers shunt losses but simultaneously increases hydraulic pressure losses, leading to higher pumping power and reduced system efficiency. Stack design therefore requires careful optimization of channel geometry to balance electrical and hydraulic performance.

Direct experimental measurement of shunt currents inside operating stacks is challenging. Consequently, shunt-current modeling is the most widely used approach to quantify and analyze these losses. Among available methods, the resistor network/equivalent resistor model is particularly attractive because of relative simplicity.

In a resistor network model[1], the stack is represented as a network of electrical resistances describing ionic current paths through the electrolyte. Each cell is assigned an electrochemical potential, and shunt currents arise due to potential differences between neighboring nodes. The key parameters are:

- $R_{sh}$: shunt channel resistance between a cell and a manifold
- $R_m$: manifold segment resistance between adjacent cells
- κ: ionic conductivity of the electrolyte (S $m^{-1}$)
- Geometric parameters of channels and manifolds

By applying Kirchhoff's current and voltage laws to this network, the shunt currents in each channel and manifold segment can be calculated[2]. In the context of Redox-flow.com flow battery S-stack, $R_s$ and $R_m$ are defined by the geometry of the gaskets used in the stack and shown in Figure 9. The cell inlet/outlet shunt channels are defined by the channel length ($L_{sh}$), channel width (w), and channel height (h), filled with electrolyte of conductivity κ, the ionic resistance is given by

$$\mathrm{R_s} = \frac{\mathrm{L_{sh}}}{\kappa \cdot \mathrm{w} \cdot \mathrm{h}}$$

Similarly, the resistance of a cylindrical manifold segment of length $L_m$ and inner diameter $\mathrm{d}$ is

$$\mathrm{R_m} = \frac{\mathrm{L_m}}{\kappa\, \mathrm{A_m}} \qquad \text{with the cross-sectional area} \qquad \mathrm{A_m} = \frac{\pi \mathrm{d}^2}{4}$$

1 White, Ralph E., et al. 'Predicting shunt currents in stacks of bipolar plate cells' Journal of the Electrochemical Society 133.3 (1986): 485.

2 Chen, Yong-Song, et al. "Modeling the effect of shunt current on the charge transfer efficiency of an all-vanadium redox flow battery." Journal of Power Sources 390 (2018): 168-175.

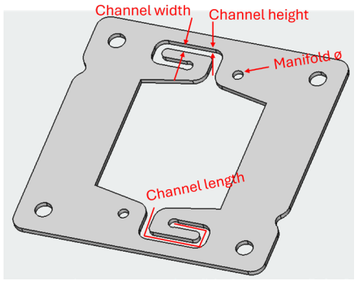



*Figure 9. Geometry of shunt channels and manifolds in flow field gaskets for S-stack.*

Typical dimensions of the shunt channel dimensions in gaskets in Redox-flow.com stacks are shown in the table below. Here the shunt channel resistance ($R_{sh}$) is calculated for 50 mm channel length (common for all gaskets) and two typical heights and widths. The electrolyte conductivity is assumed to be 280 mS/cm and taken as a typical average for vanadium flow battery electrolyte solution. It is seen that $R_s$ is typically in the range 250 – 600 $\Omega$.

| **Shunt channel resistances (κ = 280 mS/cm)** | | | | |
|---|---|---|---|---|
| **Case** | **Channel length (mm)** | **Channel height (mm)** | **Channel width (mm)** | **Shunt channel resistance / $R_s$ ($\Omega$)** |
| S1 | 50 | 1.5 | 2 | 595 |
| S2 | 50 | 1.5 | 3.5 | 340 |
| S3 | 50 | 2 | 2 | 445 |
| S4 | 50 | 2 | 3.5 | 255 |

Equally the typical manifold diameter of Redox-flow.com stack is 3mm or 4 mm. The length depends on the configuration but typically 7mm, which leads to $R_m$ in the range 20 – 35$\Omega$.

| **Manifold resistances (κ = 280 mS/cm)** | | | |
|---|---|---|---|
| **Case** | **Manifold length (mm)** | **Manifold diameter (mm)** | **Manifold resistance / $R_m$ ($\Omega$)** |
| M1 | 7 | 3 | 35 |
| M2 | 7 | 4 | 20 |

Redox-flow.com has developed a Python code that solves the non-linear equations for the equivalent resistor network model that follows the previously outlined model. The input for the model includes single cell resistance in the stack ($R_{cell}$), single cell voltage ($U_{cell}$) and electrical current applied to the stack ($I_{stack}$). The model has many output parameters, but in the present white paper it is the impact of the shunt current on the Faradaic efficiency that is in focus. These results (Figure10) shows the average shunt current as function of the number of cells in the stack for all combinations of $R_s$ and $R_m$ in the tables above. The average shunt current is defined as the sum of shunt currents between all cells divided by the number of cells in the stack and is thereby a 'measure' of the self discharge current and Faradaic efficiency. As an example, the stack cycling data shown in Fig 3 is for a stack with gaskets where $R_m$ = 20 Ohm, $R_s$ = 340 Ohm and 6 cells. From top panel of Fig 10 it is seen that for this configuration, the average shunt current is about 40 mA. If the stack is charged/discharged with 3.75 A, as in the experiment, the corresponding faradaic efficiency (FE) for the cycle would be FE = 100% - 2x40 mA/3.75 A = 97.9%. Here the x2 multiplication comes because the shunt currents are present both during charge and discharge. From the cycling data of Figure 3 it is seen that the stack faradaic efficiency is about 90 % and thereby demonstrating it is primarily determined by vanadium cross-over in the membranes inside the stack and only to a small extent due to shunt currents.





Furthermore, a typical Redox-flow.com flow field gasket is defined as Case S1/M1 (tables above) which is a 1.5 mm thick flow field gasket with small channel width and small manifold ø, where $R_s$ = 595$\Omega$, $R_m$ = 35$\Omega$. An alternative is the Case S2/M2 with 1.5 mm thickness but larger channel width and manifold ø, which results in $R_{sh}$ = 340$\Omega$ and $R_m$ = 20$\Omega$. From figure 10 it is seen that the shunt currents for all number of cells is reduced to about the half by going from gasket case S2/M2 to S1/M1. Since the smaller channel width and smaller manifold ø of case S1/M1 can lead to more uneven flow between individual cells in the stack, it is recommended to use gaskets with larger channel width and manifold ø, unless very small shunt currents are paramount for the application.

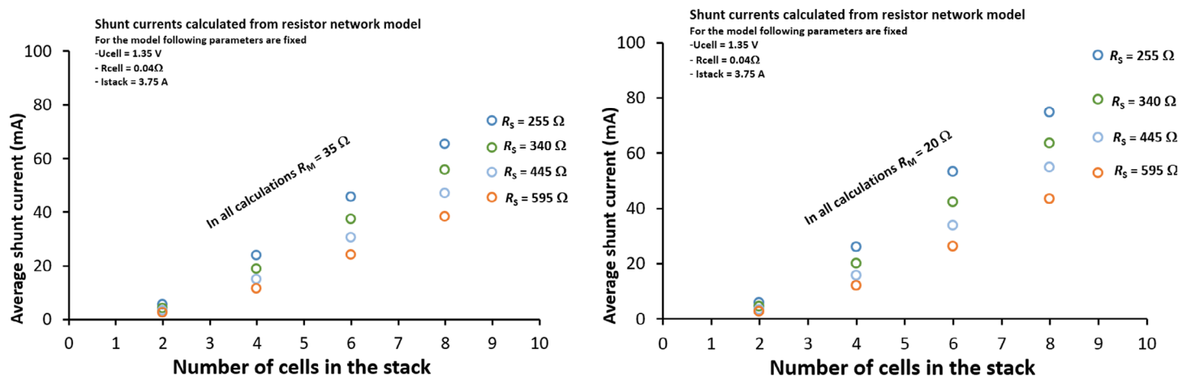



*Figure 10. Modeled average shunt currents for different manifold resistances ($R_m$) and shunt channel resistances ($R_s$) as function of number of cells in the stack.*

Experimental measurement of shunt current is challenging, nonetheless shunt current model can be used as indirect verification/comparison to experimental data. Here in particular the impact of shunt currents on the individual cell voltages can be both modeled

and measured. In general, the center cells in the stack have lower potential than the overall OCV of the electrolyte and the outer cells of the stack. The effect is typically very small (for small cell numbers) and can in general not be observed during charging/discharging as small variations of individual cell resistance have larger impact than the shunt currents. However, during stack OCV the effect of the stack current is not present. Figure 11 shows the modeled and experimental value of OCV-$OCV_0$ of the individual cells and where $OCV_0$ is the OCV of the electrolyte. It is shown for the two gasket cases from before, where it is seen that the modeling (solid lines) predicts slightly smaller potentials for the central cell that are about -0.9 mV and -1.7 mV lower for the central cells for configuration S2/M2-$R_s$ = 340Ω / $R_m$ = 20 Ω and S1/M1 - $R_s$ = 595 Ω / $R_m$ = 35 Ω, respectively. The graph also shows the experimental values (open circles) that approximately track the experimental values, but overall slightly lower than the modeled values. It is emphasized that the experimental uncertainties are relatively large (± 0.4 mV), nonetheless experimental values are systematically lower than the model. This is most likely related to difficulties of defining/calculating correct $R_s$, where the resistance related to the triangular area just before the electrolyte enters the electrode in the flow field gasket (Figure 9) is not included in $R_s$. Thus the shunt currents for the different gasket cases in Figure 11 are therefore slightly overestimated.

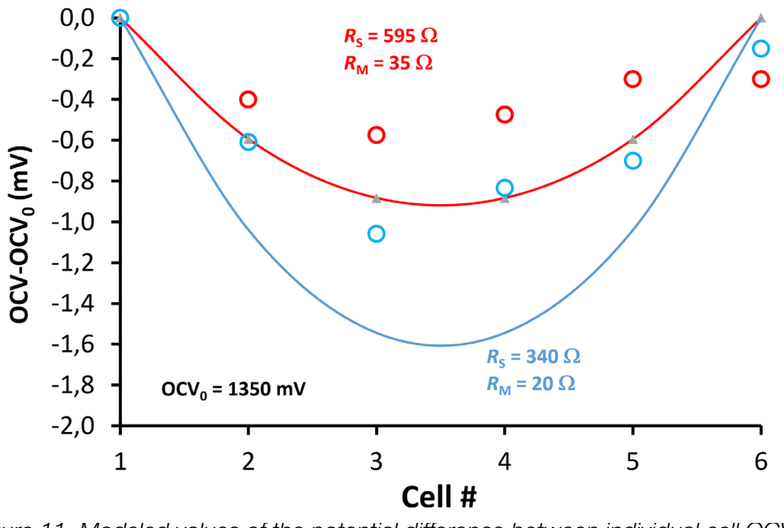



*Figure 11. Modeled values of the potential difference between individual cell OCVs and the electrolyte OCV as function of the cell in the stack (solid lines). Experimental values are shown as open circles.*

Although the shunt current model as input requires, Rcell and Istack these parameters have little influence on the average shunt currents, as the shunt currents are primarily driven by the OCV of the cell and not the smaller overpotential during charge/discharge.





Overall, the modeling is intended as a support for understanding and dimensioning of gasket for Redox-flow.com stacks. I.e. for a stack with a specific

- Number of cells
- Electrical current
- Shunt channel size/resistance
- Manifold diameter/resistance

These values can be used for estimating the overall faradaic efficiency of the stack.

## Effect of shunt currents through OCV cell

The liquid potentials shown in the previous section was recorded with the OCV cell with internal reference. The section here focuses on the impact of shunt currents through the OCV cell on the measurements of $\varepsilon_-$ and $\varepsilon_+$. With reference to Figure 1, shunt currents can go from the stack through the OCV tube with length lb, through the OCV cell and then back to the stack through the OCV tube. Due to the internal resistance of the OCV cell, this can lead to potential changes in the OCV cell and erroneous measurements of $\varepsilon_-$ and $\varepsilon_+$.

Effects of shunt currents through the cell can be observed when the stack potential is changed abrupt. E.g. by switching stack electrical current on or off. The OCV should ideally be independent of the stack current/voltage, if a response is observed this is/can be related to the shunt currents through this circuit. In an initial test (data not shown) with pristine vanadium solutions (50%/50% in $V^{3+}/V^{4+}$) where the lengths of the tubes to the OCV cell were $l_b$ ~10 cm and $l_a$ ~10 cm, the OCV response was very high, about 50 mV-100 mV for $\varepsilon_+$ and $\varepsilon_{+-}$, respectively. Therefore, to increase shunt resistance and minimize shunt currents, $l_b$ was increased to ~100 cm while $l_a$ maintained the same length. Then the test was repeated and the data shown in Figure 12. The top panel shows the response with a pristine solution, up to time 150 s the stack voltage and current is 0A/0V after which an electrical current of 3.75 A is switched on and results in a stack voltage of about 7.5 V. Here it is observed that the OCV change is about 10 mV and 30 mV for $\varepsilon_-$ and $\varepsilon_{+-}$, respectively. The middle panel shows the response after the battery has been charged to almost 100 % (in cycle 3) and is in rest mode with 0 A and with a stack OCV of 9.4 V. This is followed by a discharge with 3.75 A, whereby the stack voltage decreases to about 8.50 V. In this case the OCV change is much lower, about 1 mV and 2 mV $\varepsilon_-$ and $\varepsilon_{+-}$, respectively and almost not detectable. The change of $\varepsilon_-$ and $\varepsilon_+$ after 175 s is related to the SOC change. Finally, the bottom panel shows the same data but for cycle 180 (about 7 days after first cycle). In this case there is not observed any change of the response of the OCV cell when the stack voltage is changed.

The OCV cell does not include a specific electrode material (like carbon felt) and it is the graphite body of the OCV cell that acts as the electrode. The progression of the response

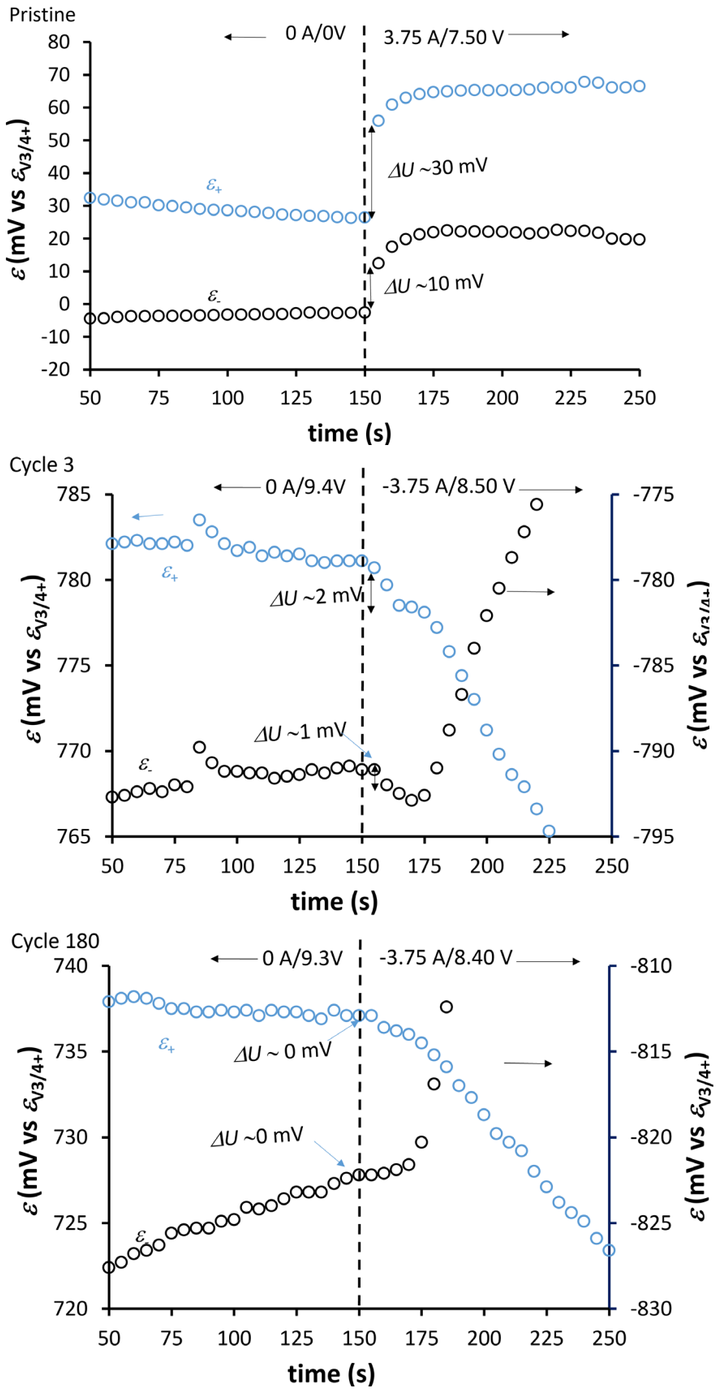



*Figure 12. Impact of abrupt changes of the stack voltage on $\varepsilon_-$ and $\varepsilon_+$ during the first initial cycling, cycle 3 and cycle 180.*





of the OCV cell can be explained by change of the internal resistance ($R_{ocv}$) of the OCV cell. I.e. the resistance of the OCV hydraulic circuit ($R_{HC, OCV}$) is so large (35 kOhm) that it determines the shunt current, whereby the OCV response scales with Rocv. Here two factors can explain the progression (i) The initial high response to shunt currents on pristine vanadium solution is a consequence of the redox reactions $V^{3+} \longrightarrow V^{4+}$ and $V^{4+} \longrightarrow V^{3+}$ are poorly catalyzed on graphite/carbon electrodes (in the OCV cell, the graphite body is used as electrode) and leads to a higher $R_{ocv}$ and explains the relatively large OCV response for the pristine solution (ii) additionally there is a clear tendency that the shunt current response of the OCV cell decreases with time ($R_{ocv}$ decreases with time). This is explained by the catalytic properties for vanadium oxidation/reduction of the graphite body of the OCV cell are improved with time and presumably by contact with the vanadium electrolyte. Overall, the recommendations for the OCV cell are:

- The hydraulic resistance of the OCV cell can lead to significant pressure losses if flow rates are > 100 mL/min. For this reason it can be advantageous to create a separate hydraulic circuit for this. Here the multiport electrolyte reservoir is an enabler for this setup.
- If large erroneous responses of $\varepsilon_-$ and $\varepsilon_{+-}$ on the cell/stack current are observed, this can be minimized by increasing the length/resistance of the hydraulic circuit for the OCV cell. This minimizes shunt currents and thereby erroneous OCV responses.
- It is generally observed that erroneous shunt current responses decreases with time (presumably to increased catalytic activity of the graphite in the OCV cell). Therefore if large erroneous OCVs are observed, it is recommend to allow the OCV cell to 'activate' for a number of cycles or hours with flow and start test when it has reached a reasonable level.

WHITEPAPER V

# X-Stacks With Flow Field And Flat Surface Current Collectors

## Introduction

Redox-flow.com has developed two X-stack types: one featuring interdigitated flow fields in the bipolar plates (X-stack-FF) and another with flat surface bipolar plates (X-stack-flat). These stacks replicate the corresponding X-cells, distinguished by either flow field or flat surface current collectors. An X-cell can be converted into an X-stack by replacing the bipolar plates and gaskets.

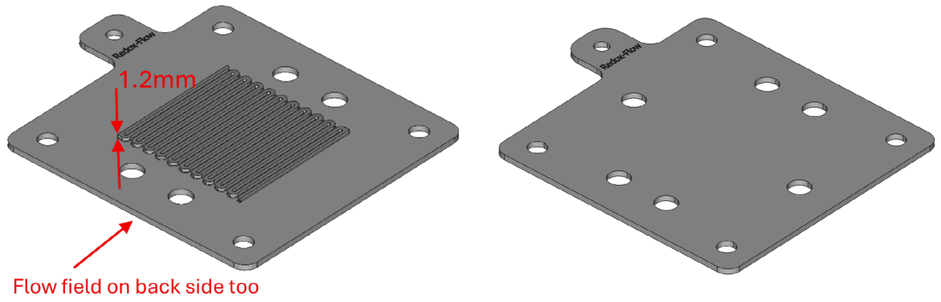



*Figure 1. Left—X-stack-FF bipolar plates with flow fields on both sides; the flow field is elevated by 1.2 mm relative to the plate surface. In contrast, the X-cell's flow field is machined into the current collector. This design minimizes side reactions, including shunt and corrosion currents. Right—flat surface bipolar plate of the X-stack-flat.*

The X-stack-flat is optimized for thick (>1 mm), porous electrodes. For thinner, denser electrodes, higher hydraulic resistance necessitates the use of interdigitated flow fields to reduce flow path lengths. These flow fields also affect mass transfer and bubble removal during electrolysis. This white paper compares the experimental performance of both stack types.

## Experimental Setup

A series of alkaline water electrolysis tests were conducted using both X-stack-FF and X-stack-flat configurations. The table below summarizes the experimental parameters, including a reference test using the X-cell with flat current collectors.

Due to the porous nature of the Zirfon separator, dual electrolyte containers cannot be used—minor pressure differences cause liquid crossover. Thus, a single, shared electrolyte reservoir is employed, resulting in mixed ($O_2$/$H_2$) gas handling.





| | X-stack-FF | X-stack-flat | X-cell (flat) |
|---|---|---|---|
| **# cells/active area per cell** | 6 / 25 $cm^2$ | 6 / 25 $cm^2$ | 1 / 6.25 $cm^2$ |
| **Current collectors/ bipolar plates** | Ni | Ni | Ni |
| **Separator** | Zirfon UTP 500+ | Zirfon UTP 500+ | Zirfon UTP 500+ |
| **Electrode/Area** | 0.25 mm Ni felt / no compression | 1.8 mm Ni foam / compressed to 1.5 mm | 1.8 mm Ni foam / compressed to 1.5 mm |
| **Electrolyte/Volume** | 6 M KOH / 500 mL | 6 M KOH / 300 mL | 6 M KOH / 100 mL |
| **Flowrate mL/min per side (stack/cell)** | 100 mL/min / 16.7 mL/min (per cell) | 75 mL/min / 12.5 mL/min (per cell) | - |
| **Temperature** | RT & 80°C | RT | RT |
| **Hydraulic circuit** | ¼" OD tubes | 1/8" OD tubes | 1/8" OD tubes |

*Table 1: Experimental conditions for each setup*

## Performance Comparison via Polarization Curves

Polarization curves were recorded for the X-stack-FF, X-stack-flat, and X-cell with flat collectors. Currents up to 10 A (400 mA/$cm^2$) were applied in fixed intervals. Voltage values were averaged over the final portion of each constant current period. Table 2 details the specific timing parameters. The cells and electrolyte were used without preconditioning.

| | X-stack-FF | X-stack-flat | X-cell (flat) |
|---|---|---|---|
| **Constant current time** | 30 s | 600 s | 300 s |
| **Time average for voltage measurement** | 5 s | 60 s | 60 s |

*Table 2: Conditions for recording polarisation curves.*

Figure 2 presents the polarization data. Maximum electrical power for the stacks approached 150 W. The power supply limited the maximum current; higher currents can be supported by the stacks.

Experimental conditions were nearly identical for the X-stack-flat and X-cell, differing only in active area: 6.25 $cm^2$ for X-cell versus 6×25 $cm^2$ for the X-stack-flat. As expected, the polarization curves are similar, with minor variations attributed to smaller experimental differences.

At 25°C, the X-stack-FF exhibited a 3 V lower stack voltage than the X-stack-flat (0.5 V per cell), largely due to the increased active area and higher density of the Ni felt electrode. While both electrodes are pure Ni, differences in the catalytic activity of the two materials could also play a role. Increasing the X-stack-FF operating temperature from 25°C to 80°C

further reduced the stack voltage by nearly 2 V at high current densities, consistent with expectations.

Iron is known to enhance catalytic activity in alkaline water electrolysis (see https://doi.org/10.1016/j.ijhydene.2025.05.262, https://doi.org/10.1016/j.coche.2023.100981 ). To investigate this, 0.2 g $FeSO_4$ was added to the electrolyte at 80°C. After 60 minutes, a new polarization curve showed an additional 1 V voltage reduction at the highest current density.

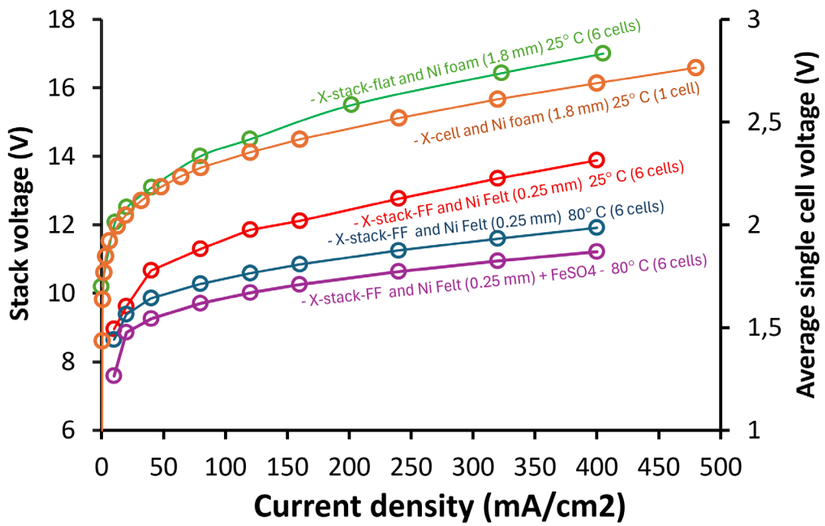



*Figure 2. Polarization curves for X-stack-flat at 25°C, X-stack-FF at 25°C and 80°C, and X-stack-FF with $FeSO_4$ at 80°C. X-cell data are included for comparison. Left axis shows total stack voltage; right axis shows per-cell average voltage.*

All tests were conducted ‘as-is’ with no performance optimization attempts (e.g., electrode type, compression, or electrolyte modification).

## Individual cell voltage monitoring

The design of the X-stacks enables easy measurements of the individual cell voltages.Figure 3 shows individual cell voltages when the X-stack-flat is operated with 40 mA/cm² at 25°C (same experimental setup as in Figure 2/ Table 1). End cells exhibit higher voltages, likely due to lower shunt current contributions compared to central cells.

In addition to assessing shunt currents, individual cell voltage measurements enable evaluation of electrode degradation, corrosion, and scaling effects.



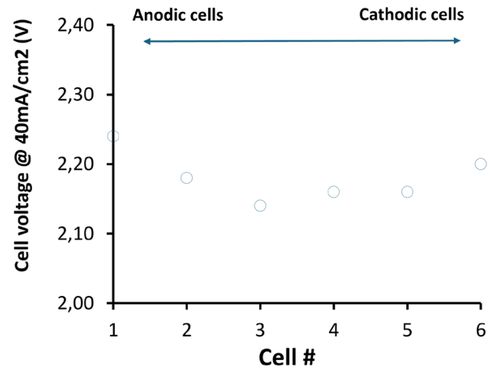



*Figure 3. Individual cell voltages in X-stack-flat at 40 mA/cm² and 25°C.*

## Faradaic efficiency

Faradaic efficiency was measured for the X-stack-flat at 25°C. As shown in Fig. 4, efficiency increased from ~90% at 10 mA/cm² to nearly 100% above 50 mA/cm², confirming minimal shunt currents due to well-designed flow channels. These values represent a lower bound, given the non-optimized electrode configuration. Estimated uncertainty: ±3%. Efficiency was determined by gas volume via water displacement.

To ensure that the stack design does not come with high shunt currents, the Faradaic efficiency of the X-stack-flat at 25°C (same experimental setup as in Figure 2/ Table 1) was measured. These data are plotted in Figure 4. It is seen that the faradaic efficiency increases from about 90 % at 10 mA/cm² to approximately 100 % faradaic efficiency >50 mA/cm². The faradaic efficiency confirms minimal shunt currents due to well-designed flow channels. Also the faradaic efficiency measured represent a lower bound, given the non-optimized electrode configuration. Estimated uncertainty: ±3%. Efficiency was determined by gas volume via water displacement.

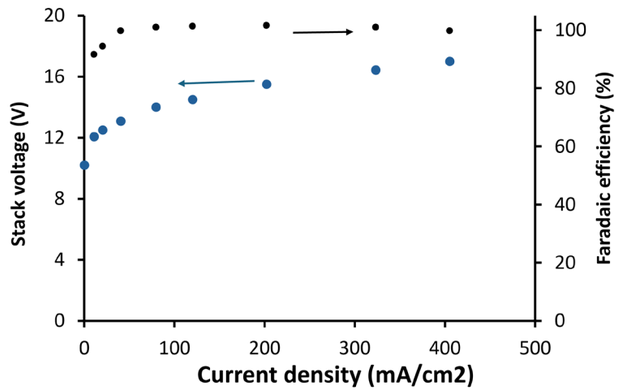



*Figure 4. Polarisation curve for the X-stack-flat (same data as in Figure 2) left y-axis and. faradic efficiency right y-axis.*

## Pressure loss in X-stack-FF

In the X-stack-FF 0.25 mm thick electrodes was used, if these were used in the X-stack-flat, this would have lead to an extremely high pressure loss in the stack because the electrode is very thin and dense. To confirm that the pressure loss in the X-stack-FF (current collectors with interdigitated flow field) is in an acceptable range, it was measured using Redox-flow-com pressure units (https://redox-flow.com/product/inline-pressure-unit-single/), that are placed at the stack hydraulic inlet and outlet.

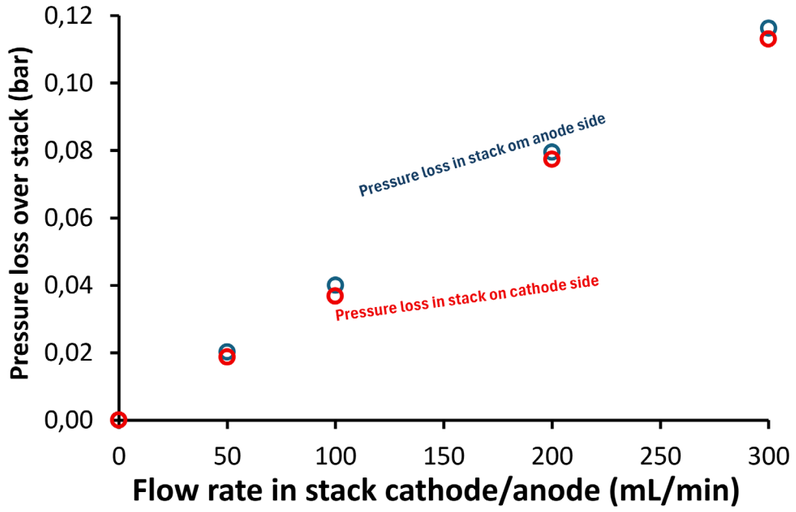



*Figure 5. Pressure loss over X-stack-FF with 6 cells and water at 25°C as function of the flow rate (individual flow rates for each side).*

Figure 5 shows the pressure loss test in the stack with pure water at 25°C. As seen the pressure loss is very small, in particular this is due to the small thickness of the electrode and the interdigitated flow fields on the bipolar plates. In this case the total pressure loss inside the stack, consists of small contributions from the flow channels in the PEEK flow body, stack manifold, shunt channels before the electrodes and the electrodes by them selves.

Although tests were done with water, similar results are expected for other electrolytes and temperature ranges and in particular excessive pressure losses (> 0.5-1 bar) inside the stack is not expected.

## Temperature control

A Redox-Flow.com heating unit (https://redox-flow.com/product-category/electrolysis/temperature-control-for-electrolysis/) was used to heat the X-stack-FF under the conditions in Table 1. The temperature of the stack was measured with a thermometer in the thermometer holder inside the stack. The temperature profile when the stack and electrolyte is heated from 25°C to 80°C is shown in Figure 6. It is seen that the stack and 500 mL electrolyte reaches the 80°C  setpoint within less than 45 min.

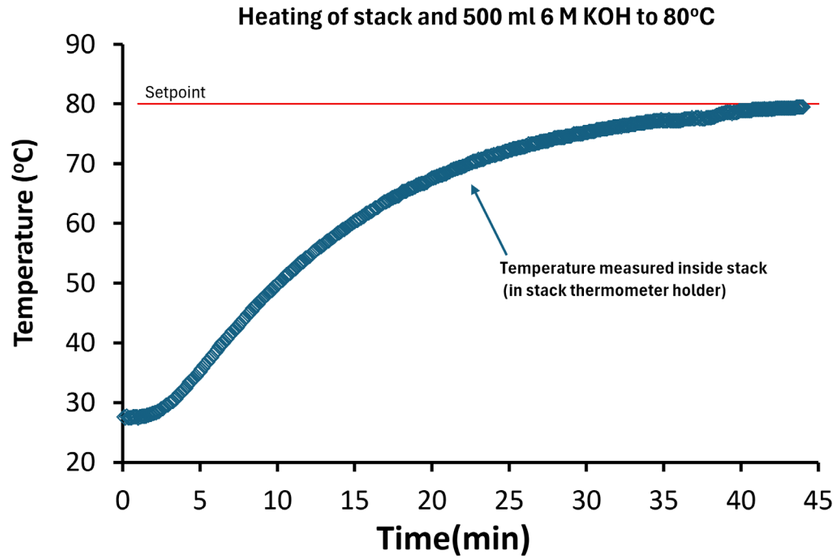



*Figure 6. Temperature profile of the stack (measured with a thermometer in the thermometer holder inside the stack) versus time.*

## Summary

The X-cell and X-stack product family from Redox-flow.com represents a uniquely versatile and comprehensive platform for electrolysis R&D. This modular system spans from single cells with an active area of 6.25 $cm^2$ to multi-cell stacks with up to 25 $cm^2$ per cell, with configurations scalable to nearly 200 $cm^2$ in total active area.

**Key features include:**

- ***Interchangeable current collectors*** - Available as flat surfaces or with interdigitated flow fields, enabling operation with both very thin and thick electrodes. This supports studies on mass transfer, bubble transport, and electrode optimization.
- ***Individual cell voltage monitoring*** - Facilitates advanced diagnostics such as analysis of shunt currents, corrosion effects (in stacks), overall electrode degradation, and system upscaling.
- ***Polymer-based system design*** - All components apart from current collectors and electrodes are made from polymers, allowing critical investigations of metal ion impurity effects on catalytic properties and electrode performance.
- ***Integrated testing accessories*** - Accessories like the heating unit and inline pressure sensors support testing under elevated temperatures and facilitate measurement of the hydraulic characteristics of electrodes and bipolar plates.

Together, these features provide a complete, adaptable R&D environment for rigorous investigation and optimization of virtually any type of electrolysis system.

WHITEPAPER VI

# Accurate Overpotential and Reference Electrode Measurements in Water Electrolysis Using the 1 cm² M-Cell

## Introduction

This whitepaper concerns the M-cell, a multipurpose 1 cm² electrochemical research cell developed by Redox-Flow.com (www.redox-flow.com). The M-cell is designed for maximum flexibility: by changing the gasket configuration and the current collectors, a single compact platform can be reconfigured into closed cell, open cell, half-cell, and three-compartment setups. Its small 1 cm² active area makes it particularly well suited for testing and screening of catalysts, novel membranes, and other materials that are only available in limited quantities. A key unique feature of the cell is its advanced reference electrode system, in which one or more Luggin capillaries ensures well-defined reference electrode locations inside the cell with a spatial precision better than approximately 0.2 mm.

Because of this modularity, the M-cell can be applied across a wide range of electrochemical disciplines. The same hardware can be configured for alkaline water electrolysis (AWE), anion-exchange-membrane (AEM) and proton-exchange-membrane (PEM) electrolysis, redox flow batteries, $CO_2$ reduction, and electrodialysis.

The present whitepaper focuses exclusively on alkaline water electrolysis, studied in three different cell configurations (see manual https://redox-flow.com/product/m-cell-full-cell-2/ for more information on the configurations):

- Part 1 – Open cell configuration with one common reference electrode
- Part 2 – Closed cell configuration with one common reference electrode
- Part 3 – Closed cell configuration with two independent reference electrodes

This whitepaper demonstrates the use of the 1 cm² M-cell, focusing on accurate reference electrode measurements and on the challenges that gas bubbles create in the Luggin capillaries. During electrolysis, bubbles can enter or fully block the capillaries and add noise to the measured potentials; the work shows how controlled electrolyte flow in both the main cell circuit and the reference electrode circuit keeps these measurements stable. Performance tests — polarisation curves, separated hydrogen and oxygen overpotentials, temperature control, and an iron-addition example — are also included.

Each of the three parts can be read separately but refers to the others where relevant, and is best read together with the M-cell assembly manual (under Resources at https://redox-flow.com/product/m-cell-full-cell-2/).





## Key Takeaways

The main conclusions and practical recommendations from the tests presented in this whitepaper are summarised below.

1. Bubble formation can be a significant source of noise in both the cell potential and the reference electrode measurements. The most effective way to mitigate this is to maintain electrolyte flow through the reference electrode hydraulic circuit (the Luggin capillaries), which clears bubbles from the capillaries and keeps the potential measurement stable.
2. The reference electrodes of the M-cell can be configured in almost endless ways. In many cases it is advantageous to connect the reference electrode circuit to the electrolyte beakers/reservoir for continuous circulation, creating a more stable system. This can introduce shunt currents and voltages in the reference electrode circuit, but in most cases these can be minimised through careful selection of the tube length and inner diameter.
3. Establishing flow in the reference electrode circuit does not necessarily require a third pump. It can be achieved either by adding a third pump head to the existing peristaltic pump or by exploiting the pressure differences already present in the main hydraulic circuit.
4. Before relying on reference electrode measurements, a detailed analysis of the hydraulic and electronic circuit should be carried out to identify potential shunt currents and their implications for the measured potentials.

Several of these points are discussed in further detail in the M-cell assembly manual (available under Resources at https://redox-flow.com/product/m-cell-full-cell-2/), which should be consulted alongside this whitepaper.

## Part 1 – Open cell configuration with one common reference electrode

All experiments were performed using commercially available electrochemical research equipment from www.redox-flow.com. The electrochemical cell used in this study was the 1 cm² M-cell, a multipurpose electrochemical test cell designed for advanced electrochemical investigations and flexible reference electrode configurations (Fig. 1.1). The cell includes integrated ports for electrolyte flow and for Luggin capillary reference electrode measurements. The reference electrode (Hg/HgO) was connected through a flow-through reference electrode unit positioned outside the cell and connected to the cell via Luggin capillaries.

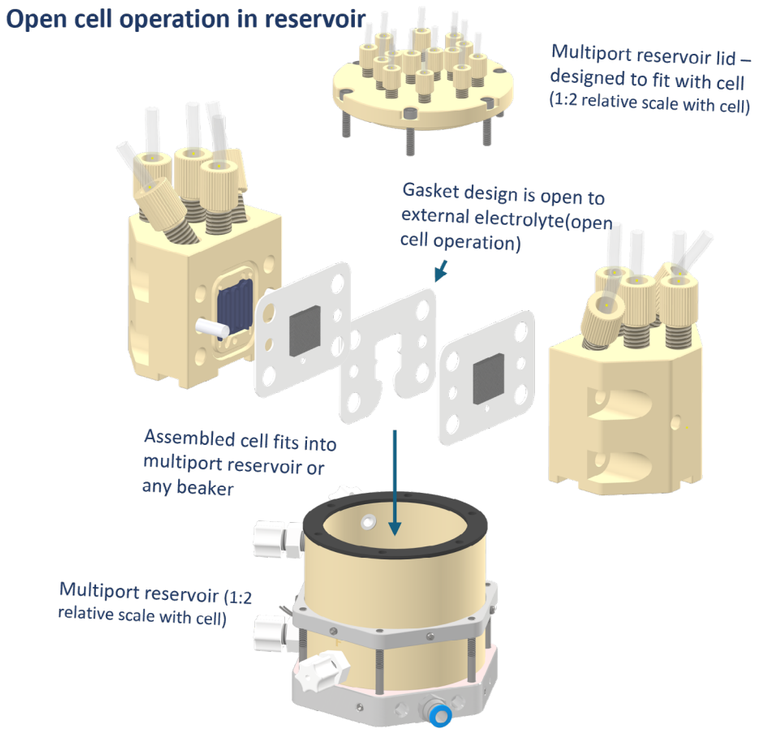



*Figure 1.1 – General configuration of the 1 cm² M-cell operated in an open reservoir configuration. The cell is immersed in a multiport electrolyte reservoir containing 6 M KOH while electrolyte is circulated through the cell via external tubing connections. The configuration enables simultaneous electrochemical measurements and controlled electrolyte flow through the cell and reference electrode circuits.*

The test setup consisted of a 6 V / 5 A power supply equipped with an AUX measurement unit that records potentials from reference electrodes and temperature sensors. All voltage and current data were recorded with a resolution of 1 s. Nickel electrodes with a porosity of 150 ppi and a thickness of 1.7 mm were used as both anode and cathode. The electrolyte was 6 M KOH.

The M-cell was operated in an open cell configuration (see assembly manual for M-cell for more details – https://redox-flow.com/product/m-cell-full-cell-2/ ) and placed inside a multiport electrolyte reservoir containing the electrolyte solution. In this configuration the cell was immersed in the electrolyte reservoir while electrolyte was continuously circulated through the cell using external tubing connections. Two peristaltic pumps were used to control electrolyte flow. The first pump, equipped with two pump heads, circulated electrolyte through the main cell circuit. This circuit supplied electrolyte to the cell through the main inlet ports and returned it to the reservoir. The second pump was used to circulate electrolyte through the reference electrode circuit connected to the Luggin capillaries.





The hydraulic layout of the system is illustrated in Fig. 1.2. In this figure the blue circuit represents the main electrolyte flow through the electrochemical cell, while the red circuit represents the reference electrode circuit connected to the Luggin capillaries. Electrolyte in both circuits was pumped from the reservoir into the cell to minimise the influence of gas bubbles formed during electrolysis.

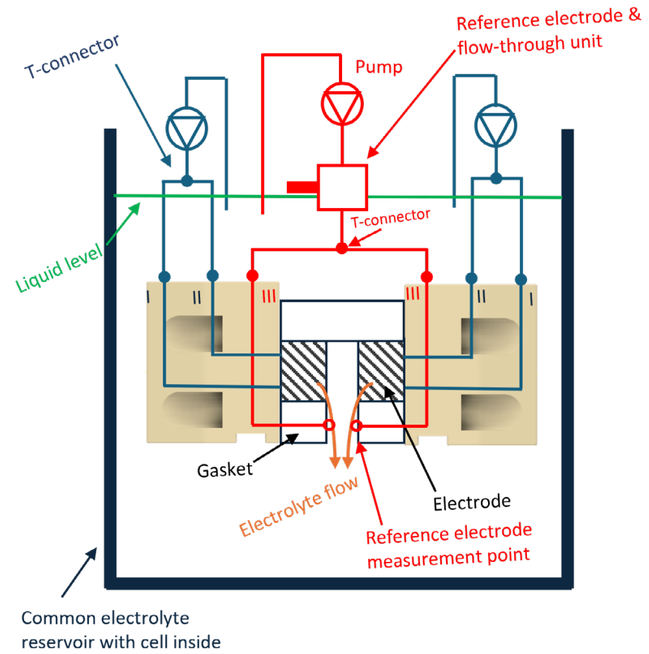



*Figure 1.2 – Hydraulic layout of the experimental setup. The blue circuit represents the main electrolyte flow through the electrochemical cell, while the red circuit represents the reference electrode circuit connected to the Luggin capillaries. Electrolyte is pumped from the reservoir into both circuits using peristaltic pumps in order to minimize bubble accumulation and ensure stable potential measurements. Space between electrodes is 0.5 mm.*

## Effect of Bubbles on Cell Potential Measurements

Figure 1.3 shows the measured cell potential $U_{cell}$ as a function of time for different electrolyte flow rates in the main cell circuit. Also, two different configurations were investigated for the reference electrode circuit. One with no electrolyte flow was applied through the reference electrode circuit (0 mL $min^{-1}$), the other with a flow rate of 1.5 mL $min^{-1}$. Unlike conventional polarisation curves where voltage is plotted as a function of current density, the data here are presented as a time series in order to highlight the influence of bubble formation on the stability of the voltage signal. All experiments were performed at room temperature.

At low current densities $U_{cell}$ remains relatively stable with minimal fluctuations. For example, at a flow rate of 25 mL min$^{-1}$ the voltage signal shows almost no measurable noise up to approximately 250 mA (250 mA cm$^{-2}$). In this regime the gas production rate is relatively low and bubbles formed at the electrode surface are transported away by the electrolyte flow. As the current increases, the rate of gas evolution also increases and the measured voltage begins to exhibit noticeable fluctuations/noise in $U_{cell}$ that becomes very pronounced at the highest current densities. The inset of Fig. 1.3 shows a zoomed-in plot of the time series data for 1400 mA. The standard deviation of the measured cell voltage, denoted by σ, is used as a quantitative measure of the noise level in the signal. The data demonstrate that the standard deviation decreases with increasing electrolyte flow rate through the cell.

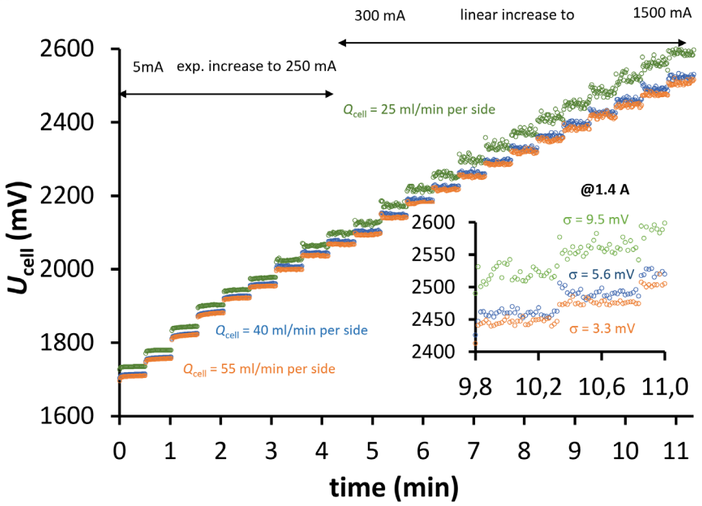



*Figure 1.3 – Measured cell potential $U_{cell}$ as a function of time for different electrolyte flow rates in the main cell circuit during alkaline water electrolysis in 6 M KOH at room temperature. Increased electrolyte flow rates reduce fluctuations in the measured cell voltage by improving bubble removal from the electrode surfaces. The inset shows a magnified region at high current where the standard deviation σ of the voltage signal is used to quantify measurement noise.*

This trend can be explained by higher electrolyte flow rates transporting bubbles away more efficiently, thereby reducing their influence on the local current distribution and effective resistance of the solution. The gas bubbles are non-conductive, so when they occupy space in the flow path, they displace the ionically conductive liquid and force the current through a more tortuous path, resulting in a varying ohmic resistance. As a result, the measured cell potential becomes more stable and the noise level decreases.





## Effect of Bubbles on Reference Electrode / Overpotential Measurements

Figure 1.4 shows the measured overpotentials at room temperature for hydrogen evolution and oxygen evolution obtained using one common reference electrode (whereby $U_{cell} = 1.23\ \mathrm{V} + \eta_{H2} + \eta_{O2}$ all times). Similar to Fig. 1.3, the data are presented as a function of time in order to focus on the fluctuations in the measured potentials. Three different electrolyte flow rates in the main cell circuit were investigated. For each of these flow rates, measurements were performed both with and without electrolyte flow in the reference electrode circuit. It is emphasized that these measurements are not intended as performance tests of the electrochemical system. Instead, the purpose of the experiments is solely to investigate how bubbles influence the noise level in reference electrode measurements.

The results show two clear trends. First, the presence of electrolyte flow in the reference electrode circuit generally reduces the noise in the measured overpotentials. When electrolyte is pumped through the Luggin capillary circuit, bubbles that might otherwise enter or accumulate in the capillaries are removed, leading to a more stable potential measurement.

Second, increasing the electrolyte flow rate in the main cell circuit also reduces the noise in the measured potentials. Higher flow rates enhance the removal of bubbles from the electrode surfaces and electrolyte channels and reduce fluctuations in the measured cell voltage $U_{cell}$. The observed noise in reference electrode measurements can therefore be attributed to two main effects. The first contribution originates from fluctuations in the cell potential $U_{cell}$. Since overpotentials are partly related to the measured cell voltage, any noise in $U_{cell}$ will propagate into the calculated electrode potentials. The second contribution arises from the interaction of bubbles with the Luggin capillary and reference electrode circuit itself. Bubbles generated during electrolysis may enter the capillary system or temporarily block the electrolyte pathway between the cell and the reference electrode. These disturbances introduce additional noise in the measured potential signal.

A small intrinsic measurement noise may also be present due to the high impedance of the reference electrode, typically on the order of 5–10 kΩ. The magnitude of this noise depends highly on the voltage measurement electronics quality. However, in present context the experiments demonstrate that the dominant contribution to the observed noise originates from bubble formation and its interaction with both the main electrolyte circuit and the reference electrode circuit.

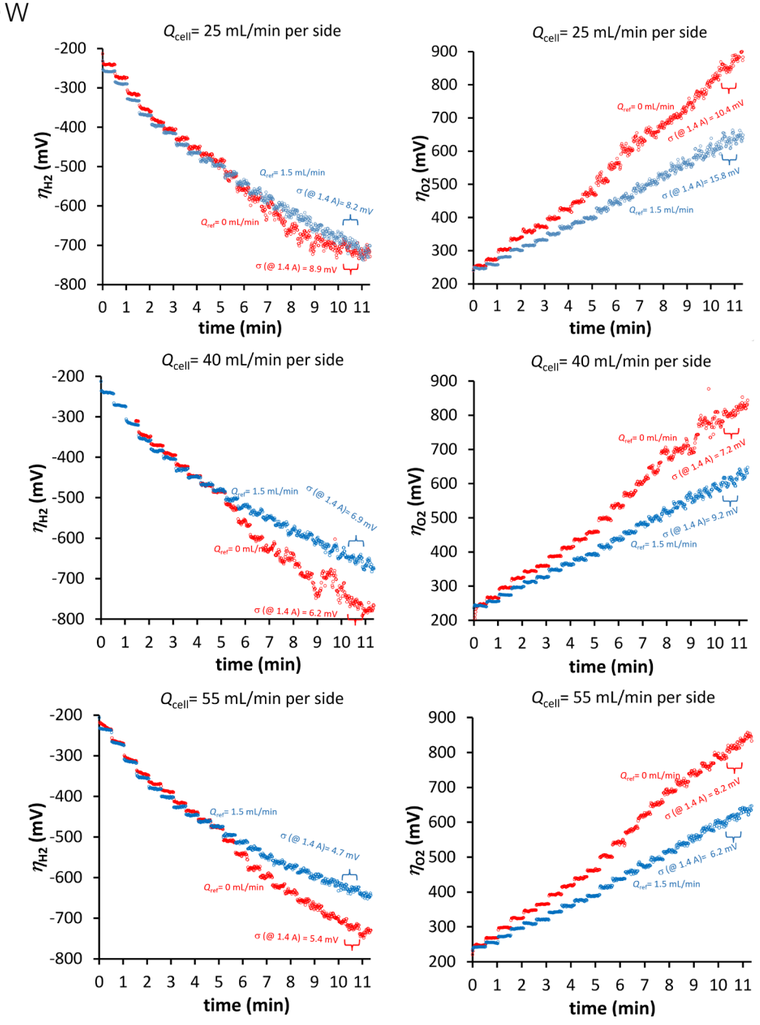



*Figure 1.4- Measured hydrogen and oxygen overpotentials at room temperature obtained using a common Hg/HgO reference electrode under different electrolyte flow conditions. Measurements were performed both with and without electrolyte flow through the reference electrode circuit. Continuous flow through the Luggin capillaries significantly reduces noise in the measured potentials by preventing bubble accumulation in the reference electrode pathway.*

## Stability of reference electrode measurements

The results above show that noise in potential measurements can originate both from bubbles formed at the electrode surfaces and from bubbles entering the Luggin capillary / reference electrode circuit. The short-term measurements clearly demonstrate these effects, but for practical electrochemical testing it is equally important to assess whether the reference electrode measurements remain stable over longer timescales.

An example of this is shown in Fig. 1.5, where the same experimental configuration was operated at 90 °C and a constant current of 1000 mA (1000 mA $cm^{-2}$). The measured cell potential, $U_{cell}$ , remains relatively stable throughout the experiment, and the hydrogen and oxygen overpotentials, $\eta_{H2}$ and $\eta_{O2}$, are also initially stable. During the first part of the experiment there is no flow through the reference electrode circuit. After approximately 12 min, the measured $\eta_{H2}$ and $\eta_{O2}$ begin to drift and become highly noisy, even though $U_{cell}$ itself remains stable. This shows that the instability is caused primarily by bubbles blocking the Luggin capillaries. When the pump for the reference electrode circuit is switched on, the measured overpotentials immediately become stable again and return to the same magnitude as before the drift started.

Together, the results show that bubble formation influences both cell potential and reference electrode measurements. The effect is impossible to predict, but depends on factors such as the cell flow rate, temperature, electrode properties, and gasket geometry. In general, higher cell flow rates and higher temperatures reduce the effect of bubbles. For long-term measurements with reference electrodes flow in the reference electrode circuit ensures stability.

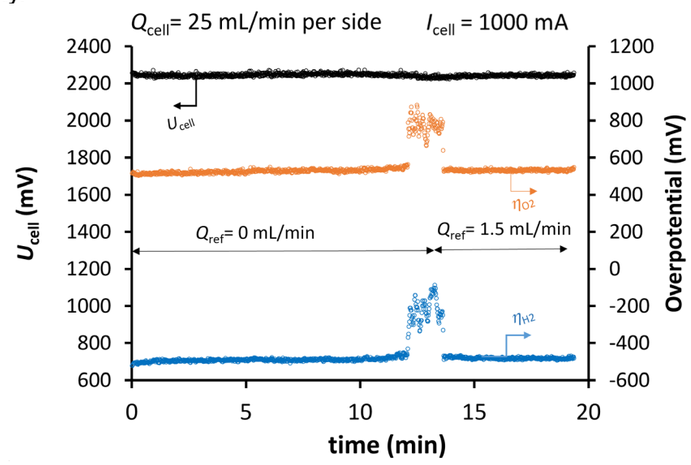



*Figure 1.5 – Cell potential, $U_{cell}$ , and overpotentials for hydrogen evolution, $\eta_{H2}$ , and oxygen evolution, $\eta_{O2}$ , as a function of time at 90 °C and a constant current of 1000 mA (1000 mA $cm^{-2}$). During the first approximately 14 min, no flow is applied through the reference electrode circuit. After this point, flow through the reference circuit is switched on. The data show that blockage of the Luggin capillaries leads to unstable and noisy overpotential measurements, while flow through the reference circuit restores stable signals.*

If long-term stable reference electrode measurements are required, flow through the reference electrode circuit is needed, either by a pump or a person operating a syringe during the experiment. A direct placement of the reference electrode inside the flow cell is not an attractive alternative. First, bubbles may also block the frit of a directly inserted reference electrode. Second, operation at elevated temperatures such as 90 °C may damage or shorten the lifetime of the reference electrode. Third, the Luggin capillary approach allows

highly localized potential measurements with a spatial resolution better than approximately 0.2 mm, whereas a directly inserted reference electrode would provide a much less well-defined measurement position.

## Internal consistency of reference electrode measurement points

This section demonstrates the accuracy and positional consistency of the measurement points defined by the Luggin capillaries. Fig. 1.6 illustrates an experimental setup with two reference electrodes that are connected to individual Luggin capillaries with measurement points located at the surfaces of the anode and cathode, respectively. The distance between the two measurement points is defined by a spacer gasket of thickness 0.55 mm, which also corresponds to the inter-electrode spacing in the cell. The voltage difference between the two reference electrodes, $\Delta U_{ref}$, is measured as a function of current in order to determine the electrolyte resistance between these two precisely defined points.

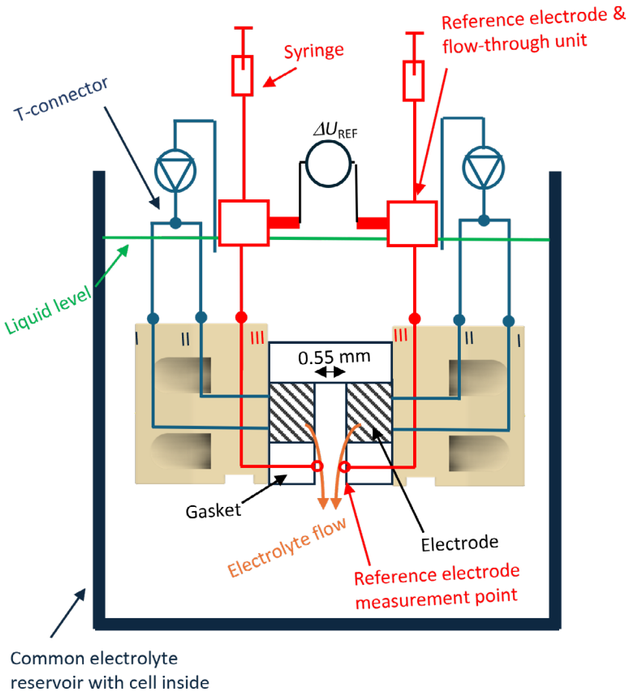



*Figure 1.6 – Hydraulic layout used for evaluating the internal consistency of the reference electrode measurement points. The blue circuit represents the main electrolyte flow through the cell, while the red circuits represent the two individual reference electrode circuits connected to Luggin capillaries on the anode and cathode side. The potential difference between the two reference electrodes, $\Delta U_{ref}$, is measured. The distance between the electrodes is 0.55 mm, which also defines the spacing between the two reference electrode measurement points.*





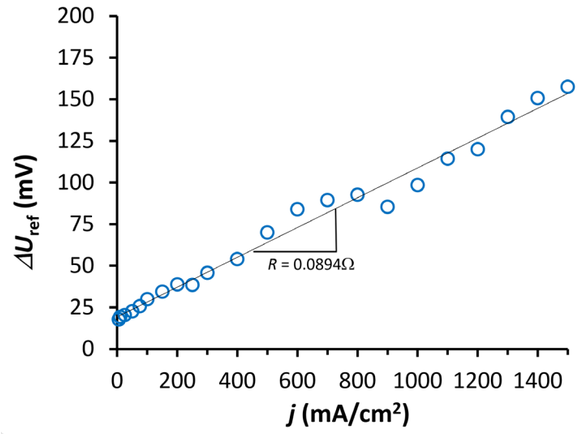



*Figure 1.7 – Measured voltage difference between the two reference electrodes, $\Delta U_{ref}$, as a function of current density in 6 M KOH at room temperature. The slope of the linear relationship gives the electrolyte resistance between the two measurement points and thereby enables calculation of the electrolyte conductivity over the defined 0.55 mm distance.*

Figure 1.7 shows $\Delta U_{ref}$ as a function of current density. From the slope of this relationship, an electrolyte resistance of 0.0894 Ω is obtained. Using the known distance between the measurement points, $L$ = 0.55mm, and a cross-sectional area of 1 cm², the electrolyte conductivity, κ, can be calculated from

$$\kappa = \frac{L}{RA}$$

where $R$ is the measured resistance and $A$ is the cross-sectional area. Inserting the experimental values gives an electrolyte conductivity of approximately 0.61 S cm$^{-1}$.

This value is in very close agreement with literature values for 6 M KOH at room temperature, which are around 0.63 S cm$^{-1}$. [1] The agreement is well within normal experimental uncertainty and strongly supports that the reference electrode measurement points are both spatially well defined and internally consistent. In other words, the Luggin capillaries do not merely provide qualitative potential measurements, but can define localised measurement positions with sufficient precision to reproduce the expected electrolyte conductivity over a sub-millimetre distance. This ability to make accurate local measurements on the sub-mm scale is a central advantage of the M-cell design.

## Performance tests

The preceding sections have focused on demonstrating the capabilities and limitations of the 1 cm² M-cell in terms of noise and stability. The present section focuses on the electrochemical performance that can be obtained with the setup. Using the experimental configuration shown in Fig. 1.2, polarisation curves together with hydrogen and oxygen

overpotentials were measured by recording the potentials as a function of time at a series of applied currents. Each current step was held for 60 s, and the reported values were constructed as the average of the final 30 s of each step. The present data compare operation at room temperature (RT, 22 °C) and 90 °C, and the results are shown in Fig. 1.8.

Overall, the polarisation curves at room temperature and 90 °C show similar shapes, but the total cell potential at 90 °C is approximately 200 mV lower across much of the investigated current range, as expected from the improved electrochemical kinetics and electrolyte transport at elevated temperature. When the overpotentials are separated into contributions from the hydrogen evolution reaction and the oxygen evolution reaction, it becomes clear that the main improvement comes from the hydrogen side.
The oxygen overpotential remains relatively similar at room temperature and 90 °C, whereas the hydrogen overpotential decreases by approximately 200 mV upon heating.

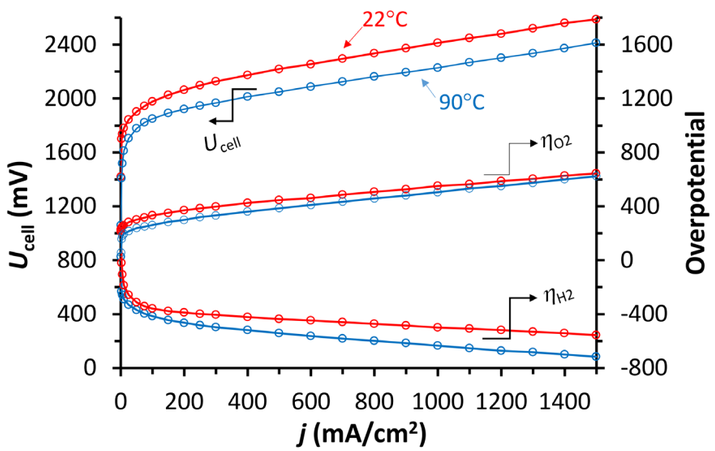



*Figure 1.8 – Polarization curve and corresponding hydrogen and oxygen overpotentials measured using the setup shown in Fig. 1.2. Each data point is constructed from the average of the final 30 s of a 60 s current step. Measurements were performed in 6 M KOH at 22 °C and 90 °C. The comparison demonstrates the performance capability of the 1 cm² M-cell and shows the reduction in total cell potential and especially hydrogen overpotential at elevated temperatures.*

The main point of this section is not to make conclusions on optimisation, but rather to demonstrate the performance measurement capabilities of the setup. Here, the key capability highlighted is the ability to measure the hydrogen and oxygen overpotentials accurately and simultaneously on both sides using a common reference electrode in a compact 1 cm² cell. Combined with the multiport reservoir and its integrated temperature-control capability, this provides a highly flexible tool for studying or screening electrode materials, catalyst activity, activation behaviour, and temperature effects under well-defined electrochemical and hydrodynamic conditions, and for comparing anode and cathode behaviour





within the same platform.

## Heating with multiport reservoir

Heating and accurate temperature control are often overlooked or poorly integrated in commercial and state-of-the-art electrochemical test systems. In contrast, the Redox-Flow.com multiport reservoir is designed with integrated heating possibilities and can be placed directly on standard laboratory hotplates equipped with an external thermometer and temperature controller. This makes elevated-temperature electrochemical testing simple and robust.

For the room-temperature and 90 °C experiments shown in Fig. 1.8, temperature control was achieved using a 600 W plate heater with an external thermometer / temperature controller. The temperature evolution during heating to the 90 °C setpoint is shown in Fig. 1.9. One thermometer was placed in the 316L heating block, which is in direct contact with the heater plate. A second thermometer was placed directly in the 6 M KOH electrolyte and used as the controlling thermometer. A third thermometer measured the ambient temperature outside the reservoir. The data show that the target temperature of 90 °C is reached rapidly, in practice after only about 20 min. This demonstrates that the combined reservoir and heating-block design provides efficient heat transfer to the electrolyte while maintaining straightforward external control of the operating temperature.

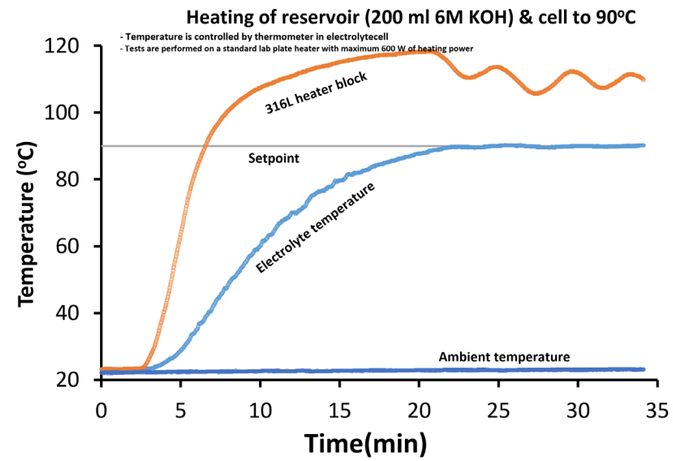



*Figure 1.9 – Temperature profiles measured during heating of the multiport reservoir system to 90 °C using a 600 W laboratory plate heater with external temperature control. The curves show the temperature in the electrolyte, the 316L heating block in contact with the hotplate, the setpoint, and the ambient temperature. The data demonstrate that the electrolyte reaches the target temperature rapidly, within approximately 20 min.*

## Part 2 – Closed cell configuration with one common reference electrode

All experiments were performed using commercially available electrochemical research equipment from www.redox-flow.com. The electrochemical cell used in this study was the 1 $cm^2$ M-cell, a multipurpose electrochemical test cell designed for advanced electrochemical investigations and flexible reference electrode configurations (Fig. 2.1). The cell includes integrated ports for electrolyte flow and for Luggin capillary reference electrode measurements. The reference electrode (Hg/HgO) was connected through a flow-through reference electrode unit positioned outside the cell and connected to the cell via Luggin capillaries.

The experimental setup consisted of a 6 V / 5 A power supply equipped with an AUX measurement unit that records potentials from reference electrodes and temperature sensors. All voltage and current data were recorded with a resolution of 1 s. Nickel electrodes with a porosity of 150 ppi and a thickness of 1.7 mm were used as both anode and cathode. The electrolyte was 6 M KOH.

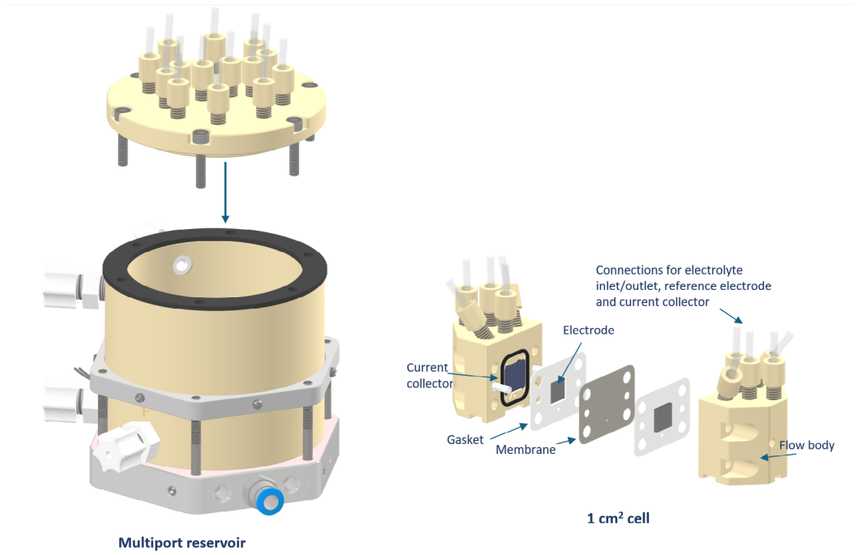



*Figure 2.1 – General configuration of the 1 $cm^2$ M-cell operated in an closed cell configuration. The cell is connected to a multiport electrolyte reservoir containing 6 M KOH while electrolyte is circulated through the cell via external tubing connections. The configuration enables simultaneous electrochemical measurements and controlled electrolyte flow through the cell and reference electrode circuits.*

The M-cell was operated in a closed cell configuration and placed inside a multiport electrolyte reservoir containing the electrolyte solution (see M-cell assembly manual for more details – https://redox-flow.com/product/m-cell-full-cell-2/ ). In this configuration the cell was connected to the electrolyte reservoir while electrolyte was continuously circulated through the cell using external tubing connections. Two peristaltic pumps were used to control electrolyte flow. The first pump, equipped with two pump heads, circulated electrolyte through the main cell circuit. This circuit supplied electrolyte to the cell through the main inlet ports and returned it to the reservoir. The second pump was used to circulate electrolyte through the reference electrode circuit connected to the Luggin capillaries. The hydraulic layout of the system is illustrated in Fig. 2.2. In this figure the blue circuit represents the main electrolyte flow through the electrochemical cell, while the red circuit represents the reference electrode circuit connected to the Luggin capillaries. Electrolyte in both circuits was pumped from the reservoir into the cell to minimise the influence of gas bubbles formed during electrolysis.

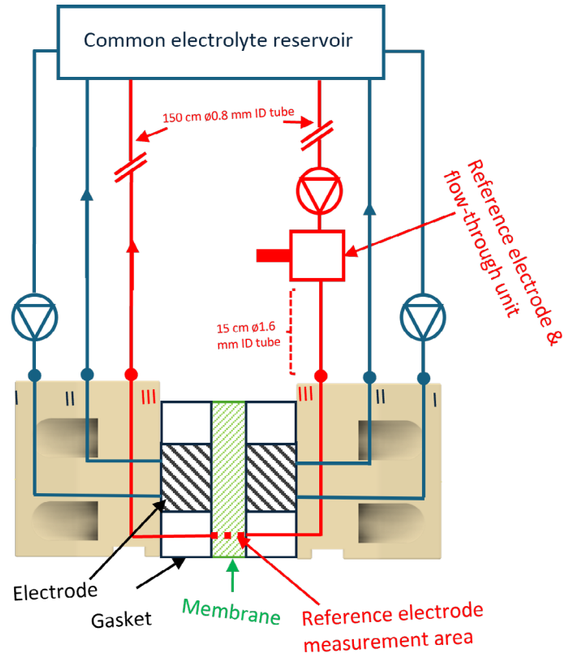



*Figure 2.2 – Hydraulic layout of the experimental setup. The blue circuit represents the main electrolyte flow through the electrochemical cell, while the red circuit represents the reference electrode circuit connected to the Luggin capillaries. Electrolyte is pumped from common reservoir into both circuits using peristaltic pump. Additional pump is used for circulating electrolyte through reference electrode circuit. Here lower ID (ø0.8 mm) and longer tube (150 cm) connected to common reservoir is used to minimise effects of possible shunt currents between common reservoir and reference electrode circuit.*

## Effect of Bubbles on Cell Potential Measurements

Figure 2.3 shows the measured cell potential $U_{cell}$ as a function of time for different temperatures and electrolyte flow rates in the main cell circuit. Unlike conventional polarisation curves where voltage is plotted as a function of current density, the data here are presented as a time series to highlight the influence of bubble formation on the stability of the voltage signal.

At low current densities $U_{cell}$ remains relatively stable with minimal fluctuations. For example, at a flow rate of 10 mL min$^{-1}$ the voltage signal shows almost no measurable noise up to approximately 250 mA (250 mA cm$^{-2}$). In this range the gas production rate is relatively low and bubbles formed at the electrode surface are transported away by the electrolyte flow. As the current increases, the rate of gas evolution also increases and the measured voltage begins to exhibit fluctuations/noise in $U_{cell}$ that becomes pronounced at the highest current densities. However, for the 25 mL min$^{-1}$ flow rates at both 23 °C and 90 °C, the noise is lower. This is also seen from the inset of Fig. 2.3 which shows a zoomed-in plot of the time series data for 1400 mA. The standard deviation of the measured cell voltage, denoted by σ, is used as a quantitative measure of the noise level in the signal. The data demonstrate that the standard deviation decreases with increasing electrolyte flow rate

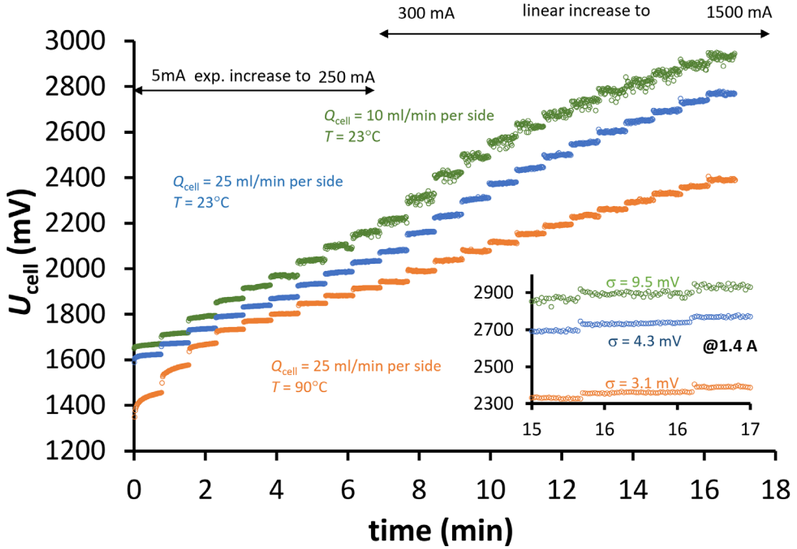



*Figure 2.3 – Measured cell potential $U_{cell}$ as a function of time for different electrolyte flow rates in the main cell circuit during alkaline water electrolysis in 6 M KOH at room temperature and 90°C. Increased electrolyte flow rates reduce fluctuations in the measured cell voltage by improving bubble removal from the electrode surfaces. The inset shows a magnified region at high current where the standard deviation σ of the voltage signal is used to quantify measurement noise.*





through the cell and the temperature of the electrolyte. This trend can be explained by higher electrolyte flow rates removing bubbles more efficiently, thereby reducing their influence on the cell voltage.

## Effect of Bubbles on Reference Electrode / Overpotential Measurements

Figure 2.4 shows the measured overpotentials for hydrogen evolution and oxygen evolution obtained using one common reference electrode. Besides different temperatures and flow rates in the main hydraulic circuit also two different flow rates in the reference electrode circuit were applied, one with no flow (0 mL min$^{-1}$), the other with a flow rate of 1.5 mL min$^{-1}$.

The overpotentials are calculated relative to the thermodynamic potentials of hydrogen and oxygen evolution. Due to the use of one common reference electrode $U_{cell} = U_{rev} + \eta_{H2} + \eta_{O2}$ at all times, where $U_{rev}$ is the minimum thermodynamic potential for water electrolysis and equals 1.23 V at room temperature and 1.17 V at 90 °C. The data are presented as a function of time in order to focus on the fluctuations in the measured potentials. It is emphasized that the purpose of the experiments is solely to investigate how bubbles influence the noise level in reference electrode measurements and not general performance of the electrodes/cell.

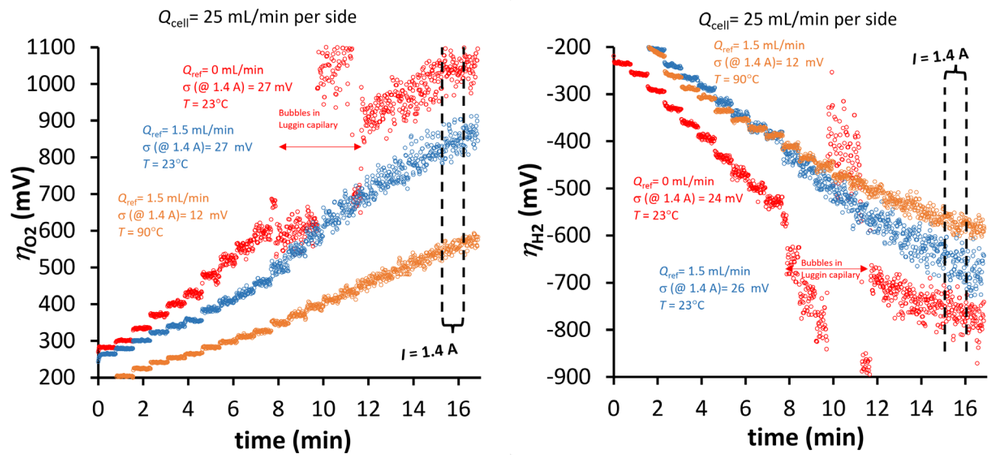



*Figure 2.4 – Measured oxygen and hydrogen overpotentials obtained using a common Hg/HgO reference electrode under different electrolyte flow conditions and temperature. Measurements were performed both with and without electrolyte flow through the reference electrode circuit. Continuous flow through the Luggin capillaries significantly reduces noise in the measured potentials.*

Two clear trends are seen. First, the presence of electrolyte flow in the reference electrode circuit generally reduces the noise in the measured overpotentials. Without flow, the Luggin capillary becomes blocked at around 8 min and accessible again after approximately 12 min. Second, increasing the temperature also reduces the noise in the measured potentials. This can be seen by comparing the plots at 23 °C and 90 °C.

## Stability of reference electrode measurements

The results above show that noise in potential measurements can originate both from bubbles formed at the electrode surfaces and from bubbles entering the Luggin capillary / reference electrode circuit. For long term electrochemical testing stability over longer timescales (minutes to hours) may be important.

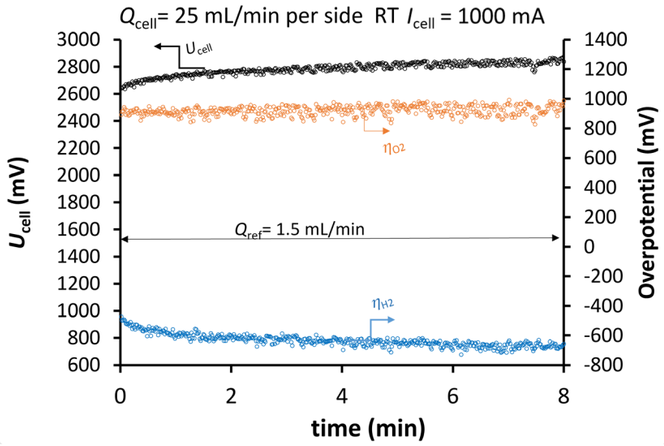



*Figure 2.5 – Cell potential, $U_{cell}$, and overpotentials for hydrogen evolution, $\eta_{H2}$, and oxygen evolution, $\eta_{O2}$, as a function of time at 23 °C and a constant current of 1000 mA (1000 mA cm$^{-2}$). During the whole tests flow is applied through the reference electrode circuit to demonstrate stability.*

An example of this is shown in Fig. 2.5, where the same experimental configuration was operated at 23 °C and a constant current of 1000 mA (1000 mA cm$^{-2}$) and with $Q_{ref}$ = 1.5 mL min$^{-1}$. Besides increasing a little due to conditioning of the electrodes, the measured cell potential, $U_{cell}$, remains relatively stable throughout the experiment. Fig. 2.5 also includes plots of $\eta_{H2}$ and $\eta_{O2}$, here it is seen that $\eta_{O2}$ is fully stable at the same value throughout the experiment, while $\eta_{H2}$ decreases initially and is the main reason for the electrode conditioning/increasing $U_{cell}$ in the experiment. This demonstrates the power of including the Luggin capillary based reference electrodes as it enables increased understanding of the electrode conditioning which in present case can be related to the cathode. Still, the main focus is stability of the measurement, and when comparing (visually) the $\eta_{H2}$ and $\eta_{O2}$ to $U_{cell}$ increased noise levels are seen in the overpotentials compared to cell potential. This increased noise is attributed to bubbles interfering with the measurement. Nonetheless,





noise appears to be random and using data averaging (e.g. 10 data points over 10 s) will significantly reduce this noise.

Together, the results show that bubble formation influences both cell potential and reference electrode measurements. The effect is impossible to predict, but depends on factors such as the cell flow rate, temperature, electrode properties, and gasket geometry. In general, higher cell flow rates and higher temperatures reduce the likelihood of persistent blockage because bubble transport is improved. For long-term measurements with reference electrodes flow in the reference electrode circuit ensures stability.

## Performance tests

The preceding sections have primarily focused on the limitations that bubbles impose on reference electrode measurements in the 1 cm² M-cell. The present section instead illustrates the electrochemical performance that can be obtained with the setup. Using the experimental configuration shown in Fig. 2.2, polarisation curves together with hydrogen and oxygen overpotentials were measured by recording the potentials as a function of time at a series of applied currents. Each current step was held for 45 s, and the reported values were constructed as the average of the final 22 s of each step. The present data compare operation at room temperature (RT, 23 °C) and 90 °C, and the results are shown in Fig. 2.6.

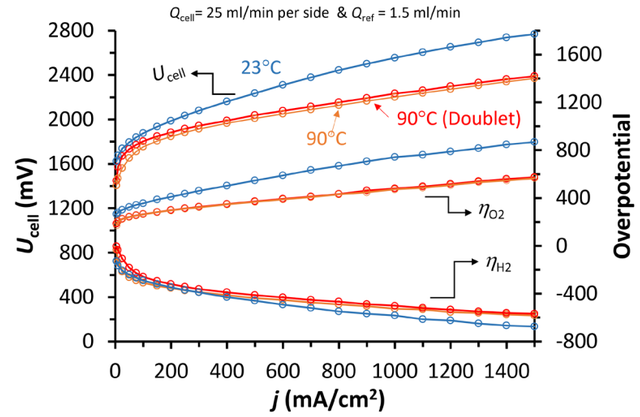



*Figure 2.6 – Polarization curve and corresponding hydrogen and oxygen overpotentials measured using the setup shown in Fig. 2.2. Each data point is constructed from the average of the final 22 s of a 45 s current step. Measurements were performed in 6 M KOH at 23 °C and 90 °C. The comparison demonstrates the performance capability of the 1 cm² M-cell and shows the reduction in total cell potential and especially hydrogen overpotential at elevated temperatures.*

Overall, the polarisation curves at room temperature and 90 °C show similar shapes, but the total cell potential at 90 °C is approximately 400 mV lower at the highest currents (1500 mA cm$^{-2}$), as expected from the improved electrochemical kinetics and electrolyte transport at elevated temperature. When the overpotentials are separated into contribu-

tions from the hydrogen evolution reaction and the oxygen evolution reaction, it becomes clear that the main improvement comes from the oxygen side. The hydrogen overpotential remains relatively similar at room temperature and 90 °C, whereas the oxygen overpotential decreases by approximately 300 mV at 1500 mA $cm^{-2}$ upon heating. This appears somewhat contradictory to the similar plots shown in Fig. 1.8 where it was seen that $U_{cell}$ decreased less and the improvement was mainly on the hydrogen side as the temperature increases. However, for alkaline water electrolysis it is known that impurities in the electrolyte and previous operation of the electrodes have a large influence on the performance/polarisation curve. As the present tests focus on demonstrating the capabilities of the M-cell, the age of the electrolyte, reuse of electrodes, etc. were not controlled, and it is anticipated that the apparently contradictory results arise from non-systematic reuse of electrodes and electrolytes.

## Heating of multiport reservoir and cell

Heating and accurate temperature control are often overlooked or poorly integrated in commercial and state-of-the-art electrochemical test systems. In contrast, the Redox-Flow.com multiport reservoir is designed with integrated heating possibilities and can be placed directly on standard laboratory hotplates equipped with an external thermometer and temperature controller. Additionally, the 1 $cm^2$ M-cell has ports that enable placement of thermometers on the current collector inside the cell in order to measure and control the temperature accurately.

To demonstrate the temperature control capabilities a test with 200 mL pure water was made with a constant flow rate of 40 mL $min^{-1}$ on each side. Here the temperature of the liquid in the reservoir was controlled. Temperature control was achieved using a 600 W plate heater with an external thermometer / temperature controller in the multiport reservoir. The temperature evolution during heating to the 80 °C setpoint is shown in Fig. 2.7. One thermometer was placed in the 316L heating block, which is in direct contact with the heater plate. A second thermometer was placed directly in the water and used as the controlling thermometer. A third thermometer measured the ambient temperature outside the reservoir. Finally also a thermometer was mounted inside the M-cell on the back side of one of the current collectors. Additionally, the M-cell was placed in a thermally isolating environment (PU foam) to minimise thermal gradients in the cell and ensure accurate measurement of the temperature inside the cell. As expected, the temperature in the heating block rises first, followed by the electrolyte temperature. Target temperature of 80°C of the water in the multiport reservoir is reached rapidly within 25 min. More importantly it is seen that the temperature of the cell follows that of the water in the reservoir closely and is about 9°C lower than in the reservoir once the water temperature is reached/steady state.

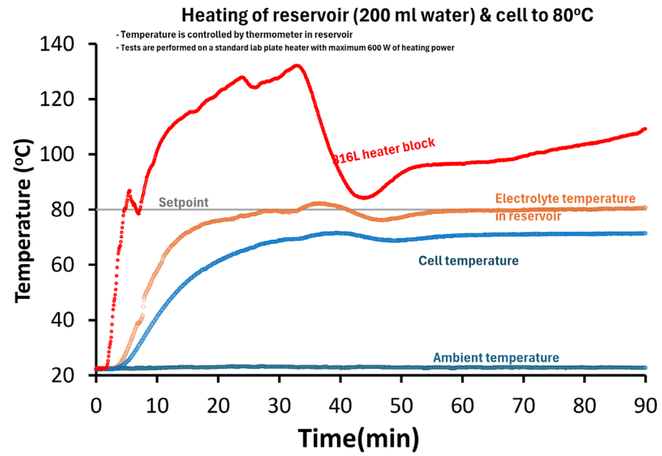



*Figure 2.7 – Temperature profiles measured during heating of the multiport reservoir system to 80 °C using a 600 W laboratory plate heater with external temperature control. The curves show the temperature of the water (200 mL) in the multiport reservoir, the temperature inside the cell, the 316L heating block in contact with the hotplate, the setpoint, and the ambient temperature.*

The temperature difference between the water inside the reservoir and the cell is mainly due to heat losses through the tubes from the reservoir to the cell including peristaltic tubes. In the present case each of the tubes is about 1 m long and made from PTFE with an inner diameter of 1.6 mm (1/16”) and outer diameter of 3.2 mm (1/8”). Making an accurate model for the temperature profile in the tubes as it approaches the cell is very difficult as it involves both PTFE/peristaltic tubes, diffusive and radiative heat losses and assumptions about the convective heat transfer around the tubes. Nonetheless, a simple model considering PTFE tubes only, at a flow rate of 40 mL $min^{-1}$, shows that temperature differences in the range 5 °C to 9 °C can be expected. The lower temperature difference (5°C) is with low convection around the tubes and the higher temperature difference (9°C) is with moderate/higher convection. In both cases the radiative heat loss accounts for less than 1°C, showing that the main heat loss is through diffusive heat transfer. In any case the modelling results in temperature differences that are in the same range as the observed one.

Thus two main conclusions can be drawn from this:

1. If accurate temperature control is needed, the temperature controlling thermometer should be located inside the cell
2. If temperature control is done on the reservoir, the temperature difference between that of the cell and the reservoir will depend on the flow rate and tube length, where higher flow rate and lower tube length will result in lower temperature difference and better temperature control

## Part 3 – Closed cell configuration with two independent reference electrodes

All experiments were performed using commercially available electrochemical research equipment from www.redox-flow.com. The electrochemical cell used in this study was the 1 cm² M-cell, a multipurpose electrochemical test cell designed for advanced electrochemical investigations and flexible reference electrode configurations (Fig. 3.1). The cell includes integrated ports for electrolyte flow and for Luggin capillary reference electrode measurements. The reference electrodes (Hg/HgO) were connected through a flow-through reference electrode unit positioned outside the cell and connected to the cell via Luggin capillaries.

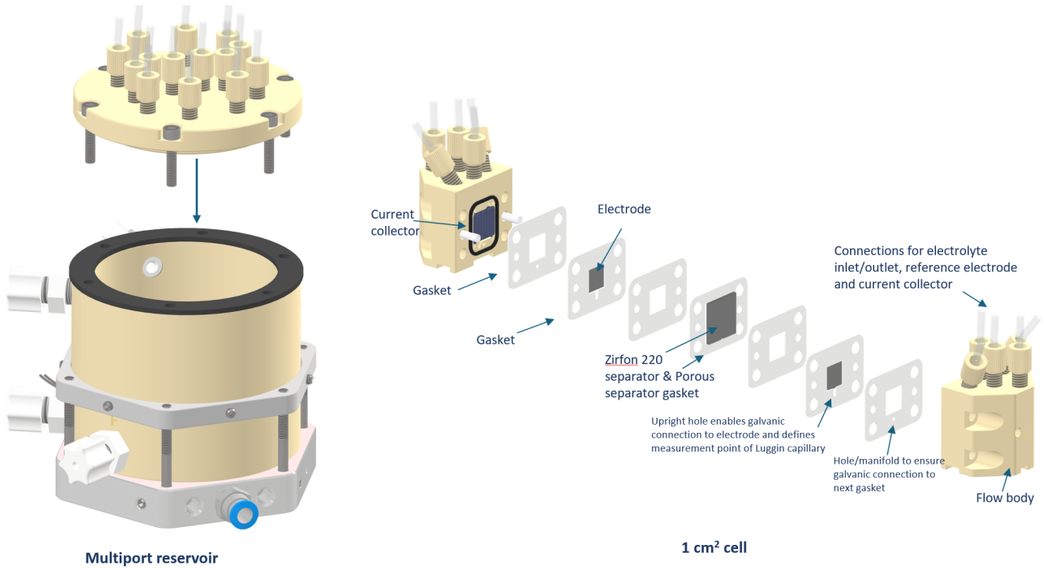



*Figure 3.1 – Configuration of the 1 cm² M-cell operated in a closed cell configuration with two independent reference electrodes. The cell is connected to a multiport electrolyte reservoir containing 6 M KOH while electrolyte is circulated through the cell via external tubing connections.*

The experimental setup consisted of a 6 V / 5 A power supply equipped with an AUX measurement unit that records potentials from reference electrodes and temperature sensors. All voltage and current data were recorded with a resolution of 1 s. Nickel electrodes with a porosity of 150 ppi and a thickness of 1.7 mm were used as both anode and cathode. The M-cell was operated in a closed cell configuration and connected to a multiport electrolyte reservoir containing the 6 M KOH electrolyte solution (see M-cell assembly manual for more details – https://redox-flow.com/product/m-cell-full-cell-2/ ). Electrolyte was continuously circulated through the cell using a peristaltic pump. An additional peristaltic pump was used to circulate electrolyte through the reference electrode circuit connected to the Luggin capillaries. The hydraulic layout of the system is illustrated in Fig. 3.2. In this figure the blue circuit represents the main electrolyte flow through the electrochemical cell, while the red circuit represents the reference electrode circuit connected to the Luggin capillaries.

Electrolyte in both circuits was pumped from the reservoir into the cell to minimise the influence of gas bubbles formed during electrolysis.

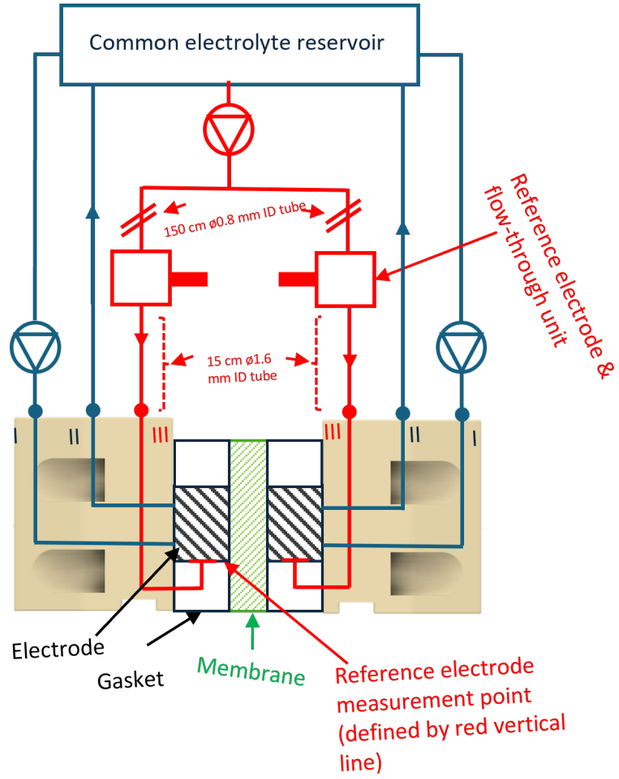



*Figure 3.2 - Hydraulic layout of the experimental setup. The blue lines represents the main electrolyte flow through the electrochemical cell, while the red lines represents the reference electrode circuit connected to the Luggin capillaries. Electrolyte is pumped from common reservoir into both circuits using a peristaltic pump. An Additional pump is used for circulating electrolyte through both reference electrode circuits. Here lower ID (ø0.8 mm) and longer tube (150 cm) connected to common reservoir is used to minimise effects of possible shunt currents between common reservoir and reference electrode circuit.*

## Effect of Bubbles on Cell Potential Measurements

Figure 3.3 shows the measured cell potential $U_{\text{cell}}$ as a function of time for different temperatures and electrolyte flow rates in the main cell circuit ($Q_{\text{cell}}$) and reference electrode circuit ($Q_{\text{ref}}$). Unlike conventional polarisation curves where voltage is plotted as a function

of current density, the data here are presented as a time series to highlight the influence of bubble formation on the stability of the voltage signal.

For all flow rates $U_{cell}$ remains relatively stable with minimal fluctuations. For example, at a flow rate of 10 mL min$^{-1}$ the voltage signal shows almost no measurable noise up to approximately 250 mA (250 mA cm$^{-2}$). As the current increases there is a small tendency for the noise to increase a little. Nonetheless, the inset of Fig. 3.3 shows a zoomed-in plot

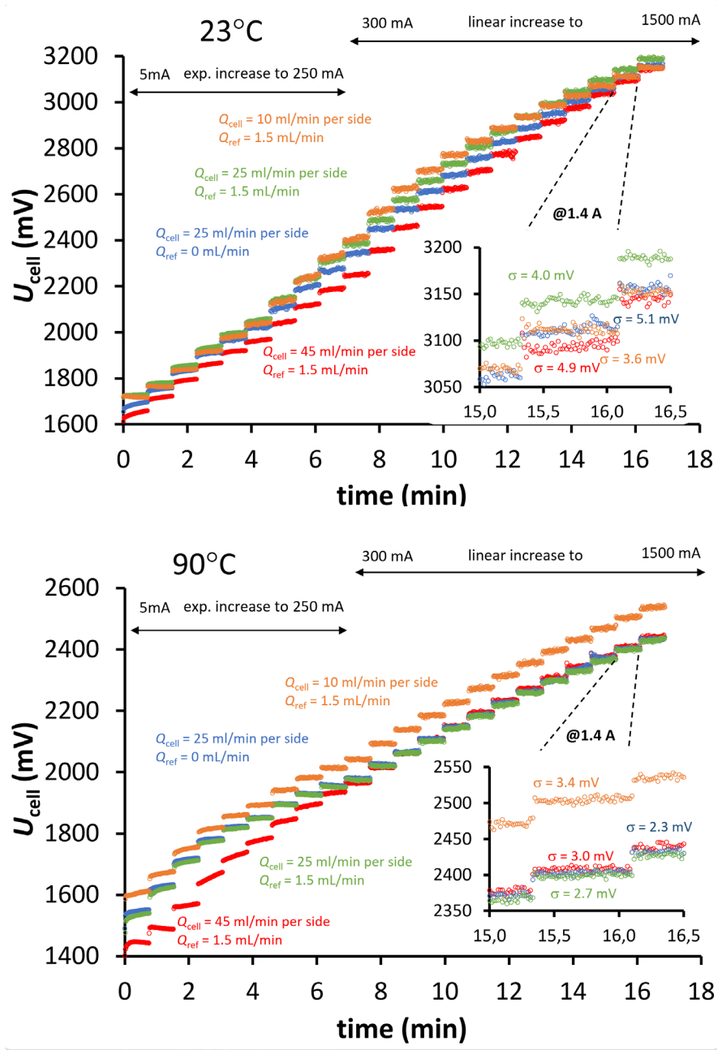



*Figure 3.3 – Measured cell potential $U_{cell}$ as a function of time for different electrolyte flow rates in the main cell circuit during alkaline water electrolysis in 6 M KOH at room temperature and 90°C. The inset shows a magnified region at high current where the standard deviation σof the voltage signal is used to quantify measurement noise.*





of the time series data for 1400 mA. The standard deviation of the measured cell voltage, denoted by σ, is used as a quantitative measure of the noise level in the signal. The data demonstrate that at both 23 °C and 90 °C the variation/noise level is very low and shows no systematic dependence on the flow rate. Still it appears as if the noise level is slightly but systematically lower for the 90 °C tests compared to the 23 °C tests.

## Effect of Bubbles on Reference Electrode / Overpotential Measurements

Figure 3.4 shows the measured overpotentials for hydrogen evolution and oxygen evolution obtained using two separate reference electrodes as outlined in Fig. 3.2. In addition to different temperatures and flow rates in the main hydraulic circuit, two different flow

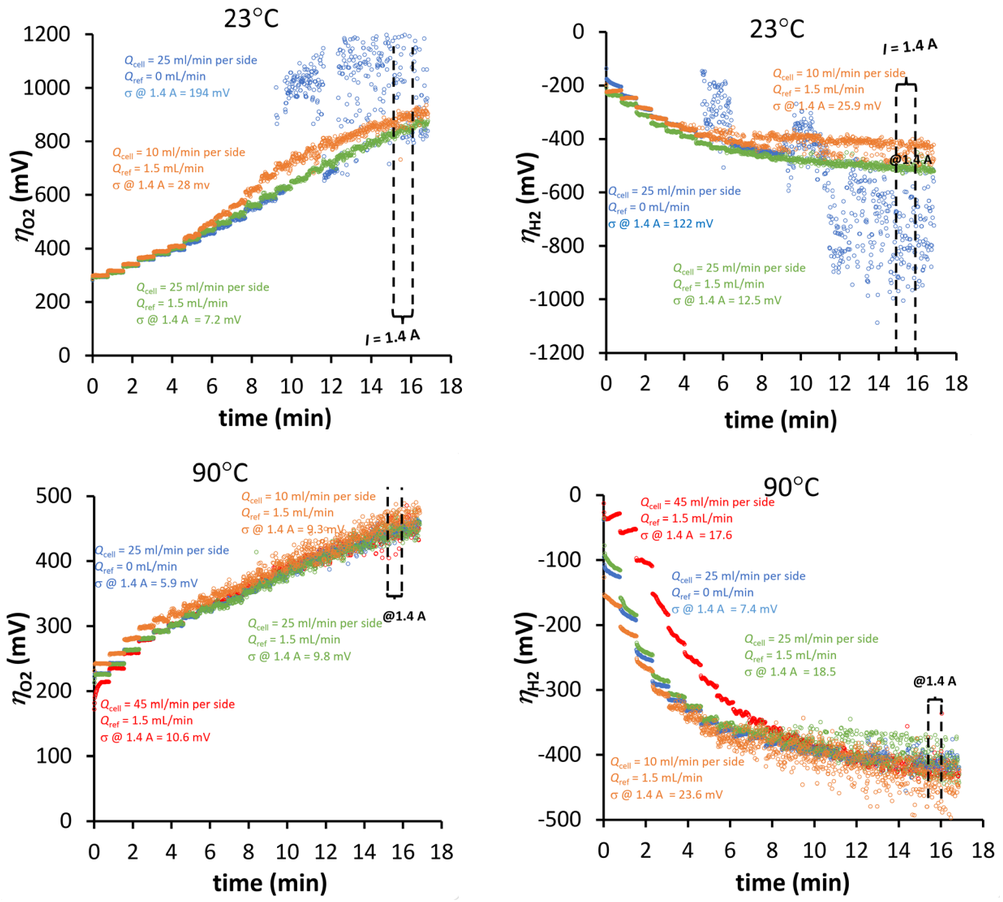



*Figure 3.4 – Measured oxygen and hydrogen overpotentials obtained using two separate Hg/HgO reference electrode under different electrolyte flow conditions and temperatures. Measurements were performed both with and without electrolyte flow through the reference electrode circuit.*

rates in the reference electrode circuit were applied, one with no flow (0 mL $min^{-1}$), the other with a flow rate of 1.5 mL $min^{-1}$.

The overpotentials are calculated relative to the thermodynamic potentials of hydrogen and oxygen evolution. As two separate reference electrodes are used, the relation $U_{cell} = U_{rev} + \eta_{H2} + \eta_{O2}$ no longer applies, as it does when one common reference electrode is used. Here Urev is the minimum thermodynamic potential for water electrolysis and equals 1.23 V at room temperature and 1.17 V at 90 °C. The data are presented as a function of time in order to focus on the fluctuations in the measured potentials. It is emphasized that the purpose of the experiments is solely to investigate how bubbles influence the noise level in reference electrode measurements and not general performance of the electrodes/cell. It is clearly seen that the presence of electrolyte flow in the reference electrode circuit generally leads to stable measurements. Without flow, the Luggin capillaries become blocked intermittently on the two sides and disturb the measurements, whereas flow in the reference electrode circuit stabilises them.

## Performance tests

The preceding sections have primarily focused on the limitations of the 1 $cm^2$ M-cell in terms of the effects of bubbles on reference electrode measurements. The present section instead illustrates the electrochemical performance that can be obtained with the setup.

Using the experimental configuration shown in Fig. 3.2, polarisation curves together with hydrogen and oxygen overpotentials were measured by recording the potentials as a function of time at a series of applied currents. Each current step was held for 45 s, and the reported values were calculated as the average of the final 22 s of each step. The present data compare operation at room temperature (RT, 23 °C) and 90 °C, and the results are shown in Fig. 3.5.

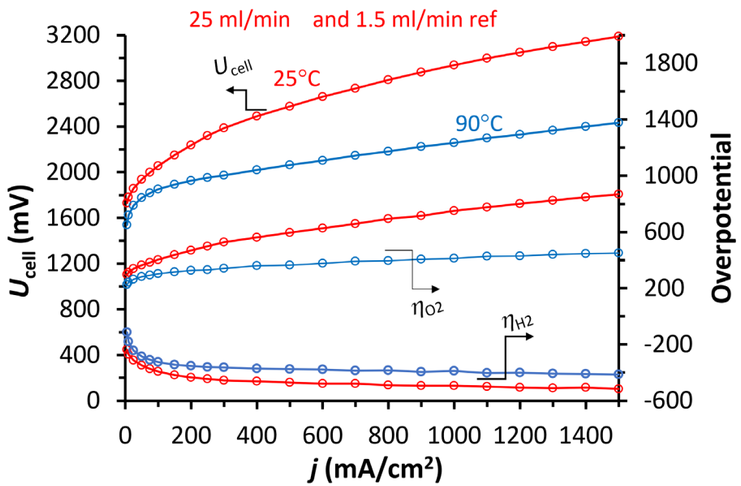



*Figure 3.5 – Polarization curve and corresponding hydrogen and oxygen overpotentials measured using the setup shown in Fig. 3.2. Each data point is constructed from the average of the final 15s of a 30s current step. Measurements were performed in 6 M KOH at 23 °C and 90 °C.*





Overall, the polarisation curves at room temperature and 90 °C show similar shapes, but the total cell potential at 90 °C is approximately 700 mV lower than the RT data at the highest currents (1500 mA $cm^{-2}$), as expected from the improved electrochemical kinetics and electrolyte transport at elevated temperature. When the overpotentials are separated into contributions from the hydrogen evolution reaction and the oxygen evolution reaction, it becomes clear that the main improvement comes from the oxygen side. The hydrogen overpotential remains relatively similar at room temperature and 90 °C, whereas the oxygen overpotential decreases by approximately 300 mV at 1500 mA $cm^{-2}$ upon heating. This appears somewhat contradictory to the similar plots shown in Fig. 2.6 where it was seen that $U_{cell}$ at RT are not the same, while data at 90 °C are about the same. However, for alkaline water electrolysis it is known that impurities in the electrolyte and previous operation of the electrodes have a large influence on the performance/polarisation curve.

As the present tests focus on demonstrating the capabilities of the M-cell, the age of the electrolyte, reuse of electrodes, etc. were not controlled, and it is anticipated that the apparently contradictory results arise from non-systematic reuse of electrodes and electrolytes. Additionally, $\eta_{H2}$ and $\eta_{O2}$ cannot be directly compared because the use of two independent reference electrodes in tests of Fig. 3.5 ($U_{cell} \neq U_{rev} + \eta_{H2} + \eta_{O2}$) compared to tests of Fig. 2.6 ($U_{cell} = U_{rev} + \eta_{H2} + \eta_{O2}$).

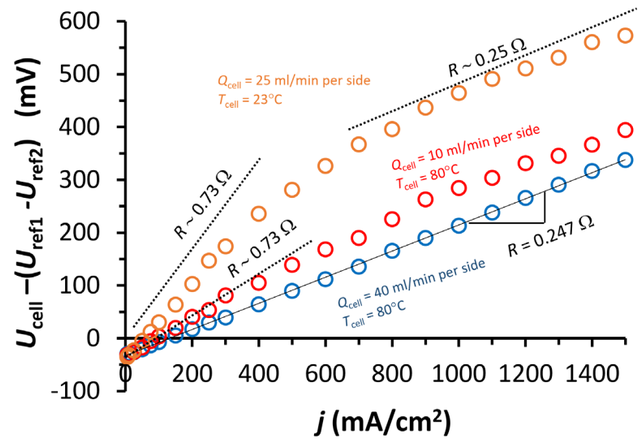



*Figure 3.6 – Measured voltage difference between the cell voltage ($U_{cell}$) and the difference between the two reference electrodes ( $U_{ref1} - U_{ref2}$ ). The magnitude is a proxy for the sum of the resistance of the separator and current density variable contributions from the electrolyte and bubbles.*

## Internal consistency of reference electrode measurement points

This section is related to discussing the accuracy and positional consistency of the measurement points defined by the Luggin capillaries. Two reference electrodes are connected to individual Luggin capillaries with measurement points located at the middle of the electrodes (perpendicular to the 1.7 mm thick electrode) as defined by the geometries of the gaskets as shown in Fig. 3.1 and 3.2. This means that the reference electrodes are separated by the Zirfon 220 separator and a reference electrode distance (~1.0 mm including the Zirfon thickness). For that reason $U_{cell} - (U_{ref1} - U_{ref2}) = U_{cell} - (\eta_{O2} - \eta_{H2} + U_{rev})$ will measure the sum of the resistance of the separator and the resistance of the electrolyte inside the tortious electrode plus any additional bubble resistance.

Figure 3.6 shows $U_{cell} - (U_{ref1} - U_{ref2})$ as a function of current density for tests with different cell flow rates and temperatures. For Zirfon UTP220 separator the expected resistances are approximately 0.1Ω (0.1Ω cm$^2$) and 0.05 Ω (0.05 Ω cm$^2$) at RT and 80°C[1].While resistance from 1 mm electrolyte inside the electrode (not considering tortuosity) is 0.17 Ω and 0.073 Ω at RT and 80°C. Thus the expected minimum resistance measured is expected to be 0.27 Ω and 0.123 Ω at RT and 80°C, respectively.

For the test with temperature of 80°C and highest flowrate (40 mL min$^{-1}$), it is seen that that the curve has a small offset of about -30 mV, which is due to the small differences of the reference electrodes that were not calibrated prior to the experiment. Besides this the curve is almost fully linear with a slope of 0.247 Ω which is slightly higher than the minimum calculated value of 0.123 Ω. The difference probably being due to both a combination of bubble resistance and electrode/electrolyte tortuosity. When flow rate is lower at 10 mL min$^{-1}$ (but at same temperature) it is seen that the curve becomes a little non-linear with an initial resistance of about 0.37 Ω that is higher than 0.247 Ω and in agreement with higher bubble resistance due to lower flow rate. For the RT experiment where the flow rate is 25 mL min$^{-1}$, a clear non-linear trend is seen, with and initial resistance of 0.73 Ω that flattens out to a value of about 0.25 Ω. Again the value of 0.73 Ω is much higher than the minimum expected value of 0.27 Ω from separator electrolyte and is probably a combination of both increased bubble resistance and tortuosity of the electrode. The origin of the non-linear increase is not fully clear, but most likely related to some dynamic bubble resistance. I.e. as the bubble formation increases the bubbles takes out such a large volume that resistance cannot increase any further.  Nonetheless, the main point here is to demonstrate that the position of Luggin capillaries are well defined down to sub millimetre and depending on the gasket configuration can be used for studying either separator resistance or bubble dynamics.

1 Technical Data Sheet ZIRFON UTP 220





## Demonstration of an application test

Addition of iron or presence of iron from e.g. 316L stainless steel in the KOH electrolyte is well-known to increase the performance/efficiency of alkaline electrolysers[2]. The following demonstrates how the 1 cm² M-cell with reference electrodes can be used for understanding the effect of iron on the performance in more detail. The experimental setup is the same as the one described in Figure 3.1 and 3.2 with two independent reference electrodes, however, the setup described in Figure 1.1 and 1.2, and Figure 2.1 and 2.2 could equally well be used.

Figure 3.7 shows the cell potential, $U_{cell} - (\eta_{O2} - \eta_{H2} + U_{rev})$, $\eta_{O2}$ and $\eta_{H2}$ as function of time with cell flow rates of 10 mL min$^{-1}$ and 1.5 mL min$^{-1}$ through the reference electrode circuit. Temperature inside the cell is 80 °C. Initially there is no current/voltage applied to the cell, but within the first minute the 1000 mA is applied and $U_{cell}$ increases to an almost constant value within the first 5 minutes of the test. Equally, $\eta_{H2}$ and $\eta_{O2}$ reach their steady-state values within the first 5 min, but with $\eta_{H2}$ reacting slower. After about 18 min $Fe_2(SO_4)_3$ is added to the common electrolyte in an amount corresponding to 1 mM. $U_{cell}$ drops instantaneously and reaches an almost steady-state value after about 6 minutes, and about 300mV lower than before addition of iron and demonstrates the effect of iron addition.

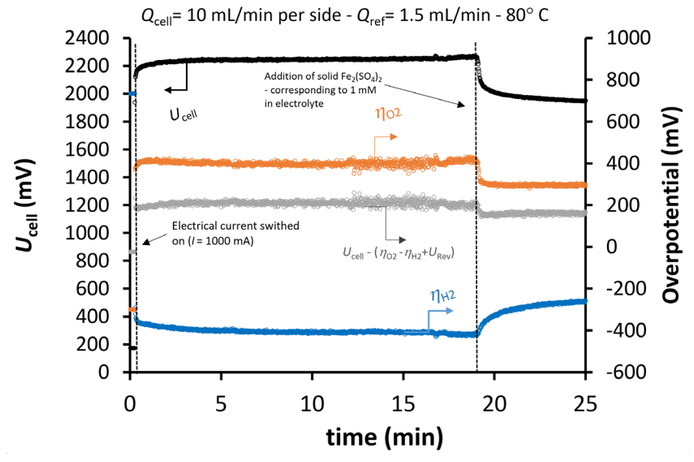



*Figure 3.7 – Cell potential, $U_{cell}$, and overpotentials for hydrogen evolution, $\eta_{H2}$, and oxygen evolution, $\eta_{O2}$, as a function of time at 90°C and a constant current of 1000 mA (1000 mA cm$^{-2}$). Current is switched on within the first minute of the experiment. After about 19 min $Fe_2(SO_4)_3$ is added to the common 6 M KOH electrolyte, corresponding to a 1 mM concentration.*

2 Demnitz, M., Lamas, Y. M., Barros, R. L. G., den Bouter, A. D. L., van der Schaaf, J., & de Groot, M. T. (2024). Effect of iron addition to the electrolyte on alkaline water electrolysis performance. Iscience, 27(1).

More importantly, it is seen that $\eta_{O2}$ drops almost to the steady state value within 30–45 seconds and is almost 200 mV lower than before. Nonetheless, $\eta_{H2}$ also becomes less negative (about 100 mV) but the steady state value is first reached after several minutes and demonstrates that the surface/catalysts restructuring on the hydrogen side is much slower than on the oxygen side.
Besides this also the $U_{cell} - (\eta_{O2} - \eta_{H2} + U_{rev})$ is plotted. As discussed in previous section it is a measure of the combined separator resistance and electrolyte resistance a certain distance (~ 0.5 mm on each side) into the electrode. Initially the value is constant and about 200 mV, once the iron is added there is a small drop of about 50 mV. As the separator resistance is not expected to change, it can be interpreted as that the improved catalytic performance moves the electrochemical reactions (OER, HER) closer towards the separator. As the reactions move closer the ohmic loss due to migration of ions will become smaller and explain the small drop in the value.

Together, this application test demonstrates the power of the M-cell, its Luggin capillaries and use of reference electrodes to increase understanding of

1. Individual catalytic improvement of both $\eta_{O2}$ and $\eta_{H2}$ when iron is added
2. The dynamics of the surface/catalysts restructuring when iron is added and in particular the difference between the two sides
3. Understanding of the effect of the catalysts and impact on the reaction (HER/OER) sites on the performance

How that noise in potential measurements can originate both from bubbles formed at the electrode surfaces and from bubbles entering the Luggin capillary / reference electrode circuit. For some long term electrochemical testing stability over longer timescales (minutes to hours) is important.

## References

[1] A Review of Specific Conductivities of Potassium Hydroxide Solutions for Various Concentrations and Temperatures
R.J. Gilliam, J.W. Graydon, D.W. Kirk, S.J. Thorpe, International Journal of Hydrogen Energy, 32 (2007) 359–364

[2] Technical Data Sheet ZIRFON UTP 220

[3] Demnitz, M., Lamas, Y. M., Barros, R. L. G., den Bouter, A. D. L., van der Schaaf, J., & de Groot, M. T. (2024). Effect of iron addition to the electrolyte on alkaline water electrolysis performance. Iscience, 27(1).

WHITEPAPER VII

# 1 cm² M-Cell: Flow Battery Tests

## Introduction

Flow battery research and development is largely driven by optimisation of electrodes, electrolytes and flow-cell geometry. In particular for testing of new redox active molecules, only small amounts/volumes are available and for this reason smaller active area are needed. Here the 1 cm² M-cell (https://redox-flow.com/product/m-cell-full-cell-2/), is a unique multipurpose electrochemical test cell for advanced electrochemical investigations. Additionally, in a standard laboratory flow-battery setup, only the electrical current and the cell potential are measured. Although these two parameters alone determine the overall performance, it is from an R&D perspective desirable to understand how the individual parts and components contribute to the overall energy losses (anolyte/catholyte redox potentials and overpotentials). This white paper demonstrates how these losses can be mapped out experimentally. The demonstration focuses on battery testing but the M-cell can, however, equally be used for many other purposes, such as half-cell cycling, cyclic voltammetry and studies on low electrolyte volumes. The tests are performed with 2,7-anthraquinone disulfonate (AQDS) and ferrocyanide ($[Fe(CN)_6]^{4-}$) as the redox-active molecules. The motivation of this white paper is not so much to demonstrate optimal performance of the chosen chemistry, but rather to demonstrate the capabilities and possibilities of the combined M-cell and OCV-cell setup, which is unique in enabling studies on small electrolyte volumes with full mapping of all relevant potentials.

## Definitions of energy levels

Fig. 1 shows a general representation of the energy levels in a flow battery (or any other reversible electrochemical flow system). In the figure, the blue scale represents absolute energy levels with respect to, e.g., the standard hydrogen electrode (SHE). On the absolute scale, the abbreviations are:

- $\varepsilon_{CC-}$ and $\varepsilon_{CC+}$: The potential on the negative and positive side current collectors
- $\varepsilon_{-}$ and $\varepsilon_{+}$: The (redox) potential of the liquid on the negative and positive side – note that it is variable and depends on the state-of-charge and is described by the Nernst equation
- $\varepsilon_{ref}$: The potential of (a) reference electrode(s) in the setup

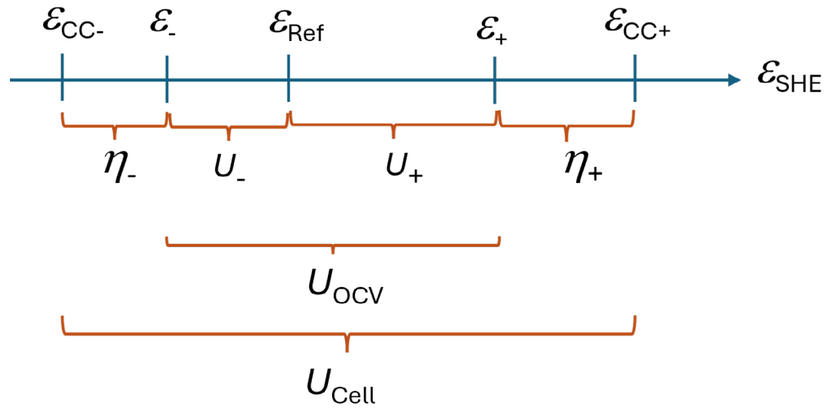



*Figure 1 – Energy levels in flow batteries*

While the upper (blue) potentials are absolute energy levels, the lower (orange) parts show the measurable voltages. Here

- $\eta_{-}$ and $\eta_{+}$: The overpotentials for charging (discharging) of the negative and positive side liquids
- $U_{-}$ and $U_{+}$: Measured potentials with respect to a reference electrode to determine the liquid (redox) potentials of the negative ($\varepsilon$) and positive side ($\varepsilon_{+}$)
- $U_{OCV}$: Potential measured in an OCV cell
- $U_{cell}$: The potential measured on the electrochemical cell by battery tester or potentiostat

The overpotentials and the electrolyte redox potentials are the most important parameters for mapping out internal resistive losses. There are multiple experimental approaches [1][2][3] for a complete mapping of $\eta_{-}$, $\eta_{+}$, $\varepsilon_{-}$ and $\varepsilon_{+}$.

## Experimental setup

All experiments were performed using commercially available electrochemical research equipment from www.redox-flow.com. The electrochemical cell used in this study was the 1 cm² M-cell, a multipurpose electrochemical test cell designed for advanced electrochemical investigations and flexible reference electrode configurations (Fig. 2):

1 Measurement of Overpotentials and Liquid Potentials in Flow Batteries, www.redox-flow.com.

2 Gonzalez, G., & Peljo, P. (2025). Experimental Set-Up for Measurement of Half-Cell-and Over-Potentials of Flow Batteries During Operation. Batteries & Supercaps, 8(2), e202400394.

3 Langner, J., Melke, J., Ehrenberg, H., & Roth, C. (2014). Determination of overpotentials in all vanadium redox flow batteries. ECS Transactions, 58(37), 1.

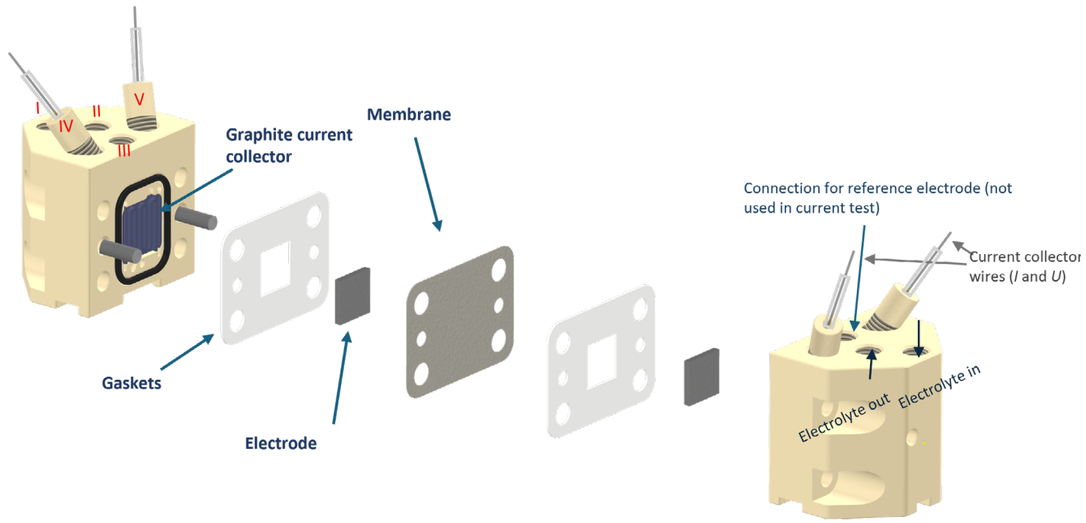



*Figure 2 – General configuration of the 1 cm² M-cell operated in closed cell configuration as shown in figure. Several gaskets are stacked to obtain a compressed electrode thickness of 3.3 mm.*

- Membrane: 20 µm E620 membrane from Fumatech
- Electrodes: Thermally treated AvCarb carbon felt, 4.7 mm thickness at 30% compression (3.3 mm compressed thickness)
- Current collectors: Graphite based (standard for flow batteries)
- Flow rate: 20 mL/min per side

Additionally, Redox-Flow has developed a unique OCV cell (see the separate white paper *Measurement of Overpotentials and Liquid Potentials in Flow Batteries* for a detailed performance evaluation) that enables an additional chamber to be mounted on the OCV cell. This additional chamber can be used as an 'internal' reference electrode in the OCV cell, replacing the external reference electrodes used in conventional setups.

Fig. 3 shows a schematic representation of the setup. Red and blue lines refer to the electric and hydraulic circuits, respectively, while the black parts represent the units in the circuit. The overpotentials ($\eta_-$ and $\eta_+$) are measured directly between the OCV cell and the electrochemical flow cell, while the redox potentials ($\varepsilon_-$ and $\varepsilon_+$) are measured with respect to the redox solution in the central chamber through the voltages $U_-$ and $U_+$. In the present white paper, the reference solution is a 50%/50% mixture of ferro-/ferricyanide (Zobell's solution). Since the posolyte is ferrocyanide ($[Fe(CN)_6]^{4-}$), the reference chamber is placed





on the outside of the positive side of the OCV cell (rather than in the centre, which can also be used) to minimise cross-over of contaminants into the reference solution. Throughout this white paper, all potentials are given with reference to the ferri-/ferrocyanide potential, and for this reason $\varepsilon_- = U_-$ and $\varepsilon_+ = U_+$. The different chambers of the OCV cell are likewise separated by Fumatech E620 membranes.

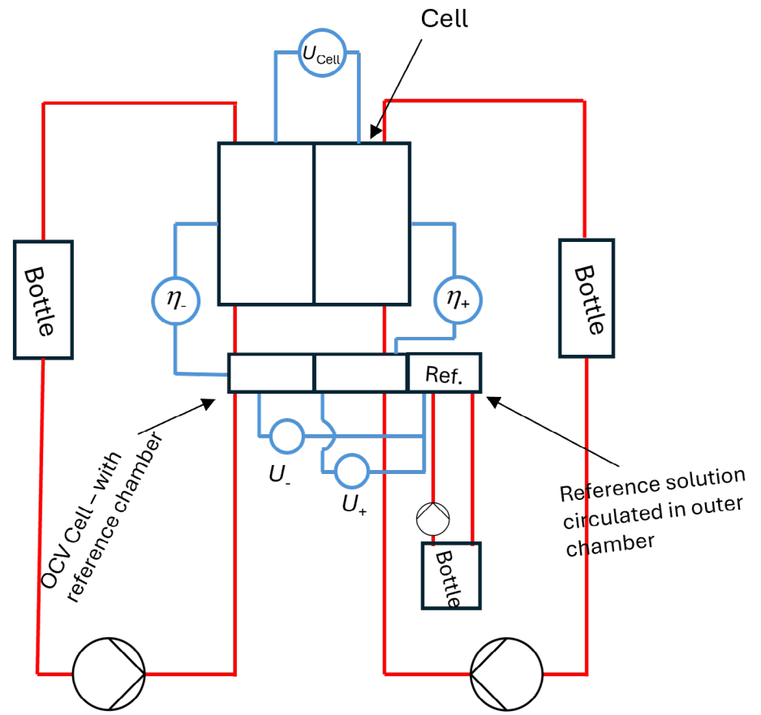



*Figure 3 – Schematic representation of a setup with an OCV cell with internal reference.*

The reference solution is circulated from an external third reservoir bottle by a peristaltic pump. It is noted that the same peristaltic pump (with three pump heads) is used for both the main cell and the reference chamber of the OCV cell, and that all channels are pumped at 20 mL/min.

In the present test, the electrolyte compositions were:

- Negolyte (120 mAh for 1.5 electron transfer[1]): 30 mL – 0.1 M $Na_2AQDS$ (2,7-anthraquinone disulfonate) + 0.25 M $Na_2SO_4$
- Posolyte (402 mAh): 50 mL – 0.3 M $K_4[Fe(CN)_6]$ + 0.25 M $Na_2SO_4$
- Reference solution: 40 mL – 0.15 M $K_4[Fe(CN)_6]$ + 0.15 M $K_3[Fe(CN)_6]$ + 0.20 M $Na_2SO_4$

The posolyte capacity (402 mAh) is thus in clear excess of the negolyte capacity (120 mAh), ensuring that the posolyte is not the capacity-limiting side. Hence, it is the AQDS

negolyte that is being probed in terms of capacity fade.
Additionally, the test setup comprised a 6 V/5 A battery tester equipped with an auxiliary (AUX) measurement unit that records the potentials from the OCV cell (overpotentials and redox potentials). All voltage and current data were recorded with a time resolution of 5 s for the battery cycling and 1s for the polarisation curves.

## Polarisation curve

The polarisation curve was obtained after the battery had been cycled for several days and was recorded at 50% state-of-charge (SOC). It was obtained by applying a constant current and measuring the voltage for 10 s, using the average of the last 3s as the voltage value in the polarisation curve. Currents were scanned from negative to positive values.

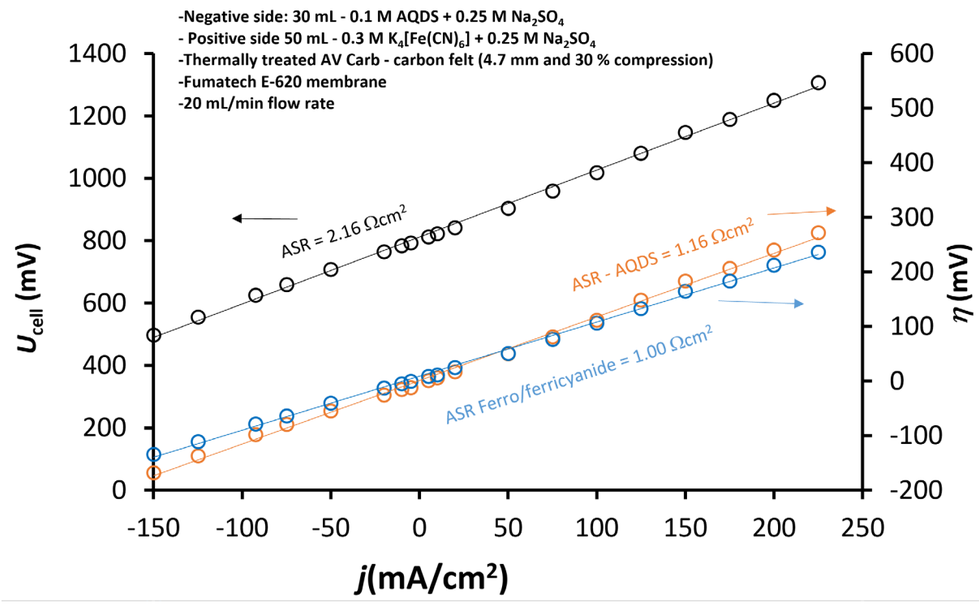



*Figure 4 – Polarisation curve and overpotentials for both negative and positive side. Positive current is charging and negative current is discharging*

Fig. 4 shows the polarisation curve at 50% SOC, from which a total area-specific resistance (ASR) of 2.16 Ω cm² is found, in agreement with previously reported[1] values of 1.8 Ω cm² to 2.2 Ω cm² for a similar chemistry and electrode configuration but measured on a 25cm² cell. By combining the M-cell with the OCV cell, it is also possible to measure the individual overpotentials, which are likewise shown in Fig. 4, where the ASR related to the

1 Fenini, F. Et al Impact of pH management on utilization and performance of anthraquinone/ferrocyanide flow batteries, Journal of Power Sources 540 (2022): 231641.





positive side is 1.00 Ω cm² and the ASR related to the negative side is 1.16 Ω cm². The sum of the two ASRs adds up to the total ASR (2.16 Ω cm²) within 0.01 Ω cm², despite the values being obtained from three independent voltage measurements. This not only underlines the robustness of the method, but also demonstrates that the combination of the M-cell and the OCV cell constitutes a powerful setup for the measurement and deconvolution of the individual overpotentials.

## Battery cycling

To further demonstrate some of the potential R&D applications, a battery cycling test was conducted on the setup with the OCV cell with internal reference. The cycling protocol consisted of constant-current charging/discharging at 80 mA to voltage limits of 1150 mV and 475 mV, respectively, followed by constant-voltage charging/discharging until the current had decreased to 10 mA.

Fig. 5 shows representative time-series data of all measured parameters between cycle 10 and cycle 20. This includes the battery cell potential and electrical current (top panel), the overpotentials of the negative and positive side (middle panel), and the redox potentials of the negolyte and posolyte (lower panel in Fig. 5). In the following, the overpotential data will not be analysed further as this has already been discussed in the polarisation curve. The primary purpose of Fig. 5 is to illustrate the complete set of parameters that is measured when the OCV cell and the M-cell are combined. Within this interval of early cycles, the curves are stable and reproducible from cycle to cycle, while their evolution over longer time scales is analysed in the following.
Battery cycling data are typically represented through the capacity and the faradaic efficiency, as shown in Fig. 6. The figure shows data from cycle 1 to cycle 180, recorded over a period of approximately 25 days, i.e., a full cycle takes approximately 3.3 hours. The initial capacity (116.2 mAh) is very close to the 120 mAh expected for a 1.5-electron transfer for AQDS.

The capacity is seen to increase slightly with cycle number until approximately cycle 135, after which it decreases rapidly to about 75 mAh at cycle 165. At this cycle, the posolyte was exchanged with a fresh solution of the same volume and composition as the original one, whereby the initial capacity (116.2 mAh) is almost fully restored after the exchange (115.2 mAh). Similarly, the faradaic efficiency is close to 100% in the initial cycles but decreases with cycle number; after the posolyte replacement, it is restored to close to 100%.

The understanding of the capacity-fade behaviour is dramatically improved by measuring the cell potential together with the redox potentials of the electrolytes using the OCV cell with internal reference. Fig. 7 shows the cell potential and the redox potentials of the

posolyte and negolyte for three selected cycles (#15, #160 and #170). Cycle 15 represents the initial behaviour, cycle 160 the behaviour just before the posolyte exchange, and cycle 170 the behaviour after the exchange. For simplicity, only the charging curves are shown. The following observations can be made:

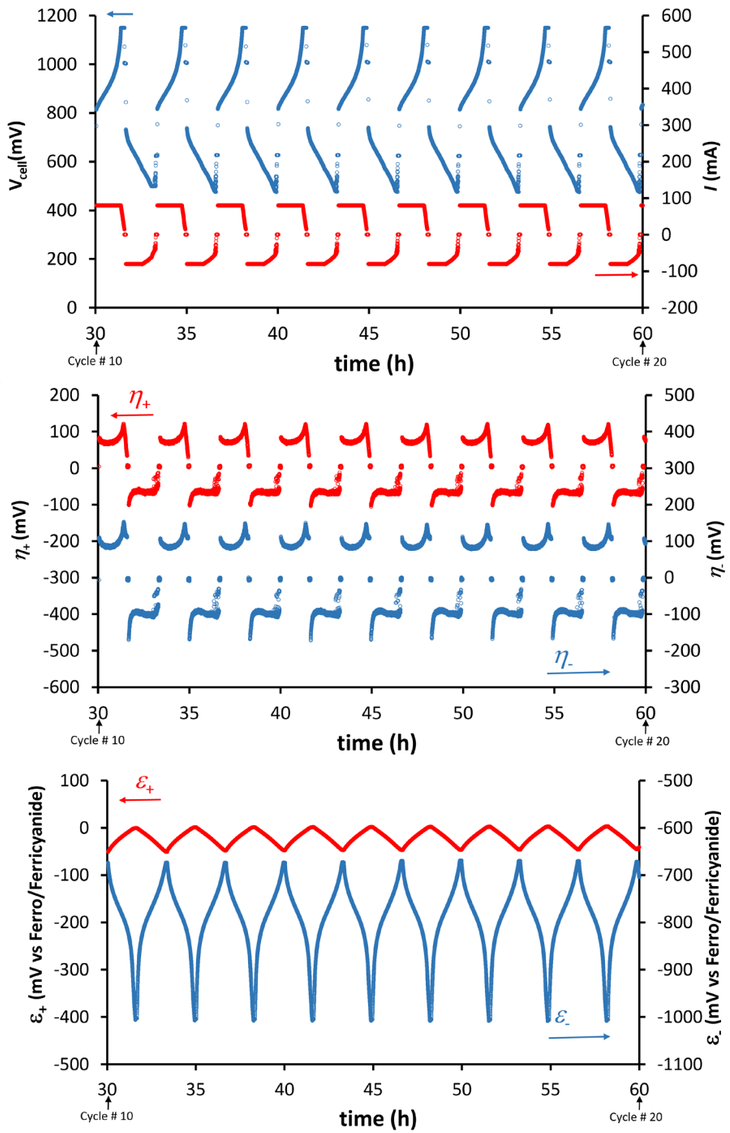



*Figure 5 – Time series data of all the measured data between cycle 10 and cycle 20. Cell potential and electrical current (top panel), the overpotential for both the negative and positive side (middle panel) and redox potentials of both the negolyte and posolyte (lower panel).*

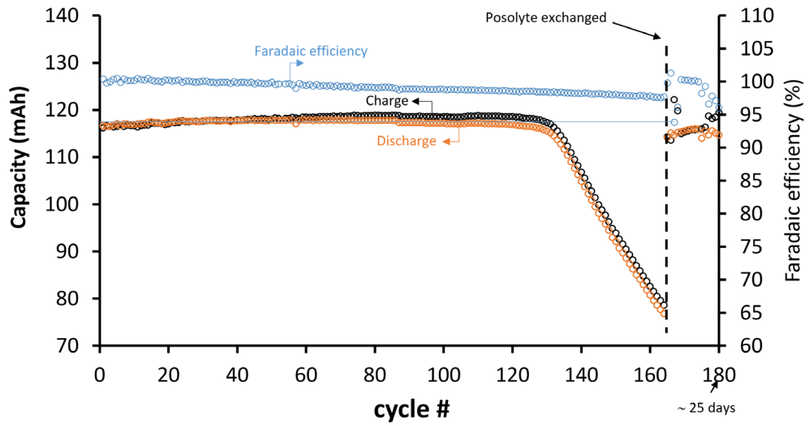



*Figure 6 – Charge/discharge capacity and faradaic efficiency vs cycle number. Before cycle 165 the posolyte is exchanged with a new solution of same composition and volume. Duration of full experiment was approximately 25 days*

- In the initial cycles (#15), the cell voltage increases monotonically until the voltage limit of 1150 mV is reached, and charging continues until full charge is reached (116.2 mAh). In cycle 160, the voltage is generally higher and full charge is reached already at 80.8 mAh. After the posolyte exchange, the charging curve is almost restored compared to the initial one, with only a slightly smaller capacity.
- (2) The origin of this behaviour can be elucidated from the posolyte and negolyte redox-potential measurements for the same cycles, shown in the lower panel of Fig. 7. For the initial cycles (#15), the posolyte potential ($\varepsilon_+$) only increases slightly, from about –50 mV to about 0 mV at full charge, whereas the negolyte potential ($\varepsilon_-$) decreases much more, from about –650 mV to about –1000 mV at full charge. This is as expected, since the posolyte (402 mAh) is in excess compared to the AQDS negolyte (120 mAh), whereby the full range of the Nernst potential is observed for the negolyte.
- (3) At cycle 160, the posolyte potential is higher than initially and increases to about 150 mV at full charge (80.8 mAh). Meanwhile, the negolyte potential almost follows the same curve as initially, except that it terminates at the reduced full charge (80.8 mAh).
- (4) In cycle 170, after the posolyte exchange, the posolyte and negolyte potential curves are almost fully restored to those of the initial cycle 15.
- (5) In particular, the increase of the posolyte redox potential indicates that an overall oxidation of the battery takes place. Hereby, the posolyte and negolyte get out of balance, and the posolyte becomes the capacity-limiting factor.

To investigate this further, the evolution of the posolyte and negolyte potentials as a function of cycle number is shown in Fig. 8. The evolution can be represented in several ways; ideally, it should be represented through the posolyte/negolyte SOC, but this would require accurate calibration tables between the SOC and $\varepsilon_+$ and $\varepsilon_-$, which is out of the scope of this white paper. Instead, the proxies ε_max (the maximum redox potential measured at either full charge or discharge), $\varepsilon_{min}$ (the minimum redox potential measured at either full charge or discharge) and the time-averaged ε_avr have been calculated. The top panel of Fig. 8 shows these parameters for the posolyte. Both $\varepsilon_{min}$ and $\varepsilon_{avr}$ increase monotonically with cycle number. $\varepsilon_{max}$ follows the same trend, but around cycle 130 it increases rapidly and reaches a value of about 150 mV. After the posolyte exchange, the potentials are restored to values slightly below the initial ones.

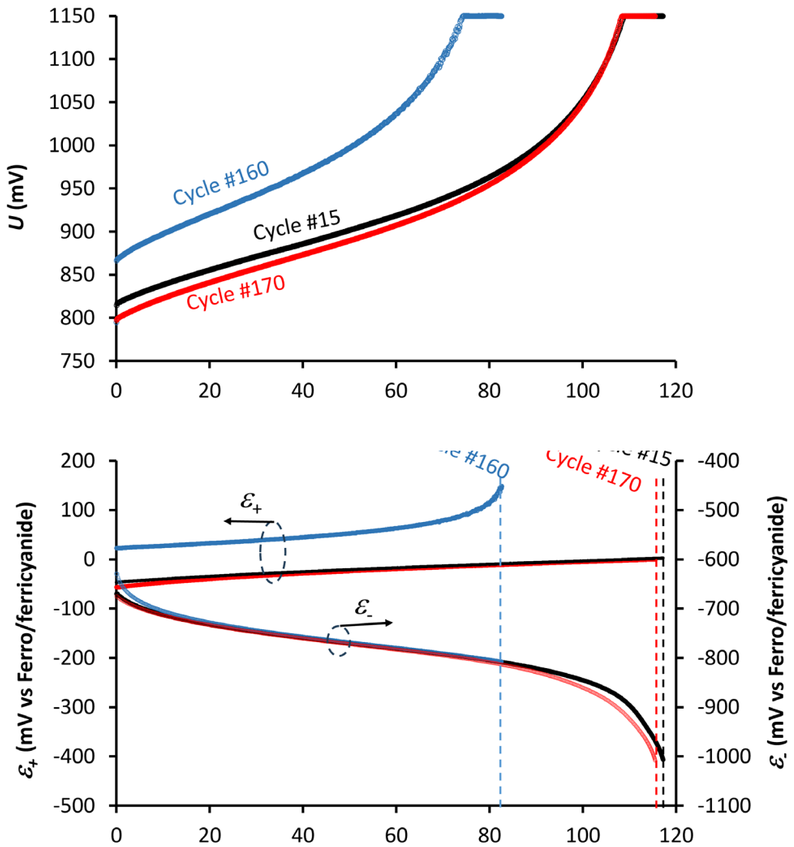



*Figure 7 – $U_{cell}$ (top panel), $\varepsilon_-$ and $\varepsilon_+$ (bottom panel) for cycle 15, 160 and 170 on charge. Note that relative scale for $\varepsilon_+$ and $\varepsilon_-$ are the same. Discharge data are not included in order to make the panels*

The lower panel of Fig.8 shows the same parameters for the negolyte. Here, a similar trend is observed: $\varepsilon_{max}$ increases slowly, while $\varepsilon_{avr}$ is almost constant up to cycle 130, after which it increases. $\varepsilon_{min}$ shows the largest change; initially, it is almost constant at –1000 mV, while just before the posolyte exchange it reaches almost –800 mV. After the posolyte exchange, the redox potentials are almost fully restored to their initial values.

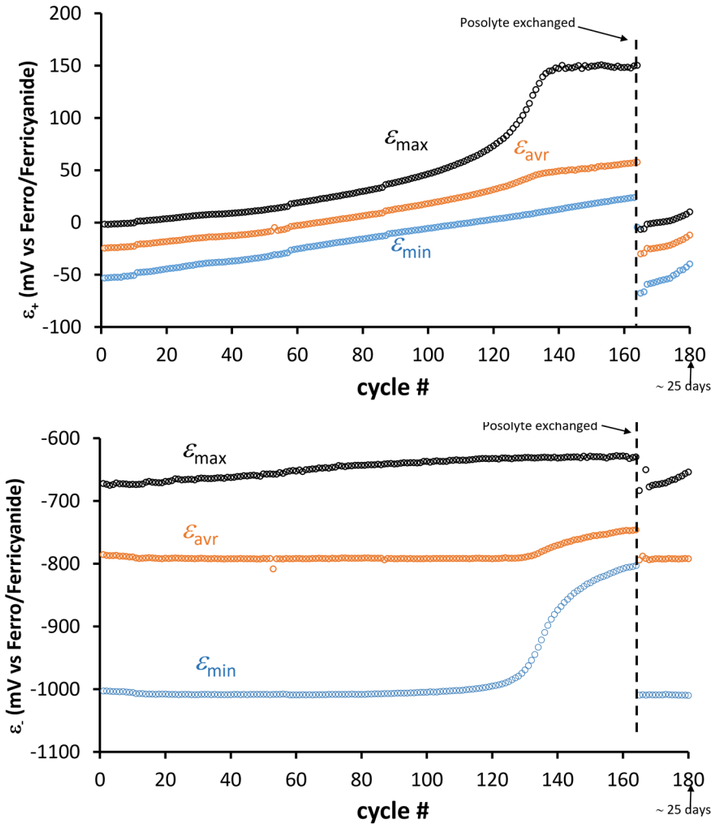



*Figure 8 –Maximum, minimum and time-averaged values of the redox potentials for $\varepsilon_+$ (top panel) and $\varepsilon_-$ (bottom panel) vs cycle number.*

From Figs. 6 and 7, it could only be speculated that an overall oxidation/imbalance of the battery explains the large capacity fade after approximately cycle 130; Fig. 8, however, clearly demonstrates that this is the case. $\varepsilon_{max}$ for the posolyte reaches a maximum value of about 150 mV at full charge, and since it is measured against the ferro-/ferricyanide reference, this means that the posolyte SOC is above 99 % at this point, whereby the

posolyte becomes the capacity-limiting side. Concurrently, $\varepsilon_{min}$ for the negolyte, i.e. the redox potential at full charge, increases rapidly after cycle 130. This shows that the AQDS can no longer be fully reduced, which corroborates the $\varepsilon_{max}$ data for the posolyte and demonstrates that the posolyte and negolyte have become imbalanced.

## Summary

The tests presented in this white paper demonstrate the power of the combined setup of the 1 $cm^2$ M-cell and the OCV cell with internal reference, which enables a full mapping of all relevant energy levels in a flow battery. As a demonstration, a long-term durability test with AQDS and ferrocyanide as the redox-active molecules was performed, showing the stability and functionality of the M-cell. The combined measurement of capacity, faradaic efficiency and electrolyte redox potentials made it possible to identify an oxidation-driven imbalance between the posolyte and negolyte as the origin of the observed capacity fade, information that is not accessible from standard cell-voltage measurements alone.





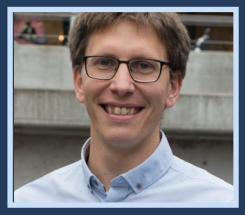
## Considerations and recommendations

Choosing the right experimental setup for low volume flow battery cycling, mapping out energy levels and potentials can be done in many ways and how to mitigate effects of $O_2$ in the air. The table below summarises some considerations for the choice of experimental setup.

| | |
|---|---|
| **When to use the M-cell for flow battery tests?** | 1. Small volumes and amounts of redox-active molecules – with the Hydraulic Connection Pack for Small Volumes (www.redox-flow.com/product/hydraulic-connection-pack-for-small-volumes/ ), volumes below 5 mL can be tested.<br>2. Small active electrode/membrane area – The M-cell has a fixed active area of 1 $cm^2$.<br>3. When combined with the OCV cell with internal reference (www.redox-flow.com/product/ocv-cell/ ) the M-cell becomes a uniquely powerful setup that enables the measurement of all relevant energy levels in flow battery tests.<br>4. Versatile cell that can be used for many electrochemical tests |
| **Influence of $O_2$ in air** | 1. Most anolytes (negolytes) for flow batteries can react with $O_2$ from the air, causing a slow oxidation/imbalance of the flow battery. This manifests itself as a capacity fade that is not related to the 'true' intrinsic capacity fade of the battery.<br>2. Air can enter the battery solutions through (i) bottle caps, (ii) tube feed-throughs into bottles and (iii) gaskets/sealings in the cell.<br>3. $O_2$ penetration into flow-battery systems operated in air most often originates from negative (relative) pressure on the suction side of the (peristaltic) pump. |
| **Mitigation of the effects of $O_2$ from the air** | 1. The most efficient mitigation is to place the whole flow battery test setup inside an oxygen-free chamber. However, this may be an expensive and elaborate solution that does not fit all purposes.<br>2. Bottles/reservoirs can continuously be purged with inert gas (e.g. $N_2$ or Ar). However, it is important that the gas is humidified before entering the bottle, otherwise water will evaporate rapidly from the redox solutions.<br>3. It is very important to consider the order of the units in the hydraulic circuit. **Redox-Flow always recommends placing the bottles/reservoirs just before the inlet/suction side of the pump; in this case, the effect of** the negative pressure is levelled out by the capacitive effect of the head space in the bottles, and less air will be sucked into the bottles (compared to, e.g., a cell placed just before the pump inlet). Additionally, the bottles/reservoirs can be placed inside ventilated, $O_2$-free surroundings. |

WWW.REDOX-FLOW.COM

# Any questions?
# We're happy to hear from you.




**MIKKEL KONGSFELT**

*CEO, HEAD OF SALES*

+45 31 26 20 40

SALES@REDOX-FLOW.COM

WWW.REDOX-FLOW.COM


Redox Flow®


Redox Flow
Stokagervej 6H
8240 Risskov
Denmark
CVR/VAT: DK40042350